Geosci. Model Dev., 18, 9061–9099, 2025
https://doi.org/10.5194/gmd-18-9061-2025

Geoscientific Model Development
Open Access
EGU

Development of UI-WRF-Chem (v1.0) for the MAIA satellite mission: case demonstration

Huanxin Zhang[1,2], Jun Wang[1,2], Nathan Janechek[1,2], Cui Ge[1,2,a], Meng Zhou[2,3,b,c], Lorena Castro García[1,2], Tong Sha[2], Yanyu Wang[2], Weizhi Deng[1,2], Zhixin Xue[1,2], Chengzhe Li[1,2], Lakhima Chutia[1,2], Yi Wang[2], Sebastian Val[4], James L. McDuffie[4], Sina Hasheminassab[4], Scott E. Gluck[4], David J. Diner[4], Peter R. Colarco[5], Arlindo M. da Silva[6], and Jhoon Kim[7]

[1]Department of Chemical and Biochemical Engineering, The University of Iowa, Iowa City, IA, 52242, United States
[2]Center for Global and Regional Environmental Research, The University of Iowa, Iowa City, IA, 52242, United States
[3]Interdisciplinary Graduate Program in Geo-Informatics, The University of Iowa, Iowa City, IA, 52242, United States
[4]NASA Jet Propulsion Laboratory, California Institute of Technology, Pasadena, CA, 91109, United States
[5]Atmospheric Chemistry and Dynamics Lab, NASA Goddard Space Flight Center, Greenbelt, MD, 20771, United States
[6]Global Modeling and Assimilation Office, NASA Goddard Space Flight Center, Greenbelt, MD, 20771, United States
[7]Department of Atmospheric Sciences, Yonsei University, Seoul, 03722, South Korea
[a]currently at: South Coast Air Quality Management District (AQMD), Diamond Bar, CA, 91765, United States
[b]currently at: Goddard Earth Sciences Technology and Research (GESTAR) II, University of Maryland, Baltimore County, Baltimore, MD, 21250, United States
[c]currently at: Global Modeling and Assimilation Office, NASA Goddard Space Flight Center, Greenbelt, MD, 20771, United States

Correspondence: Huanxin Zhang (huanxin-zhang@uiowa.edu) and Jun Wang (jun-wang-1@uiowa.edu)

Received: 24 March 2025 – Discussion started: 5 May 2025
Revised: 31 August 2025 – Accepted: 6 October 2025 – Published: 26 November 2025

Abstract. The Multi-Angle Imager for Aerosols (MAIA) satellite mission, to be jointly implemented by NASA and the Italian Space Agency, aims to study how different types of particulate matter (PM) pollution affect human health. The investigation will primarily focus on a discrete set of globally distributed Primary Target Areas (PTAs) containing major metropolitan cities, and will integrate satellite observations, ground observations, and chemical transport model (CTM) outputs (meteorology variables and PM concentrations) to generate maps of near-surface total and speciated PM within the PTAs. In addition, the MAIA investigation will provide satellite measurements of aerosols over a set of Secondary Target Areas (STAs), which are useful for studying air quality more broadly. For the CTM, we have developed a Unified Inputs (of initial and boundary conditions) for WRF-Chem (UI-WRF-Chem) modeling framework to support the MAIA satellite mission, building upon the standard WRF-Chem model. The framework includes newly developed modules and major enhancements that aim to improve model simulated meteorology variables, total and speciated PM concentrations as well as AOD. These developments include: (1) application of NASA GEOS FP and MERRA-2 data to provide both meteorological and chemical initial and boundary conditions for performing WRF-Chem simulations at a fine spatial resolution for both forecast and reanalysis modes; (2) application of GLDAS and NLDAS data to constrain surface soil properties such as soil moisture; (3) application of recent available MODIS land data to improve land surface properties such as land cover type; (4) development of a new soil NO_x emission scheme – the Berkeley Dalhousie Iowa Soil NO Parameterization (BDISNP); (5) development of a stand-alone emission preprocessor that ingests both global and regional anthropogenic emission inventories as well as fire emissions.

Here, we illustrate the model improvements enabled by these developments over four target areas: Beijing in China, CHN-Beijing (STA); Rome in Italy, ITA-Rome (PTA); Los Angeles in the U.S., USA-LosAngeles (PTA), and Atlanta

in the U.S., USA-Atlanta (PTA). UI-WRF-Chem is configured as 2 nested domains using an outer domain (D1) and inner domain (D2) with 12 and 4 km spatial resolution, respectively. For each target area, we first run a suite of simulations to test the model sensitivity to different physics schemes and then select the optimal combination based on evaluation of model simulated meteorology with ground observations. For the inner domain (D2), we have chosen to turn off the traditional Grell 3D ensemble (G3D) cumulus scheme. We conducted a case study over USA-Atlanta for June 2022 to demonstrate the impacts of the cumulus scheme on precipitation and subsequent total and speciated $PM_{2.5}$ concentrations. Our results show that keeping the G3D cumulus scheme turned on results in higher precipitation and lower total and speciated $PM_{2.5}$ than the simulation with the G3D cumulus scheme turned off. Compared with surface observations of precipitation and $PM_{2.5}$ concentration, the simulation with the G3D scheme off shows better performance. We focus on two dust intrusion events over CHN-Beijing and ITA-Rome, which occurred in March 2018 and June 2023, respectively. We carried out a suite of sensitivity simulations using UI-WRF-Chem by excluding chemical boundary conditions or including MERRA-2 chemical boundary conditions. Our results show that using MERRA-2 data to provide chemical boundary conditions can help improve model simulation of surface PM concentrations and AOD. Some of the target areas have also experienced significant changes in land cover and land use over the past decade. Our case study over CHN-Beijing in July 2018 investigates the impacts of improved land surface properties with recent available MODIS land data on capturing the urban heat island phenomenon. Model-simulated surface skin temperature shows better agreement with MODIS observed land surface temperature. The updated soil NO_x emission scheme in July 2018 also leads to higher NO_2 vertical column density (VCD) in rural areas within the CHN-Beijing target area, which matches better with TROPOMI observed NO_2 VCD. This in turn affects the simulation of surface nitrate concentration. Lastly, we conducted a case study over USA-LosAngeles to tune dust emissions. These examples illustrate the fine-tuning work conducted over each target area for the purpose of evaluating and improving model performance.

1 Introduction

Ambient particulate matter (PM) pollution has been ranked as the top environmental risk factor for premature deaths (Forouzanfar et al., 2016). The integrated use of satellite and chemical transport model (CTM) outputs have shed light on the impacts of $PM_{2.5}$ (PM with aerodynamic diameter less than 2.5 µm) on public health in the past decade (Cohen et al., 2017; Wang et al., 2021a). Satellite-retrieved aerosol data products such as aerosol optical depth (AOD) have been widely used to estimate ground-level $PM_{2.5}$ concentration over the past two decades (e.g., Shin et al., 2020; Van Donkelaar et al., 2006; Wang and Christopher, 2003) due to the wide spatial coverage achievable from spaceborne observations. Because of uncertainties in remote sensing retrievals and the complex AOD-$PM_{2.5}$ relationship (Wang and Christopher, 2003), satellite-derived ground-level $PM_{2.5}$ have been combined with ground observations of $PM_{2.5}$ and/or CTM simulated $PM_{2.5}$ to form a hybrid method of providing a new data source for epidemiological health studies (e.g., Van Donkelaar et al., 2010; Holloway et al., 2021; Diao et al., 2019). This hybrid method has also been used for estimating $PM_{2.5}$ component concentration and its application in health-related studies (Philip et al., 2014; Li et al., 2021; Hu et al., 2019; Wei et al., 2023). The association between exposure to PM and mortality has been well established. However, since ambient PM is a complex mixture of particles that vary in size, shape and chemical composition, there remains uncertainty in understanding the relative toxicity of different PM types to human health (Sangkham et al., 2024; Weichenthal et al., 2024).

The Multi-Angle Imager for Aerosols (MAIA) satellite mission to be jointly implemented by the National Aeronautics and Space Administration (NASA) (Diner et al., 2018) and the Italian Space Agency (ASI) has a key objective to map PM composition and study the impacts of different types of PM on human health (Liu and Diner, 2017). The MAIA instrument builds upon the work of the Multi-angle Imaging SpectroRadiometer (MISR) instrument onboard NASA's Terra spacecraft, which has been retrieving aerosol properties including aerosol type since February 2000 (Diner et al., 1998; Kahn et al., 2005). MISR has also been one of the commonly used satellite instruments for mapping global PM concentration for studying air quality and public health (Liu et al., 2009; Holloway et al., 2021; Meng et al., 2018). The MAIA instrument contains a pointable 14-wavelength pushroom camera, spanning the ultraviolet (UV), visible and near-infrared (VNIR) and shortwave infrared (SWIR) regions of the electromagnetic spectrum to measure the spectral radiance of sunlight scattered by the Earth's atmosphere and surface. Three of the bands are polarimetric to further help constrain aerosol particle properties. The MAIA investigation will focus on a globally distributed set of primary target areas (PTAs) (https://maia.jpl.nasa.gov/mission/#target_areas, last access: 7 November 2025) for PM health studies, which include metropolitan cities. For each PTA, it will employ Geostatistical Regression Models (GRMs), to generate maps of surface total $PM_{2.5}$, PM_{10} and speciated PM including sulfate, nitrate, dust, organic carbon (OC) and elemental carbon (EC). The GRMs use satellite retrieved aerosol parameters, CTM outputs (meteorological variables along with total and speciated PM mass concentrations) and other ancillary information such as population density data as predictors. Surface observations of total and speciated PM are

used to train the GRMs (i.e., determine the coefficients of the model predictors) (Jin et al., 2024).

Our work here introduces the development of the Unified Inputs (of initial and boundary conditions) for WRF-Chem (UI-WRF-Chem) as the CTM for supporting the MAIA satellite mission, based on the standard WRF-Chem model (Fast et al., 2006; Grell et al., 2005). Since meteorological variables as well as total and speciated PM mass concentrations from UI-WRF-Chem outputs are used in the GRMs to derive the total and speciated PM maps, we have implemented major updates in UI-WRF-Chem that aim to improve model simulated meteorology variables or PM concentration through the integrated use of satellite and ground-based observations. Because WRF-Chem is an online coupled chemical transport model, the improvement of aerosol concentration simulation could also enhance the simulation of meteorology through the incorporation of aerosol radiation feedback, especially in polluted regions such as Delhi, India (Chutia et al., 2024).

The UI-WRF-Chem modeling framework builds upon the standard WRF-Chem model with newly developed modules and major enhancements that enable integration of NASA Goddard Earth Observing System (GEOS) data for unified meteorology and chemistry inputs, updates of land surface properties with recent available Moderate Resolution Imaging Spectroradiometer (MODIS) land data, and expanded emission processing capabilities:

- First, we use the NASA GEOS products including both GEOS Forward Processing (FP) and Modern-Era Retrospective analysis for Research and Application, version 2 (MERRA-2) data to provide both meteorological and chemical initial and boundary conditions for performing WRF-Chem simulation with a finer spatial resolution in forecasting and reanalysis modes, which allows for consistency between meteorology and chemistry. The NASA GEOS system assimilates satellite observations of aerosol products (Randles et al., 2017). Using these assimilated data to provide chemical initial and boundary conditions for WRF-Chem simulations over MAIA target areas would be computationally efficient for capturing long-range or regional transport without enlarging the model domain to include the emission sources. A number of studies have demonstrated the influence of chemical boundary conditions on regional air pollution in the domain of interests, when running WRF-Chem (e.g., Mo et al., 2021; Ukhov et al., 2020; Roozitalab et al., 2021; Wang et al., 2004).

- Second, we employ data from the Global Land Data Assimilation System (GLDAS) (Rodell et al., 2004) or the North American Land Data Assimilation System (NLDAS) (Mitchell et al., 2004) to constrain soil properties such as soil moisture in WRF-Chem. Soil properties are critical for weather forecasts, biogenic emission estimates and dust storm simulation (Han et al., 2021), and ultimately, air quality prediction (Thomas et al., 2019; Jenkins and Diokhane, 2017; de Rosnay et al., 2014). Both GLDAS and NLDAS provide optimized initial soil conditions with a high spatial and temporal resolution for numerical weather forecasting (Dillon et al., 2016; Xia et al., 2014). Better estimates of soil properties also enhance the simulation of soil NO_x emissions, serving as an important part of the total global NO_x budget (Jaeglé et al., 2005), and subsequently improve the simulation of nitrate aerosols.

- Third, we use recent available MODIS land data to update static land surface properties such as land cover type in WRF-Chem. Some of the default land surface properties used in WRF-Chem are out of date. Using recent available MODIS land data to update land surface properties would help improve mesoscale model performances (Li et al., 2014, 2017a; Aegerter et al., 2017; Wang et al., 2023).

- Fourth, we develop the Berkeley Dalhousie Iowa Soil NO Parameterization (BDISNP) scheme for simulating soil NO_x ($NO + NO_2$) emissions, building upon the Berkeley Dalhousie Soil NO Parameterization (BDSNP) scheme (Hudman et al., 2012). Previous study showed that the default soil NO_x emissions in WRF-Chem could be underestimated by a factor of 10 in some regions (Oikawa et al., 2015). Since soil NO_x emissions play a critical role in the formation of ozone (O_3) and nitrate aerosols (Sha et al., 2021; Lin et al., 2021), their accurate representation in the model is essential.

- Finally, we develop a stand-alone WRF-Chem Emission Preprocessing System (WEPS) that ingests both global and regional anthropogenic emission inventories as well as fire emissions. Because anthropogenic and fire emissions are important for aerosol simulations in the model, building our own emission preprocessor allows us the opportunities to optimize existing emission inventories and add new ones, including those from top-down estimates (Wang et al., 2020b, c).

In this paper, we present the developments of the UI-WRF-Chem modeling framework and illustrate the resulting model improvements. We focus on four target areas, three of which are MAIA PTAs: Rome, Italy (ITA-Rome), Los Angeles, California (USA-LosAngeles) and Atlanta, Georgia (USA-Atlanta). We also include Beijing, China (CHN-Beijing), which is MAIA secondary target areas (STAs). STAs are regions that will be observed by the MAIA satellite instrument but not necessarily processed to the same level as PTAs. These four target areas together provide a good representation of the range of PM pollution levels from low (Los Angeles and Atlanta), to high (Beijing) with Rome in the middle. Some of our previous studies have focused on other MAIA PTAs using the UI-WRF-Chem modeling framework. Li et

al. (2024) developed an inverse modeling method to improve the diurnal profile of anthropogenic emissions in the Addis Ababa, Ethiopia PTA, using surface-based PM observations from both U.S. Embassy sites and PurpleAir sensors. Chutia et al. (2024) investigated the impacts of aerosol-radiation interaction on air quality in the Delhi, India PTA. Overall, current work along with previous work can provide a good picture of the model performance for different applications. This paper is organized as follows: Sect. 2 focuses on the description of the UI-WRF-Chem model development; Sect. 3 provides the model configuration used in the target areas; Sect. 4 analyzes the case studies for different target areas; and Sect. 5 presents conclusions and discussion.

2 UI-WRF-Chem development

In this section, we first provide a brief overview of the MAIA PM products to illustrate the role of UI-WRF-Chem. We then describe the development of the UI-WRF-Chem modeling framework, emphasizing the major updates and key components designed to address the needs of the MAIA satellite mission.

2.1 Overview of MAIA PM products

The MAIA PM products to be generated in the PTAs include a Level 2 (L2) PM product and a Level 4 (L4) Gap-Filled PM (GFPM) product. Both L2 and L4 PM products include 24 h averaged total and speciated PM mass concentration with a spatial resolution of 1 km within bounding boxes measuring 360 km × 480 km (east-west × north-south) size. The L2 PM data are only available for days corresponding to MAIA satellite overpasses (typically 3–4 times per week in the PTAs) at locations with valid MAIA aerosol retrievals. The L4 PM data merge L2 satellite-derived PM concentration with bias-corrected PM concentrations from UI-WRF-Chem outputs and are therefore spatially (covering the whole target area) and temporally (daily) "complete". The L2 PM product is derived using GRMs which take the satellite retrieved aerosol parameters, meteorological variables and total and speciated PM concentrations from UI-WRF-Chem and other ancillary information such as population density data as predictors and surface observations of total and speciated PM concentrations as target variables. GRMs are trained for each PM type and each PTA. For the launch-ready version of the GRMs, four meteorological variables from UI-WRF-Chem are used: 2 m air temperature, 10 m wind speed, surface relative humidity (RH) and planetary boundary layer height (PBLH). To generate the L4 GFPM product, separately trained GRMs are employed to generate a bias-corrected, CTM-based PM product where the primary predictor is the CTM-generated PM concentration, rather than the satellite-retrieved aerosol optical depth. Other predictors and target variables are the same as those used in the generation of L2 PM product. For areas where both satellite-derived L2 PM and CTM-based PM products are available, these two products are then combined using weights derived from a Bayesian Ensemble Averaging model to generate the final L4 GFPM product. More detailed information can be found in Jin et al. (2024).

Two versions of the MAIA L2 PM and L4 GFPM products will be generated as part of the routine processing: the "forecast" and the "reanalysis" version. For the forecast product version, GEOS FP meteorology is used for model initial and boundary conditions and GEOS FP fields of aerosols and aerosol precursors will also be used to specify boundary conditions of atmospheric composition. The reanalysis versions replace GEOS FP variables with outputs from MERRA-2 data. Due to the ∼6 month latency of speciated $PM_{2.5}$ data from surface monitors, the forecast versions will rely on previously available measurements. Generation of the reanalysis products will nominally occur on an annual basis and will benefit from more complete surface monitor datasets. More detailed information about the PM products can be found at https://maia.jpl.nasa.gov/resources/data-and-applications/ (last access: 7 November 2025).

2.2 Overview of UI-WRF-Chem modeling framework

To meet these needs, UI-WRF-Chem is designed to operate in both forecasting (or near real time, NRT) and reanalysis modes. We use the NASA GEOS model data: GEOS FP in forecasting or NRT mode and MERRA-2 in reanalysis mode to drive WRF-Chem simulations by providing self-consistent and unified meteorological and chemical initial and boundary conditions, referred to as the Unified Inputs (of initial and boundary conditions) for meteorology and chemistry. Figure 1 presents the flowchart of the UI-WRF-Chem modeling framework. Here, we provide a brief description of the UI-WRF-Chem framework, outline the components included in the standard WRF-Chem model and highlight the major updates we have introduced.

Compared with the standard WRF-Chem model, the UI-WRF-Chem modeling framework incorporates new modules and significant modifications to enable the seamless use of NASA GEOS data, updates of land surface properties with recent available MODIS land data and expanded emission capabilities. First, we incorporate the GEOS2WRF module from NASA's Unified-Weather Research and Forecasting model (NU-WRF) (Peters-Lidard et al., 2015), which functions similarly to the standard ungrib process, by converting GEOS FP or MERRA-2 data to an intermediate file format. We also develop the LDAS2WRF module, adapted from the GEOS2WRF module to convert the GLDAS or NLDAS data into the same intermediate file format. The standard metgrid process then converts these intermediate files into meteorological files in the NetCDF format (met_em.d*.nc), respectively. These two NetCDF files are subsequently merged to generate the final meteorological files for the real process.

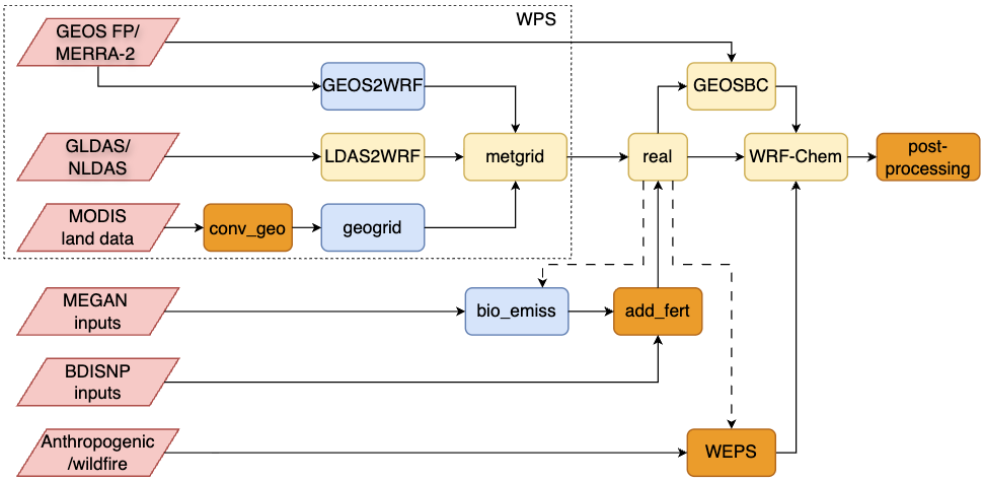

Figure 1. Flowchart of UI-WRF-Chem modeling framework. Pink parallelogram represent input datasets used, including meteorological, land surface and emission data. Rounded rectangles represent different modules and processes within the UI-WRF-Chem framework. Blue rounded rectangles denote standard WRF-Chem components without any changes, except for GEOS2WRF, which is from NASA's NU-WRF framework. Yellow round rectangles represent modified modules based on standard WRF-Chem components, except for LDAS2WRF, which is adapted from GEOS2WRF. Orange rounded rectangles indicate new modules developed in this work. The input datasets and modules enclosed within the dashed box corresponds to the WPS in the standard WRF-Chem model, where meteorological files (met_em.d*.nc) are generated. The conv_geo process converts MODIS land data into binary files, for the geogrid process. Both GEOS2WRF and LDAS2WRF convert input data in the NetCDF file format to an intermediate file format, equivalent to the ungrib process. GEOSBC is adapted from the mozbc module, where GEOS FP and MERRA-2 data are used to update chemical initial and boundary conditions. The bio_emiss module reads MEGAN emission input datasets (e.g., isoprene emission factor) and generates files (wrfbiochemi_d0*) for WRF-Chem to calculate biogenic emissions. The add_fert module is used to add the BDISNP input datasets (e.g., fertilizer data) into the wrfbiochemi_d0* files for the real process. WEPS processes both anthropogenic and fire emission datasets and converts them into WRF-Chem ready emission files (*wrfchemi*). Dashed lines from real to bio_emiss and WEPS indicate that real needs to be executed once before running the full flow to generate wrfinput_d0* files, which provide domain information to these two modules.

Second, to integrate the MODIS land data into the static geographical datasets, we develop the conv_geo Python-based module, where we convert the MODIS land data into the standard binary file formats required by the geogrid process. This enables updates of land surface properties with recent available MODIS land data, not available in the standard WRF-Chem model. We also develop the GEOSBC module, by modifying the standard mozbc module to use GEOS FP or MERRA-2 data for updating both chemical initial and boundary conditions, which improves the consistency between meteorology and chemistry inputs. Additionally, we modify WRF-Chem's chemistry scheme to ensure compatibility between dust fields from GEOS FP or MERRA-2 and the dust representation in the chemistry scheme itself (see Sect. 2.7 for more information).

For emissions, we develop the BDISNP scheme for soil NO_x emissions by extending the workflow of the standard MEGAN-based biogenic VOC calculation. Same as the MEGAN process, we first use the standard bio_emiss module to read the MEGAN emission input datasets (e.g., isoprene emission factor) and then convert them into the wrfbiochemi_d0* files for the real process. We then apply the add_fert module that we have developed here to incorporate emission input datasets (e.g., fertilizer data), specific to the BDISNP scheme into wrfbiochemi_d0* files. Additionally, we modify WRF-Chem codes to calculate soil NO_x emissions. We also develop the WEPS module to process both anthropogenic and fire emissions, adopting some functionalities from the widely used anthro_emiss and EPA_ANTHRO_EMISS utilities in the WRF-Chem community. This provides flexibility for incorporating additional emission inventories into the WEPS. Lastly, we develop a Python-based postprocessing module to calculate selected WRF-Chem variables and compile hourly WRF-Chem output files into daily files in the formats required by the GRMs.

2.3 Updates of meteorological and chemical initial and boundary conditions as well as soil properties

Here, we have adopted the functionality of the NASA's NU-WRF to drive WRF-Chem by providing unified meteorological and chemical initial and boundary conditions using GEOS FP and MERRA-2 data. Both GEOS FP and MERRA-2 data are generated within the GEOS atmospheric and data assimilation system (Rienecker et al., 2008), in which meteorological and aerosol observations are jointly assimilated. GEOS FP uses the most recent GEOS system to produce the real-time forecasting data while MERRA-2 uses a frozen

version of the GEOS system to conduct the long-term atmospheric reanalysis since 1980. The GEOS native model is on a cubed sphere grid with 72 hybrid-eta layers from surface to 0.01 hPa. Products are saved on a $0.5° \times 0.625°$ latitude by longitude grid for MERRA-2 and $0.25° \times 0.3125°$ latitude by longitude for GEOS FP (Gelaro et al., 2017).

MERRA-2 assimilates multiple streams of aerosol products including bias corrected AOD calculated from observed radiances measured by the Advanced Very High Resolution Radiometer (AVHRR) over ocean prior to 2002 and by MODIS on Terra and Aqua satellites over dark surfaces and ocean since 2000 and 2002, respectively; also assimilated are the MISR AOD over bright land surface and AOD measurements from Aerosol Robotic Network (AERONET) before 2014 (Randles et al., 2017). In the NRT mode, GEOS FP only assimilates AOD derived from MODIS Terra and Aqua. The aerosol module used in the GEOS system is the Goddard Chemistry, Aerosol, Radiation, and Transport (GOCART) model (Colarco et al., 2010; Chin et al., 2002). The GOCART module simulates major aerosol species including sulfate, BC, OC, dust (five bins with lower and upper radius range as: 0.1–1, 1–1.8, 1.8–3, 3–6, 6–10 µm), and sea salt (five bins with lower and upper radius range as: 0.03–0.1, 0.1–0.5, 0.5–1.5, 1.5–5.0, 5.0–10 µm). These aerosol products are available in both GEOS FP and MERRA-2 products. Since 2017, nitrate aerosols have been added into the GEOS system and GEOS FP products thus include nitrate aerosols.

Our work differs from the past work that uses the GEOS FP or MERRA-2 data to drive WRF-Chem in several aspects. For example, Peters-Lidard et al. (2015) presented the NU-WRF model that can be driven by GEOS FP and MERRA-2, but its atmospheric chemistry process is simplified with the GOCART module (without prognostic simulation of aerosol size distribution and nitrate for example) and is designed to be an observation driven integrated modeling system that represents aerosol, cloud, precipitation, and land processes at satellite-resolved scales ($\sim$ 1–25 km). Hence, its real-time application for atmospheric chemistry and aerosol composition forecast is rather limited. Nevertheless, the NU-WRF's concept and framework (GEOS2WRF, Fig. 1) of using GEOS FP and MERRA-2 to drive WRF-Chem are adopted by UI-WRF-Chem development here to provide meteorological initial and boundary conditions for WRF-Chem, using meteorological variables other than soil properties.

Adopting of GEOS FP or MERRA-2 soil properties into WRF-Chem needs special treatment. In the GEOS system, the land surface model (LSM) is a catchment-based model (Koster et al., 2000), which is fundamentally different from the LSMs available in WRF-Chem. The commonly used LSMs in WRF-Chem include the Noah scheme (Chen et al., 1996; Chen and Dudhia, 2001), the Rapid Update Cycle (RUC) (Smirnova et al., 2000), and the Community Land Model (CLM) (Oleson et al., 2004), which are all column-based models with different soil layers. To resolve this issue, Peters-Lidard et al. (2015) used the Land Information System (LIS) (Kumar et al., 2006) to process GEOS outputs and provide initial conditions of soil properties such as soil temperature and soil moisture for running WRF and NU-WRF (Kumar et al., 2008). Since land surface process is slow and usually requires years of LIS simulation to stabilize the soil properties in the model, we have here developed a module (LDAS2WRF, Fig. 1) to utilize soil data products from two land data assimilation systems, GLDAS (Rodell et al., 2004) and NLDAS (Mitchell et al., 2004), which use LIS to focus on the analysis of soil properties in near real time. This way, we reduce the computational cost and complexity of running LIS within the UI-WRF-Chem. The initial conditions of soil properties can have an important impact on boundary layer processes for days to weeks (the so-called memory effect). Hence, the special treatment of soil properties by using observation-constrained GLDAS and NLDAS in UI-WRF-Chem is warranted.

We have developed the capability to use GEOS FP and MERRA-2 data to provide chemical initial and boundary conditions in our UI-WRF-Chem modeling framework. Since WRF-Chem is a regional chemical transport model, time-varying chemical boundary conditions from global chemical transport models are typically used to specify concentrations of different chemical species at the domain boundaries. This is especially important for long-lived chemical species, such as O_3, or capturing regional or long-range transport events. The common practice is to use global model outputs such as the Community Atmosphere Model with Chemistry, CAM-Chem (Emmons et al., 2020) for reanalysis or the Whole Atmosphere Community Climate Model (WACCM) (Gettelman et al., 2019) for forecasts. Unlike CAM-Chem or WACCM, which do not assimilate satellite aerosol observations, GEOS FP and MERRA-2 incorporate satellite-based aerosol data assimilation, which provides observational constraints for the day-to-day variations in aerosol concentrations over a given domain. To leverage this unique capability, we have modified the WRF-Chem preprocessor tool – mozbc (https://www2.acom.ucar.edu/wrf-chem/wrf-chem-tools-community, last access: 10 May 2022) to create the GEOSBC module (Fig. 1), enabling direct ingestion of GEOS FP and MERRA-2 data for updating chemical initial and boundary conditions.

Lastly, we have developed a method to constrain the chemical boundary condition for the allocation of dust concentration in the MERRA-2 data as a function of different dust size bins. While assimilating satellite-derived aerosol optical parameters can improve the simulation of dust in MERRA-2 data, uncertainties remain in simulating the dust size distribution from emission sources and along the transport pathway in the MERRA-2 data (Kramer et al., 2020). These uncertainties are particularly evident during long-range dust transport events, due to factors such as the deposition process and the quality of satellite data being assimilated (Zhu et al., 2025). To address this, we have developed a method to further con-

strain the MERRA-2 simulated dust size distribution with AERONET observation, which can be incorporated into the chemical boundary conditions for simulating the impacts of dust transport on the domain of interest. This method is applicable in regions where AERONET sites with long-term data are available. We compare the dust particle size distribution (PSD) from MERRA-2 data with AERONET observations to improve the allocation of dust concentration into different size bins in the chemical boundary conditions. A detailed description and application of this approach are provided in Sect. 4.1 and 4.2.

2.4 Updates of land surface properties

We develop capabilities within UI-WRF-Chem to update land surface properties using recent available satellite-based land data products through the WRF Preprocessing System (WPS). MODIS land products are applied here to update four key land surface properties in the Noah LSM: land cover type on an annual basis and green vegetation fraction (GVF), leaf area index (LAI), and surface albedo on a monthly basis. These variables are among the key surface properties in the land model that regulate the exchanges of energy, water, and momentum (Mölders, 2001). The major technical development and its application to study the impacts of land use/-cover changes on urban temperature in Eastern China during 2003–2019 were described in Wang et al. (2023). Below we briefly describe the updates of each land surface property.

The standard WRF-Chem model provides different sources of data for land surface properties. For land cover type, one data source is from the U.S. Geological Survey (USGS) map with 24 land cover types, which is derived from the monthly AVHRR Normalized Difference Vegetation Index (NDVI) observations from April 1992 to March 1993. Another one is from the MODIS land cover data including 17 land cover types, based on the International Geosphere-Biosphere Program (IGBP) scheme (Friedl et al., 2002) and three classes of tundra (Justice et al., 2002). Historically, MODIS land cover data inputs used in WRF-Chem have been fixed to years such as 2001 or 2004, or to 2001–2010 climatology data (Broxton et al., 2014). For GVF, the default data is derived from the AVHRR NDVI observations (1985–1990). An alternative option is to use the MODIS Fraction of Photosynthetically Active Radiation (FPAR) (early 2000s) to substitute for GVF. For LAI and surface albedo, one option is to calculate the values online using a look-up table, based on each land cover type. Another option is to use the MODIS LAI and albedo data directly (early 2000s).

Since these data sources are outdated, we have developed the conv_geo Python-based module (Fig. 1) to update all four land surface properties in UI-WRF-Chem via the WPS using recent available MODIS land data. This approach provides self-consistence among the key land surface properties used in the land model as they come from the same satellite observations and offers a flexible way to apply the data for WRF-Chem simulations across different spatial resolutions. Specifically, the land cover type is updated with the MODIS yearly land cover type product (MCD12Q1). GVF can be updated by: (1) deriving from the MODIS monthly NDVI product (MOD13A3) or (2) substituting with MODIS 8-day FPAR product (MCD15A2H). LAI is updated directly from MODIS 8-day LAI product (MCD15A2H). Surface albedo can be updated using either the MCD43A3 daily albedo product or the MODIS combined Terra and Aqua Bidirectional Reflectance Distribution Function (BRDF) and Albedo daily product (MCD43C3). For the MAIA project, MODIS land data from 2018–2020 are used as static inputs to the UI-WRF-Chem simulations, except for CHN-Beijing where only 2018 data are applied.

2.5 Development of the BDISNP soil NO_x emission scheme

The new BDISNP soil NO_x emission scheme is also integrated as part of the UI-WRF-Chem framework. The detailed development of the scheme has been described in Sha et al. (2021) and Wang et al. (2021c). Briefly, in the standard WRF-Chem model, soil NO_x emissions are calculated using the Model of Emissions of Gases and Aerosols from Nature (MEGAN) (Guenther et al., 2006; Guenther et al., 2012), which is intended for estimating biogenic emissions of volatile organic compounds (VOCs). In the MEGAN model, emission factors are based on four global plant function types (broadleaf trees, needleleaf trees, shrubs/bushes and herbs/crops/grasses). Previous work by Oikawa et al. (2015) has suggested that soil NO_x emissions calculated from the MEGAN model using WRF-Chem can be a factor of 10 underestimated in the Imperial Valley, California, compared with ground observations. The BDSNP soil NO_x emission scheme, currently implemented in the global 3-D GEOS-Chem model (Hudman et al., 2012), was added into the UI-WRF-Chem, as the BDISNP, with several of our own updates.

As in BDSNP, the BDISNP includes a more physical representation of the soil NO_x emission process compared with the MEGAN model. The BDISNP considers available nitrogen (N) in soils from biome specific emission factors, online dry and wet deposition of N, and fertilizer and manure N. It also includes the pulsing of soil NO_x emission following soil wetting by rain and the impacts of soil temperature and moisture. Compared to BDSNP, we have made four major updates in the BDISNP: (1) updating the land cover type data with the recent available MODIS land cover type data to better reflect the land cover change; (2) using the GLDAS soil temperature data for calculating soil NO_x emissions rather than using the 2 m air temperature as a proxy for soil temperature; (3) using the modeled GVF data to determine the distribution of arid and non-arid regions to replace the static climate data used in the BDSNP scheme. With these three updates, Sha et al. (2021) has shown that the WRF-Chem simulation with the

BDISNP scheme leads to a better agreement with TROPOspheric Monitoring Instrument (TROPOMI) retrieved NO_2 columns over California for July 2018, compared with using the default MEGAN scheme. The increased soil NO_x emissions with the BDISNP scheme result in a 34.7 % increase in monthly mean NO_2 columns and 176.5 % increase in surface NO_2 concentration, which causes an additional 23.0 % increase in surface O_3 concentration in California. The work of Zhu et al. (2023) used derived soil NO_x flux measurements from a field campaign over the San Joaquin Valley in California during June 2021 to evaluate three soil NO_x emission schemes: the MEGAN in the California Air Resource Board (CARB) emission inventory, the Biogenic Emission Inventory System (BEIS) and the BDISNP developed here. It was found that both MEGAN and BEIS inventories were lower than the observation by more than one order of magnitude, and the BDISNP was lower by a factor of 2.2. Even though being underestimated, the BDISNP and the observation showed a similar spatial pattern and temperature dependence.

The fourth update revises the default soil temperature response function in the BDSNP scheme, as described in Wang et al. (2021c). In the default scheme, the soil temperature response follows an exponential function for soil temperature between 0 and 30 °C and stays the same as 30 °C after the soil temperature is above 30 °C. In the work of Oikawa et al. (2015), which found high soil NO_x emissions in high-temperature agricultural soils, an observation-based soil temperature response function was developed. This function is used here to update the default soil temperature response function. Specifically, for soil temperature in the range of 20 and 40 °C, it is a cubic function of soil temperature. When soil temperature is greater than 40 °C, the value of the response function is set the same as the value of soil temperature at 40 °C. In addition, final soil NO_x emissions are reduced by 50 % following the work of Silvern et al. (2019) and Vinken et al. (2014). With this update, Wang et al. (2021c) showed that the GEOS-Chem simulated tropospheric NO_2 vertical column density (VCD) agrees better with Ozone Monitoring Instrument (OMI) observed NO_2 VCD for 2005–2019 summer in the U.S., compared with the GEOS-Chem simulation that uses the default soil temperature function. This model improvement further helps explain the slowdown of tropospheric NO_2 VCD reduction during 2009–2019 observed by OMI in the U.S.

2.6 Development of WRF-Chem Emission Preprocessing System (WEPS)

The WEPS Fortran utility is developed to map both global and regional anthropogenic emissions as well as fire emissions for running UI-WRF-Chem simulations. WEPS builds upon a few tools used in the WRF-Chem community (https://www2.acom.ucar.edu/wrf-chem/wrf-chem-tools-community, last access: 10 May 2022). For example, the anthro-emiss utility creates WRF-Chem ready emission files from global anthropogenic emission inventory datasets. There is also another Fortran program (emission_v3.F) to process the U.S. EPA National Emissions Inventory (NEI) 2005 and 2011. Recently, a new tool EPA_ANTHRO_EMIS has been developed to create WRF-Chem ready anthropogenic emission files from Sparse Matrix Operator Kernel Emissions (SMOKE) Modeling System netcdf outputs for NEI 2014 and 2017. We have adopted some of the functionalities in these tools into the WEPS.

Currently in WEPS, we can ingest the following global anthropogenic emission inventories: (1) HTAP_v2.2 (Janssens-Maenhout et al., 2015) and HTAP_v3 (Crippa et al., 2023), created under the umbrella of the Task Force on Hemispheric Transport of Air Pollution (TF HTAP), which is the compilation of different emission inventories over specific regions (North America, Europe, Asia including Japan and South Korea) with the independent Emissions Database for Global Atmospheric Research (EDGAR) inventory filling in for the rest of the world; (2) EDGARv5.0 for year 2015 (Crippa et al., 2020). The HTAP_v3 includes regional emission inventories from U.S. EPA NEI, CAMS-REGv5.1 for Europe, the Regional Emission inventory in Asia (REASv3.2.1), the Clean Air Policy Support System (CAPSS-KU) inventory over South Korea, the JAPAN emission inventory (PM2.5EI and J-STREAM) in Japan and EDGARv6.1 (https://data.jrc.ec.europa.eu/dataset/df521e05-6a3b-461c-965a-b703fb62313e, last access: 1 December 2023) for the rest of the world. It consists of $0.1^\circ \times 0.1^\circ$ grid maps of species: CO, SO_2, NO_x, non-methane volatile organic compound (NMVOC), NH_3, PM_{10}, $PM_{2.5}$, BC and OC for year 2000–2018 (Crippa et al., 2023). Four sectors are included for these species: energy (mainly power industry), industry (manufacturing, mining, metal, cement, etc.), transport (ground transport such as road) and residential (heating/cooling of buildings etc.). For NH_3, an additional sector – agriculture is also included. The datasets have a monthly temporal resolution, and we have interpolated them to daily data. In addition, we have added sector-based diurnal profiles, following the work of Du et al. (2020). For UI-WRF-Chem simulation over the U.S. domain or China domain, we have added the capability to use U.S. EPA NEI 2017 or the Multi-resolution Emission Inventory model for Climate and air pollution research (MEIC) (Zheng et al., 2018; Li et al., 2017b) emission inventory to replace the global emission inventory HTAP_v3, respectively.

For fire emissions, the WEPS can process several emission inventories as described in Zhang et al. (2014). They include: Fire Locating and Modeling of Burning Emissions inventory (FLAMBE) (Reid et al., 2009); Fire INventory from NCAR version 1.0 (FINN v1.01) (Wiedinmyer et al., 2011); Global Fire Emission Database version 3.1 (GFED v3.1) (van der Werf et al., 2010); Fire Energetics and Emissions Research version 1.0 using fire radiative power (FRP) measurements from the geostationary Meteosat Spinning Enhanced Visi-

ble and Infrared Imager (FEER-SEVIRI v1.0) (Roberts and Wooster, 2008; Ichoku and Ellison, 2014); Global Fire Assimilation System (GFAS v1.0) (Kaiser et al., 2012); NESDIS Global Biomass Burning Emissions Product (GBBEP-Geo) (Zhang et al., 2012); Quick Fire Emissions Dataset version 2.4 (QFED v2.4) (Darmenov and Da Silva, 2015). Our recent work involves developing a Visible Infrared Imaging Radiometer Suite (VIIRS) based fire emission inventory, FIre Light Detection Algorithm (FILDA-2) (Zhou et al., 2023). Our past work has mainly focused on OC and BC emissions from the FLAMBE emission inventory (e.g., Ge et al., 2014; Zhang et al., 2022, 2020). We have now included gas species such as CO from FLAMBE emission inventory. The injection height by default is set to range from 500 to 1200 m, based on our previous work (e.g., Yang et al., 2013; Wang et al., 2013; Ge et al., 2017) and users have the option to specify the injection height on their own.

2.7 Updates of WRF-Chem chemistry scheme

The MAIA investigation not only focuses on the total $PM_{2.5}$ and PM_{10} mass but the speciated $PM_{2.5}$ including sulfate, nitrate, BC or EC, OC and dust. We have therefore selected the Regional Acid Deposition Model, Version 2 (RADM2) for gas-phase chemistry (Stockwell et al., 1990) and the Modal Aerosol Dynamics model for Europe (MADE) (Ackermann et al., 1998) and the Secondary ORGanic Aerosol Model (SORGAM) (Schell et al., 2001) as the aerosol module for MAIA model simulations, using WRF-Chem Version 3.8.1. The RADM2-MADE/SORGAM chemistry mechanism in WRF-Chem simulates the above-mentioned aerosol species and has been widely used to study air quality (e.g., Georgiou et al., 2018; Zhang et al., 2020; Tuccella et al., 2012). The MADE/SORGAM aerosol module also includes ammonium, sea salt and water. The aerosol size distribution is represented by the modal approach (Binkowski and Shankar, 1995), which uses three modes (the Aitken, accumulation and coarse mode). A log-normal size distribution and internal mixing of aerosol species are assumed in each mode.

In the MADE/SORGAM aerosol scheme, dust is not explicitly simulated but rather blended into other species. For smaller size bins of dust, they are represented by the unspecified $PM_{2.5}$ chemical species, which have Aitken and accumulation modes. For larger size bins of dust, they are counted as the "soila", which are used for coarse soil-derived aerosol species. To output the dust proportion of the surface $PM_{2.5}$ mass concentration as required by the MAIA project, we add dust species in five size bins (same as the GOCART dust bins in MERRA-2) into the MADE/SORGAM aerosol scheme. This way, when using GEOS FP or MERRA-2 to provide chemical initial and boundary conditions, dust species from the boundary file can also be consistent with the dust species in the aerosol scheme. WRF-Chem currently provides three dust emission schemes: the original GOCART dust emission scheme (Ginoux et al., 2001), GOCART dust emission with the Air Force Weather Agency (AFWA) modifications (LeGrand et al., 2019), and the University of Cologne (UOC) scheme (Shao et al., 2011). Both GOCART and GOCART-AFWA emission schemes release dust in five size bins with lower and upper radius range of 0.1–1, 1–1.8, 1.8–3, 3–6, 6–10 µm, same as the dust size bin used in the MERRA-2 system. The UOC dust emission scheme considers dust in four size bins with lower and upper radius range of 0–1.25, 1.25–2.5, 2.5–5, and 5–10 µm. Here, we have selected the GOCART-AFWA emission scheme in the UI-WRF-Chem framework, which matches the dust size bins in the GEOS FP and MERRA-2 aerosol scheme.

Subsequently, a new chemistry scheme (MADE/SORGAM-DustSS) is created in UI-WRF-Chem to include the dust in five size bins and sea salt aerosols as additional chemical tracers while all other gas and aerosol species are the same as in the MADE/SORGAM scheme. The standard WRF-Chem model currently supports the GOCART sea salt emission scheme, which releases sea salt aerosol species in four bins. The lower and upper radius range of sea salt aerosols species are: 0.1–0.5, 0.5–1.5, 1.5–5.0, 5.0–10 µm. We have then added sea salt aerosols in these four bins into the MADE/SORGAM-DustSS scheme in the UI-WRF-Chem framework. The GOCART sea salt aerosols in MERRA-2 data have five bins with lower and upper radius range as: 0.03–0.1, 0.1–0.5, 0.5–1.5, 1.5–5.0, 5.0–10 µm. This way, the GOCART sea salt aerosols in the aerosol scheme would also match the aerosols in the chemical boundary file provided by MERRA-2 data. In the newly added scheme of MADE/SORGAM-DustSS, we have followed the simple GOCART aerosol scheme in the standard WRF-Chem model to add different transport processes for dust and sea salt aerosol species such as dry deposition. We have also added a simple wet scavenging scheme for dust and sea salt aerosols, which is described more in Sect. 4.2.

Aerosol optical properties such as extinction and single scattering albedo are calculated based on a sectional approach (Barnard et al., 2010) with 8 bins in WRF-Chem, regardless of the aerosol scheme selected. For aerosol species in the MADE/SORGAM-DustSS aerosol scheme, the mass and number concentrations of each aerosol species in the three modes will be matched to the 8 bins. For dust and sea salt aerosol species, the dust and sea salt aerosols in their original 5 and 4 bins, are matched to the 8 bins. In each bin, the particles are assumed to be internally mixed and spherical. The bulk properties such as refractive index for each bin is based on volume approximation. Then, Mie theory is called to calculate the optical properties such as the absorption efficiency and asymmetry parameter for each bin. The optical properties are computed and outputted at four wavelengths (300, 400, 600 and 1000 nm). In addition, the work of Ukhov et al. (2021) has found a few inconsistencies in WRF-Chem related to dust emissions coupled with the GOCART aerosol module, which also impacts other aerosols

schemes such as the MADE/SORGAM module. These inconsistencies were found in the calculation of surface $PM_{2.5}$ and PM_{10} concentration, calculation of aerosol optical properties and estimation of gravitational settling. We have incorporated the corrections of these inconsistencies made by Ukhov et al. (2021) in our UI-WRF-Chem framework.

2.8 Postprocessing and evaluation codes, and repository management

Python-based modules are developed in house to postprocess UI-WRF-Chem hourly outputs as part of the UI-WRF-Chem framework. They include diagnostics of some commonly used variables which are not directly outputted such as relative humidity (RH) and the capability to extract and compile hourly model output into daily output to facilitate file management. We have also created Python modules to evaluate UI-WRF-Chem model performance against ground-based and satellite observations, e.g., comparing model simulated column concentration of trace gases NO_2 with satellite observed column concentration of NO_2. In addition, bash scripts are developed to automatically run UI-WRF-Chem framework for both forecasting and reanalysis modes. It needs minimal work to specify the paths of the codes and data on the servers before running the UI-WRF-Chem model. The UI-WRF-Chem framework uses the GitHub, a git-based version control system to manage its codes and developments. The repository stores the main codes of UI-WRF-Chem. When major developments from our group and collaborators are made and validated, a new version will be released. The WRF-Chem community updates the WRF-Chem code and releases new versions periodically and we also check the major bug fixes and developments to incorporate them in our codes accordingly.

3 Evaluation statistics and model configuration

3.1 Evaluation statistics

Several statistics are used to evaluate the model performance against ground and satellite observations, including linear correlation coefficient (R), root mean square error (RMSE), mean bias (MB), normalized mean bias (NMB), mean absolute error (MAE), normalized standard deviation (NSD) and normalized centered root mean square error (NCRMSE). NSD is the ratio of the standard deviation of the model simulation to the standard deviation of the observation. NCRMSE is like RMSE except that the impact of the bias is removed. Some of these statistics are summarized in a Taylor Diagram (Taylor, 2001), which includes R (shown as the cosine of the polar angle), NSD (shown as the radius from the quadrant center), and NCRMSE (shown as the radius from the expected point, which is located at the point where R and NSD are unity).

To determine whether the performances among model sensitivity simulations for different case studies over different target areas are statistically significant, we conduct the paired t-test on collocated model-observation samples or between model simulations. We focus on the MAE as the evaluation metric. For comparison of hourly data, we account for the temporal autocorrelation by estimating the lag-1 autocorrelation and applying the effective sample size adjustment (Wilks, 2011). For cases with smaller sample size, we also apply the non-parametric Wilcoxon signed rank test (e.g., Menut et al., 2019; Tao et al., 2025) to ensure the robustness of our test. In addition, when multiple model sensitivity simulations are evaluated, we apply a Bonferroni correction procedure (SIMES, 1986) to both paired-t and Wilcoxon tests, following previous work (Crippa et al., 2017). Under this approach, the null hypothesis is rejected if $p \leq \frac{\alpha}{m}$, where p is the raw p value, α is the significance level (0.05 in this study) and m is the number of hypothesis tests. For testing the significance over spatial maps, where a large number of tests are performed simultaneously, we instead apply the Benjamini-Hochberg false discovery rate (FDR) correction (Benjamini and Hochberg, 1995). We hence report adjusted p-value throughout this work unless noted otherwise.

3.2 Model configuration

All the UI-WRF-Chem model simulations for MAIA target areas are set up as 2 nested domains (Fig. 2) with a $4\,\text{km} \times 4\,\text{km}$ horizontal spatial resolution for the inner domain (D2) focusing on the MAIA target area and a $12\,\text{km} \times 12\,\text{km}$ horizontal spatial resolution for a larger outer domain (D1). The inner and outer domain have nominal dimension of $\sim 360\,\text{km}$ (east-west) $\times\, 480\,\text{km}$ (north-south) and $\sim 1080\,\text{km}$ (east-west) $\times\, 1000\,\text{km}$ (north-south), respectively. Both domains have 48 vertical levels extending from the surface to 50 hPa. For the inner domain (D2), we have turned off the cumulus scheme to let the model fully resolve the convective process while all other model configurations are kept the same for both domains. A summary of model configurations regarding different schemes used for the four targets areas is provided in Table 1. For each target area, we first run a suite of sensitivity simulations to test the model sensitivity to different physics schemes by evaluating model simulated meteorology variables with ground observations and then select the optimal combination of physics schemes based on evaluation results. A description of the satellite and ground observation datasets used are provided in Sect. S1 in the Supplement.

There are many physics schemes that can be used in WRF-Chem. We select the commonly used schemes for each target area based on literature review and our previous work (e.g., Yang et al., 2013; Sha et al., 2021; Zhang et al., 2022). We also consider a few other factors as described below. For the cumulus scheme, we consider the Grell 3D ensemble (G3D, Grell and Dévényi, 2002) scheme, which also accounts for

Table 1. A summary of model physics, chemistry and emissions configurations for CHN-Beijing, ITA-Rome, USA-LosAngeles, and USA-Atlanta target areas.

Category	Model component	CHN-Beijing	ITA-Rome	USA-Los Angeles	USA-Atlanta
Physics	Microphysics	Lin	Morrison	Lin	Lin
	Cumulus	G3D	G3D	G3D	G3D
	Longwave radiation	RRTMG	RRTMG	RRTMG	RRTMG
	Shortwave radiation	RRTMG	RRTMG	RRTMG	RRTMG
	Planetary boundary layer	YSU	YSU	YSU	YSU
	Surface layer	Revised MM5			
	Land surface model	Noah	Noah	Noah	Noah
Chemistry	Gas-phase	RADM2	RADM2	RADM2	RADM2
	Aerosols	MADE/SORGAM-DustSS			
	Photolysis	Madronich F-TUV			
Emissions	Anthropogenic emissions	MEIC 2016	HTAP v3 (2018)	NEI 2017	NEI 2017
	Dust emissions	GOCART with AFWA modifications			
	Biogenic emissions of VOCs	MEGAN	MEGAN	MEGAN	MEGAN
	Soil NO_x emissions	BDISNP	BDISNP	BDISNP	BDISNP
	Wildfire emissions	FLAMBE	FLAMBE	FLAMBE	FLAMBE

cloud radiation feedback. For model spatial grids greater than 10 km, they usually rely on the cumulus parameterization to determine the subgrid convective processes. For model spatial grids smaller than 10 km, it is generally considered as the convective gray zone, where the use of convective parameterization or explicit resolving treatment of the convective process remains to be an ongoing question (Jeworrek et al., 2019). Typically, for model spatial grids larger than 5 km, convective parameterization has been used in regional model studies (e.g., Zhang and McFarlane, 1995; Clark et al., 2009; Dudhia, 2014). For model spatial grids smaller than 5 km, generally considered convection-permitting scale, numerous regional model studies have suggested to turn off the cumulus scheme (e.g., Prein et al., 2015; Wang et al., 2021b; Weisman et al., 1997; Weisman et al., 2008; Done et al., 2004; Gao et al., 2017), especially if the cumulus scheme is not scale-aware (Wagner et al., 2018). Therefore, we have chosen to turn off the cumulus scheme here for the inner domain (D2) with the 4 km spatial resolution.

With the current version (WRF-Chem v3.8.1) of the code, chemical species are transported using the G3D scheme, regardless of which cumulus scheme is used, while other scalars are transported with the selected cumulus scheme. Therefore, the G3D scheme is used to ensure the consistency between chemistry and physics. Additionally, WRF-Chem v3.8.1 was selected as the base version at the beginning of this project due to its stability. We have maintained this version over the course of the project to ensure the consistency and reproducibility of the results. Although there are several scale-aware cumulus schemes available in WRF-Chem such as the Kain-Fritsch scheme (KF, Kain, 2004) and the Grell-Freitas scheme (GF, Grell and Freitas, 2014), only the GF scheme has been updated to ensure the consistent transport of both chemical species and other scalars, as described by Li et al. (2018, 2019). We acknowledge the limitation of using only the G3D scheme in this work and plan to update the UI-WRF-Chem modeling framework to a newer version to enable the use of the GF scheme and incorporate other recent improvements as well.

For the microphysics scheme, an inexpensive scheme is typically sufficient for model spatial grids greater than 10 km but a more complex scheme that accounts for the prediction of the mixed phases (6-class schemes, including graupel) and number concentrations (double-moment schemes) is required (Han et al., 2019). Therefore, we consider these three schemes in the current work: the Lin scheme (Lin et al., 1983; Chen and Sun, 2002), the WRF Single-Moment 6-Class Microphysics Scheme (WSM6) (Hong and Lim, 2006) and the Morrison scheme (Morrison et al., 2009). The former two is a single-moment 6 class scheme and the latter one is a double-moment scheme, which also predicts the number concentration of the hydrometer besides the total amount. All the three schemes include the simulations of graupel which is shown to help with the simulation of convection for higher resolution simulation (Brisson et al., 2015). At convective-permitting scales, the graupel size representation could play a more important role in the precipitation prediction than the number of moments (single vs. double) in certain cases (Adams-Selin et al., 2013).

For the shortwave radiation scheme, we only consider the two-stream multiband Goddard scheme (Chou et al., 1998) and the Rapid Radiative Transfer Model for GCMs (RRTMG) (Iacono et al., 2008), which both include the direct aerosol radiation feedback. For the longwave radiation,

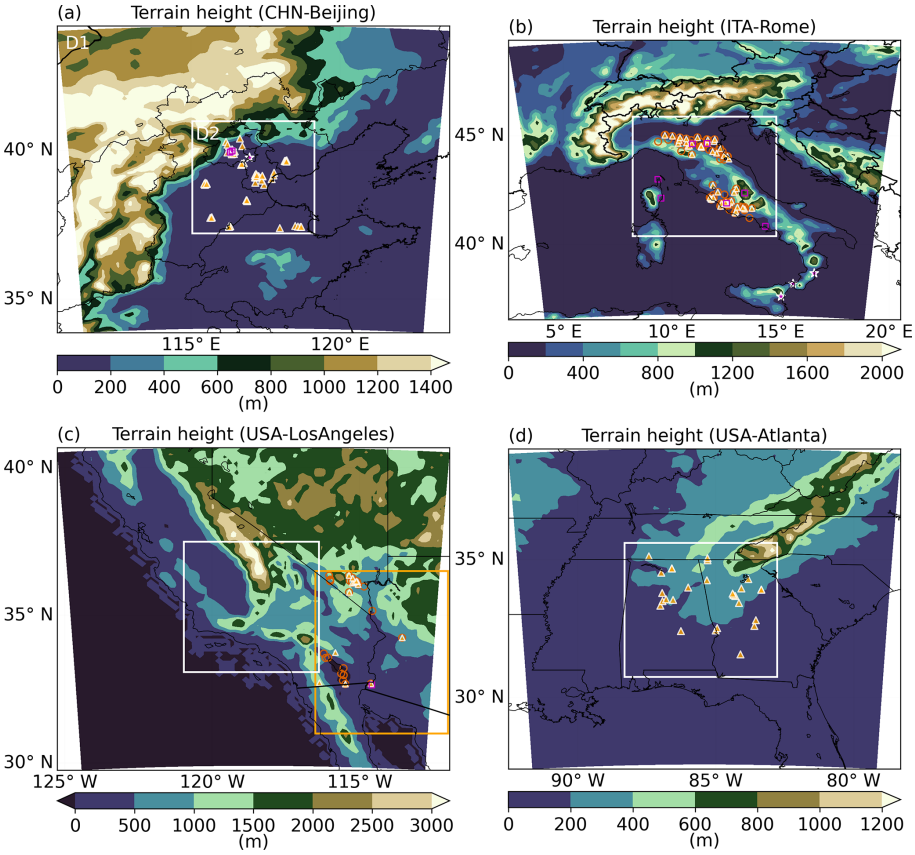

Figure 2. Terrain height for **(a)** CHN-Beijing, **(b)** ITA-Rome, **(c)** USA-LosAngeles and **(d)** USA-Atlanta target areas of the 2 nested domains: the outer domain (D1) and the inner domain (D2) shown as the white box. For **(a)**, the orange filled triangles represent the ground observation sites of $PM_{2.5}$ and PM_{10} mass concentration. Both open magenta squares and stars represent the AERONET ground observation sites. The sites denoted by the stars are used to constrain the dust particle size distribution as described in Sect. 4.1, while the sites denoted by squares are used to evaluate model simulated AOD. **(b)** is same as **(a)**, except that the orange open circles represent ground observations of PM_{10} mass concentration, and orange filled triangles are the ground observations sites of $PM_{2.5}$ mass concentration. **(c)** is the same as **(b)** except that the orange box is defined as the dust-prone region, which is used to tune dust emissions. For **(d)**, orange filled triangles represent the ground observation sites of $PM_{2.5}$ mass concentration.

we select the RRTMG and the Rapid Radiative Transfer Model (RRTM) schemes (Mlawer et al., 1997). RRTMG for both shortwave and longwave radiation schemes are recommended to pair together in the model by the developing team of WRF-Chem. For the planetary boundary layer (PBL) scheme and the corresponding surface layer scheme, we consider the nonlocal boundary layer scheme – the Yonsei University scheme (YSU, (Hong et al., 2006)) with the revised fifth-generation Pennsylvania State University – National Center for Atmospheric Research Mesoscale Model (MM5) (Grell et al., 1994; Jiménez et al., 2012) surface layer scheme. We also consider two commonly used local boundary layer schemes: Mellor-Yamada-Janjic (MYJ, (Janjic, 2001)) with the ETA similarity surface layer scheme; Mellor-Yamada-Nakanishi-Niino level 2.5 (MYNN2.5, (Nakanishi and Niino, 2004)) with the MYNN surface layer scheme. When using the YSU scheme, we also turn on the surface drag parameterization (Jiménez and Dudhia, 2012) to improve topographic effects on surface winds over a complex terrain. The land surface model is the Noah land model (Chen and Dudhia, 2001), which incorporates our updates of the land surface properties as described in Sect. 2.4. Additionally, for a specific target area, other physics schemes not mentioned here but commonly used in that area will also be tested.

Details regarding the selection and evaluation results of the physics scheme for the four target areas are available in Sect. S2. Here, we provide a summary of the evaluation results. Sensitivity simulations performed for each target area are listed in Table S1 and we focus on testing the following schemes: microphysics, shortwave and longwave radiation and PBL. We evaluate four UI-WRF-Chem simulated meteorology variables with surface observations: air temperature at 2 m (t2), dew temperature at 2 m (dewt2) or relative humidity (RH), wind speed at 10 m (wspd10) and sea level pressure (pres). Results of the hourly or 3-hourly evaluation

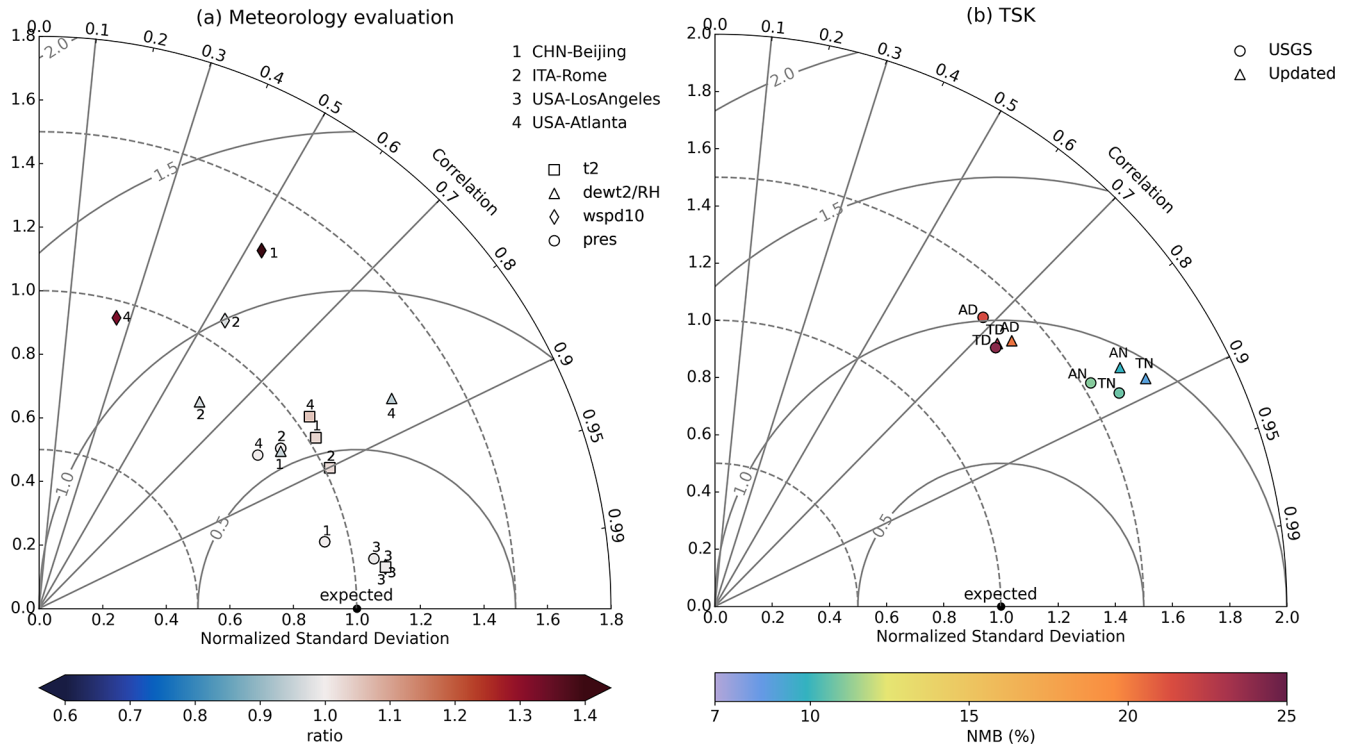

Figure 3. Taylor Diagrams for evaluating UI-WRF-Chem model simulated **(a)** meteorological variables (t2, dewt2 or RH, wspd10 and pres) with ground observations for CHN-Beijing, ITA-Rome, USA-LosAngeles and USA-Atlanta target areas, and **(b)** surface skin temperature (TSK) with MODIS observed land surface temperature (LST) for CHN-Beijing during July 2018. In **(a)**, evaluation results of daily meteorology variables are based on the model final configuration for each target area (Table 1). Color bar represents the ratio between model results and ground observations. In **(b)**, USGS and updated refer to the UI-WRF-Chem sensitivity simulations 2N_def (default USGS land cover type and subsequently derived GVF, LAI and albedo) and 2N_upd (updated land cover type, GVF, LAI and albedo with MODIS land data) in Table 2, respectively. UI-WRF-Chem simulated TSK averaged over the Terra and Aqua overpass time during daytime (TD and AD) and nighttime (TN and AN), respectively are compared to the corresponding Terra and Aqua observations. Color bar represents the normalized mean bias (NMB) between model results and satellite observations.

of the meteorology variables are summarized in Table S2 and Fig. S1. Overall, all the sensitivity simulations of t2 and pres for all the target areas show the highest correlation (> 0.8). Dewt2 or RH also show good correlation (0.59–0.84) with ITA-Rome showing the lowest correlation. The case study of ITA-Rome is conducted over June 2023, where some regions in Italy experienced rainfall events about one third of the month. Uncertainties of UI-WRF-Chem capturing the rainfall events (discussed in Sect. 4.2) could result in the lower correlation of RH. Comparatively, wspd10 shows lower correlation (0.22–0.52) over USA-Atlanta. Across the target areas, we find that wspd10 is most sensitive to the PBL scheme compared with other schemes tested, which is also found in previous studies (e.g., Yu et al., 2022). It is found that no single combination of the physics scheme will result in the best performance for each meteorology variable evaluated. The interaction of these different parameterized processes mentioned above (e.g., convection, boundary layer mixing, microphysics and radiation) are complex (Prein et al., 2015) and it is region, case and variable specific. Therefore, model performance can vary from region to region or case to case.

Based on the evaluation results, we select the optimal combination of various physics schemes tested as the final configuration for each target area (Tables S1 and 1). We summarize the statistics of the evaluation of the daily meteorology variables for the four target areas in Fig. 3a, for the final configuration only. We find that UI-WRF-Chem simulated daily t2, dewt2 and pres all show high correlation (> 0.7) and low NMB ($-10\,\%$ to $+10\,\%$) across the target areas. For evaluation of daily wspd10, correlation increases, and bias decreases compared with hourly evaluation. For USA-Atlanta, the daily wspd10 still shows lower correlation (~ 0.25) compared with other target areas. The sensitivity simulation over USA-Atlanta is conducted over June 2022 and majority of the wspd10 are under $5\,\mathrm{m\,s^{-1}}$. It can be challenging for the model to capture this stable condition very well. Future work could focus on trying nudging with ground observation to improve the model performance over this area. We also recognize that our sensitivity tests are limited to one month for

each target area. We are not able to test the performance for different seasons. Nevertheless, it provides values for understanding the model sensitivity to different schemes at different locations.

Biogenic emissions for VOCs are from the MEGAN scheme and soil NO_x emissions are from the BDISNP scheme. Fire emissions are from the FLAMBE emission inventory and dust emissions use the GOCART with AFWA modification. Here, we use MEIC 2016 as the anthropogenic emission for CHN-Beijing and NEI 2017 emission inventory for USA-LosAngeles and USA-Atlanta. The HTAP_v3 2018 is used for ITA-Rome. The gas-phase chemistry is the RADM2, and the aerosol module is the newly added scheme MADE/SORGAM-DustSS: the MADE/SORGAM scheme with the addition of dust and sea salt aerosol species as described in Sect. 2.7. Lastly, we use the Madronich Fast Tropospheric UV and Visible Radiation Model (F-TUV) as the photolysis scheme (Madronich, 1987; Tie et al., 2003).

4 Case studies for different target areas

4.1 Case study – CHN-Beijing

Beijing and its surrounding area in China, are affected by both local and regional emissions as well as long-range transport (Wu et al., 2021; Zhang et al., 2018). In recent decades, the North China Plain including the Beijing area has experienced severe PM pollution problems as a result of the rapid economic growth and urbanization (Zhang et al., 2016). In addition to the impacts of anthropogenic emission on surface PM levels, strong dust storms from the Taklamakan Desert and the Gobi Desert sometimes can be transported downwind to the Beijing area and affect local air quality in the springtime. Here for the CHN-Beijing target area (Fig. 2a), we first focus on a dust intrusion event during 24–31 March 2018, to study the impacts of chemical boundary conditions on surface PM. Figure 4 shows the MODIS Aqua observed AOD over part of China for the period of this event. The dust storm can be seen on 26 March 2018, at both Taklamakan and Gobi Deserts and by 28 March, strong dust clouds have been transported to Beijing and its surrounding areas. Figure S2 displays the movement of surface observations of daily PM_{10} mass concentration across China from 24 March to 31 March 2018. On 27 and 28 March 2018, high surface PM_{10} concentration were observed in Beijing, Tianjin and Hebei province with hourly concentration exceeding $1000\,\mu g\,m^{-3}$ (not shown here). Then, we focus on July 2018 to study the impacts of updating land surface properties and soil NO_x emission scheme on model performances.

4.1.1 Sensitivity experiment design

For CHN-Beijing target area, we carry out a suite of sensitivity simulations using the UI-WRF-Chem framework as shown in Table 2 to investigate the impacts of chemical boundary conditions, updated land surface properties and soil NO_x emission scheme on model performance. First, three simulations are conducted during March 2018 to study the impacts of using MERRA-2 data to provide chemical boundary conditions on model performance. Additionally, four simulations are carried out for July 2018 to investigate the impacts of updating land surface properties as well as surface soil NO_x emission scheme. The simulation with "2N_def" uses the default USGS land cover type and subsequently derived GVF, LAI and albedo, using a predefined look-up table. The simulations with "2N_upd" uses the corresponding updated land cover type, GVF, LAI and albedo, based on the MODIS land data products for the simulation period, as described in Sect. 2.4. The simulations with "2N_*_snox*" use our newly developed BDISNP soil NO_x emission scheme.

The impacts of chemical boundary conditions are evaluated from several sensitivity experiments. In the simulation "2N_upd_ snox-none", no chemical species from MERRA-2 data are transported into the domain. In the simulation "2N_upd_ snox-dust", dust and other aerosols including sulfate, BC and OC are considered in the chemical boundary condition from MERRA-2 data. Furthermore, to constrain the chemical boundary condition for the allocation of dust concentration as a function of different size bins, we analyze the AERONET measured aerosol volume size distribution (AVSD) data from 2000 to 2020. If the fine mode fraction (FMF) of AOD at 500 nm is less than 0.3 (Lee et al., 2017), it is considered as a dust event. Figure 5a shows the averaged dust particle size distribution (PSD) over the AERONET sites (Fig. 2a) between 2000–2020 from both AERONET and MERRA-2 data for all the dust events that occurred in CHN-Beijing. The ratio between the mean of the AERONET PSD and MERRA-2 PSD for each of the five dust size bins is then used as a constraint to scale the dust concentration in each bin in the MERRA-2 chemical boundary data. The sensitivity run "2N_upd_snox-dust PSD" in Table 2 is based on this result.

Three UI-WRF-Chem sensitivity simulations in Table 2 are run from 18 to 31 March 2018, for evaluating the impacts of using MERRA-2 data to provide chemical boundary conditions. The simulation results with the first 6 d are used as initialization. Model output from 24 to 31 March 2018, are used for analysis, unless noted otherwise. The rest of the four simulations are used for evaluating the impacts of updating land surface properties and soil NO_x emission scheme on model performance. They are carried out from 24 June to 31 July 2018, and model outputs from 1 to 31 July are used for data analysis. We mainly use model output from the inner domain (D2) for data analysis unless noted otherwise.

4.1.2 Impacts of chemical boundary conditions on surface PM and AOD

First, we evaluate the effectiveness of using MERRA-2 data to provide chemical boundary conditions in capturing this

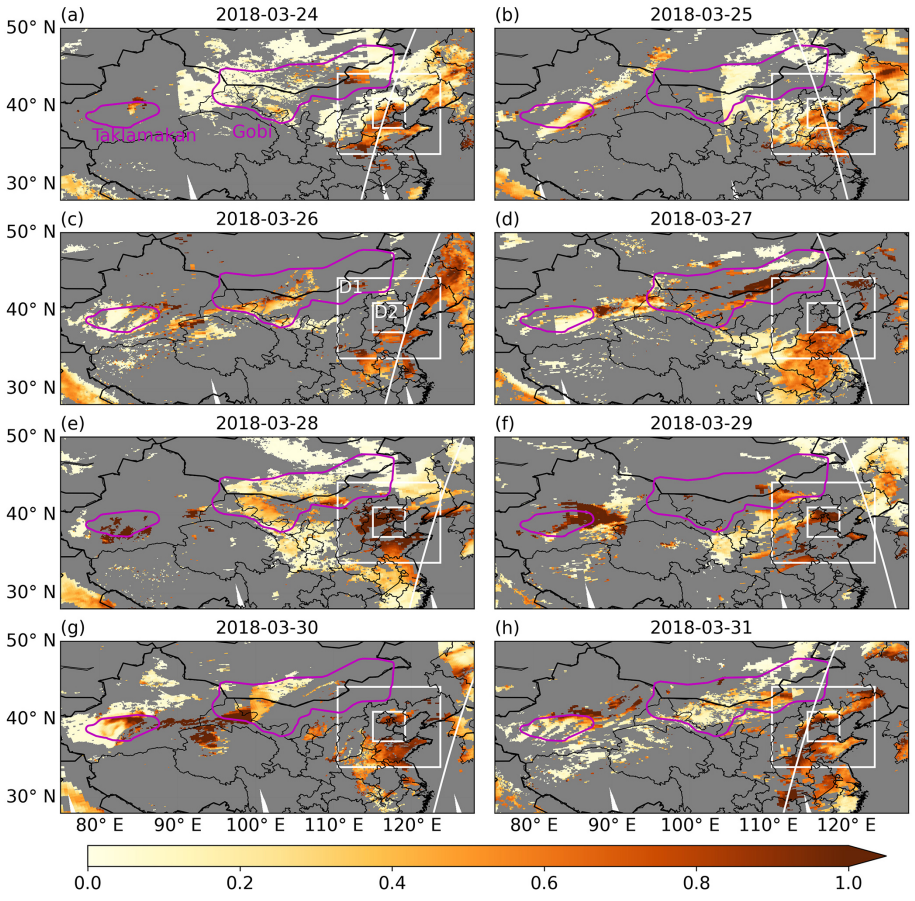

Figure 4. (a–h) MODIS Aqua Deep Blue (DB) AOD from 24–31 March 2018. The white boxes represent the UI-WRF-Chem 2 nested domains for outer (D1) and inner domain (D2) over CHN-Beijing, respectively. The white diagonal lines indicate the CALIOP tracks. The magenta contour lines represent the boundaries of Taklamakan and Gobi Deserts.

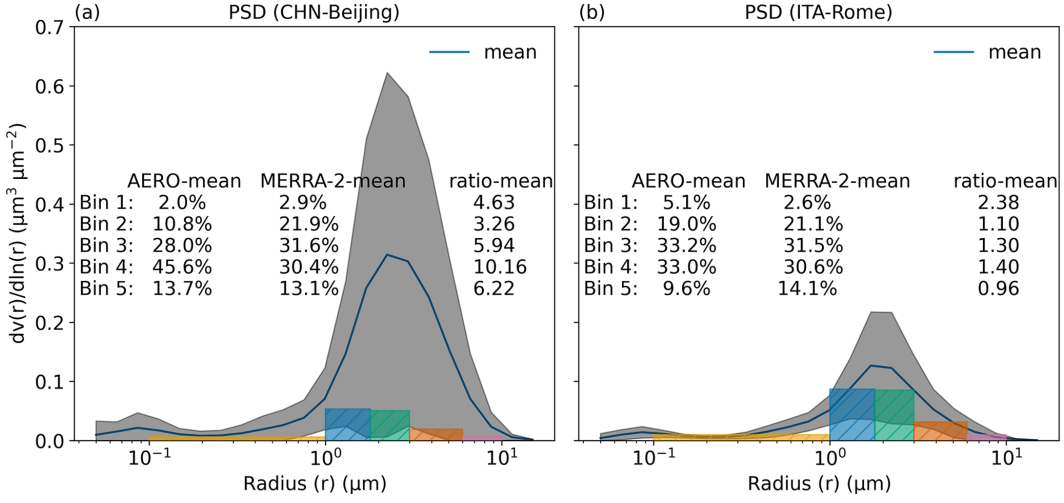

Figure 5. Averaged particle size distribution (PSD) from AERONET observations (blue line) and MERRA-2 data (the 5 colored bins) for **(a)** CHN-Beijing and **(b)** ITA_Rome over 2000–2020 and 2000–2023, respectively. The AERONET sites used are shown as stars in Fig. 2a and b, respectively. The dark gray areas represent the AERONET variability. AERO-mean and MERRA-2 mean represent the fraction of the PSD from each bin over the sum of the 5 bins. Ratio-mean is the ratio of the total PSD of AERONET over MERRA-2 for each bin.

Table 2. A suite of UI-WRF-Chem sensitivity simulations with different chemical boundary conditions, land data and soil NO_x emission schemes for CHN-Beijing.

simulation name[a]	land data[b]	soil NO_x emission[c]	species considered in the chemical boundary[d]	simulation time[e]
2N_upd_snox-none	updated	BDISNP	none	03/2018
2N_upd_snox-dust	updated	BDISNP	dust + other aerosols	03/2018
2N_upd_snox-dust PSD	updated	BDISNP	dust PSD + other aerosols	03/2018
2N_def	USGS	Guenther	dust + other aerosols	07/2028
2N_upd	updated	Guenther	dust + other aerosols	07/2018
2N_upd_MEGAN	updated	MEGAN	dust + other aerosols	07/2018
2N_upd_BDISNP	updated	BDISNP	dust + other aerosols	07/2018

[a] The simulation name starting with "2N*" refers to the 2 nested domains used for CHN-Beijing as shown in Fig. 2a. The 2 nested domains have a horizontal spatial resolution of 4 km × 4 km and 12 km × 12 km for the inner and outer domain, respectively.
[b] We test different land surface properties used for the UI-WRF-Chem static input data. The simulation name with "*def*" refers to the use of USGS land cover type data and subsequently derived GVF, LAI and albedo, with a predefined look-up table. The simulation name with "*upd*" refers to the use of updated land cover type, GVF, LAI and albedo data with MODIS land data products.
[c] We test different soil NO_x emission schemes. The Guenther scheme calculates biogenic emissions including soil NO_x emissions, without any external input datasets needed. The MEGAN scheme requires external input files to calculate biogenic emissions including soil NO_x emissions. The BDISNP is our newly developed scheme. Since the USGS land data is only compatible with the Guenther scheme, we conduct sensitivity simulations "2N_def" and "2N_upd" to evaluate the impacts of updating land surface properties. The simulation name with "*snox*" means that the BDISNP soil NO_x emission scheme is used.
[d] We test different scenarios of chemical species used in MERRA-2 data for updating UI-WRF-Chem chemical boundary conditions. "None" (simulation name with "*none*") means that chemical boundary conditions from MERRA-2 data are not used but instead the model default chemical boundary conditions are used. They represent a clean North American summer day, which includes a limited number of chemical species and most of them are gas species. For aerosol species, the concentrations are close to zero values. "dust + other aerosols" (simulation name with "*dust*") means that dust and other aerosols including sulfate, BC and OC are considered in the chemical boundary conditions from MERRA-2 data. "dust particle size distribution (PSD) + other aerosols" (simulation name with "*dust PSD*") is the same as "dust + other aerosols" except that we use the ratio of averaged PSD from AERONET observations and MERRA-2 data over 2000–2020 to scale the dust concentration for each size bin in the MERRA-2 data. More details can be found in Sect. 4.1.1.
[e] We conduct the sensitivity simulations in two different time periods: March and July 2018, respectively. The simulations in March focus on evaluating the impacts of using MERRA-2 data to provide chemical boundary conditions on model performance while the simulations in July focus on the impacts of updating land surface properties with MODIS data and soil NO_x emission scheme.

dust long-range transport event in spring 2018. Figure 6 shows the overall evaluation of model simulated hourly surface $PM_{2.5}$ mass concentration against ground observations over PTA-Beijing during 24–31 March 2018. Results are presented for three sensitivity experiments, as described in Sect. 4.1.1. WRF-Chem PM data are regridded onto the MERRA-2 grid to ensure a fair comparison. Without considering any chemical species in the boundary, the UI-WRF-Chem simulated $PM_{2.5}$ concentration (2N_upd_snox-none) substantially underestimates ground observations with a MB of $-66.4\,\mu g\,m^{-3}$. After including dust and other aerosols in the boundary conditions, the UI-WRF-Chem simulated $PM_{2.5}$ concentration (2N_upd_snox-dust) increases from 18.7 to $35.5\,\mu g\,m^{-3}$ and thus reduces the MB to $-49.6\,\mu g\,m^{-3}$. The correlation (R) increases from 0.19 to 0.51 and MAE decreases from 66.7 to $50.2\,\mu g\,m^{-3}$ (paired t-test, adjusted $p < 0.05$; Bonferroni correction). By constraining the dust PSD in the MERRA-2 data with the AERONET climatology data, the UI-WRF-Chem simulated $PM_{2.5}$ (2N_upd_snox-dust PSD) further improves the model performance with MB of $-24\,\mu g\,m^{-3}$, R of 0.54 and MAE of $37.0\,\mu g\,m^{-3}$ (paired t-test, adjusted $p < 0.05$; Bonferroni correction). This sensitivity simulation also outperforms the MERRA-2 simulated surface $PM_{2.5}$ concentration with MB of $-33.7\,\mu g\,m^{-3}$, R of 0.39 and MAE of $41.7\,\mu g\,m^{-3}$ (paired t-test, adjusted $p < 0.05$; Bonferroni correction).

Figures 7a and S3 show the time series of hourly surface $PM_{2.5}$ and PM_{10} concentration from 24–31 March 2018 for both model simulations and ground observations. During 27–28 March, when the dust front intruded PTA-Beijing, hourly observations of surface $PM_{2.5}$ and PM_{10} concentration averaged over all the sites could reach approximately 150 and $900\,\mu g\,m^{-3}$, respectively. The UI-WRF-Chem simulation without chemical boundary conditions (2N_upd_ snox-none) misses this peak for both $PM_{2.5}$ and PM_{10} while both the UI-WRF-Chem simulation with chemical boundary condition (2N_upd_snox-dust) and MERRA-2 data capture this peak for $PM_{2.5}$ but miss the peak for PM_{10}. The UI-WRF-Chem simulation with dust PSD constrained (2N_upd_snox-dust PSD) capture the peaks of both $PM_{2.5}$ and PM_{10}. Compared with the simulation without boundary conditions (2N_ upd_snox-none), adding chemical boundary conditions (2N_upd_snox-dust) improves model performance with increased correlation for both $PM_{2.5}$ (0.41 to 0.72) and PM_{10} (0.06 to 0.23). The simulation with dust PSD constrained (2N_upd_snox-dust PSD) does not improve the correlation of $PM_{2.5}$ (0.65) but does for PM_{10} (0.28), compared with the simulation using dust in the chemical boundary (2N_upd_snox-dust). Time series of UI-WRF-Chem simulated hourly speciated $PM_{2.5}$ (e.g., OC, EC, sulfate, nitrate) and dust components in both $PM_{2.5}$ and PM_{10} from the two sensitivity simulations (2N_upd_snox-dust and 2N_ upd_snox-dust PSD) (not shown here) indicate that only the dust components exhibit similar peaks as in the total $PM_{2.5}$ and PM_{10}, while other speciated $PM_{2.5}$ components do not follow the same temporal pattern. This demonstrates that the

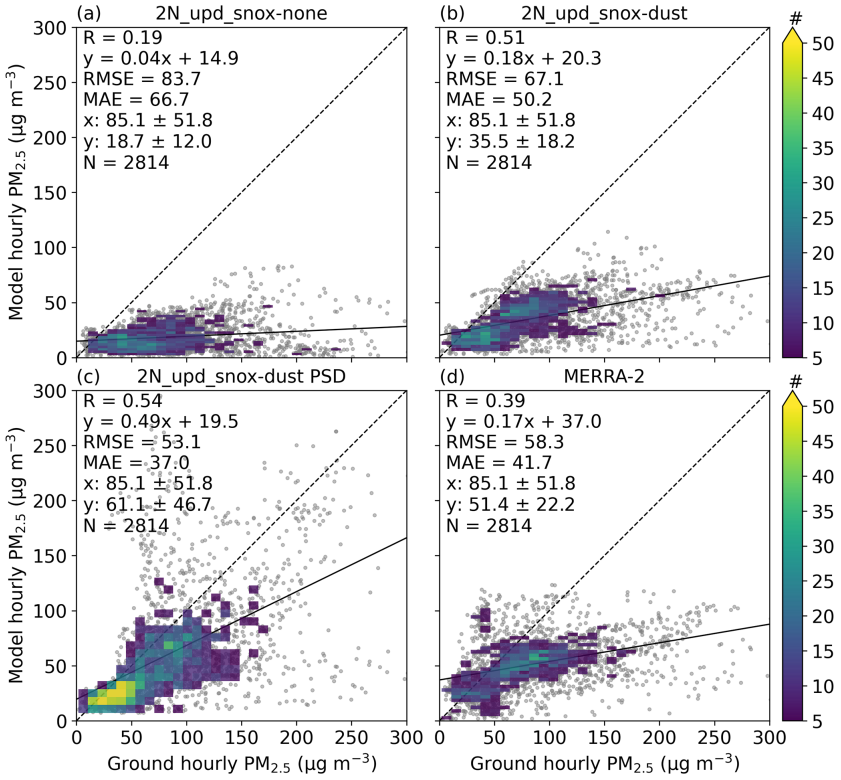

Figure 6. Scatter plot of hourly surface $PM_{2.5}$ concentration between model (y axis) and ground observation (x axis) for surface sites in the inner domain (D2) of CHN-Beijing for 24–31 March 2018. **(a)**–**(c)** refer to the UI-WRF-Chem sensitivity simulations with different chemical boundary conditions being considered using MERRA-2 data (Table 2). **(a)** no chemical species, **(b)** dust and other aerosols and **(c)** same as **(b)** except that the dust concentration is scaled based on constraining MERRA-2 dust PSD data with AERONET PSD climatology data. **(d)** is from MERRA-2 simulated surface $PM_{2.5}$ concentration. Also shown on the scatter plot is the correlation coefficient (R), the root-mean-square error (RMSE), the mean absolute error (MAE), the mean ± standard deviation for observed (x) and model-simulated surface $PM_{2.5}$ (y), the number of collocated data points (N), the density of points (the color bar), the best fit linear regression line (the solid black line) and the 1 : 1 line (the dashed black line). WRF-Chem PM data are regridded onto the MERRA-2 grid, and when multiple surface sites fall within the same MERRA-2 grid, the observations are then averaged to represent a single collocated site.

observed peaks in both $PM_{2.5}$ and PM_{10} are primarily driven by the dust intrusion event. Moreover, the magnitude of the peak from the sensitivity simulation – 2N_upd_snox-dust PSD is larger and matches better with surface observations, especially for PM_{10}, than that of the 2N_upd_snox-dust. This further highlights the effectiveness of our method in improving the representation of dust size distribution in MERRA-2 data.

Not only does considering chemical boundary conditions improve surface PM mass concentration, it also enhances the total aerosol column amount and vertical distribution. Figure 7b–d shows the AOD evaluation between model simulations and AERONET observations. Without considering boundary conditions, the UI-WRF-Chem simulation (2N_upd_snox-none) significantly underestimates the AERONET observed AOD (0.05 vs. 0.73) and shows poor correlation (0.02). Including dust and other aerosols (2N_upd_snox-dust) increases UI-WRF-Chem simulated AOD (0.29), improves correlation (0.79) and reduces MAE from 0.67 to 0.44 (paired t-test, adjusted $p > 0.05$; Wilcoxon, adjusted $p < 0.05$; Bonferroni correction). Further constraining the dust in the boundary (2N_upd_snox-dust PSD) yields the best model performance with simulated AOD of 0.93 and correlation of 0.83, reducing MAE from 0.44 to 0.31 (paired t-test, adjusted $p > 0.05$; Wilcoxon, adjusted $p < 0.05$; Bonferroni correction). The paired t-test does not find statistically significant changes in the MAE, likely due to the smaller sample size, whereas the Wilcoxon test shows that changes in the MAE are statistically significant.

We then compare the UI-WRF-Chem simulated vertical aerosol profile with the Cloud-Aerosol Lidar with Orthogonal Polarization (CALIOP) data for the outer domain (D1) during 26–28 March, when dust reaches the PTA-Beijing domain. Figure 8 shows the CALIOP derived aerosol extinction coefficient, aerosol type as well as UI-WRF-Chem simulated extinction coefficient. The CALIOP ground tracks are located within the UI-WRF-Chem outer domain (D1)

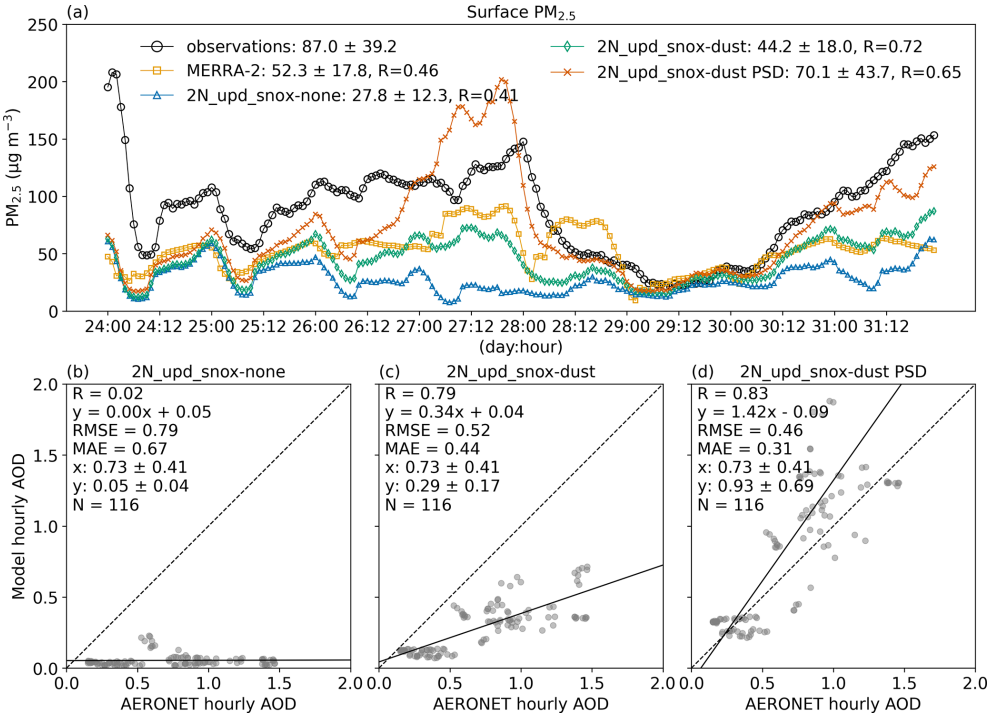

Figure 7. (a) time series of hourly surface $PM_{2.5}$ concentration averaged over surface sites in the inner domain (D2) of CHN-Beijing for 24–31 March 2018, from model simulations and ground observations. 2N_upd_snox-none/dust/dust PSD refer to the UI-WRF-Chem sensitivity simulations with different chemical boundary conditions being considered using MERRA-2 data (Table 2): no chemical species; dust and other aerosols; dust concentration is scaled based on constraining MERRA-2 dust PSD data with AERONET PSD climatology data. Also shown on the plot is the mean ± standard deviation of surface $PM_{2.5}$ for model simulations or observations as well as the correlation coefficient (R). **(b–d)**: scatter plot of hourly AOD between model (y axis) and AERONET observation (x axis) for 24–31 March 2018. Also shown on the scatter plot is R, the root-mean-square error (RMSE), the mean absolute error (MAE), the mean ± standard deviation for observed (x) and model-simulated AOD (y), the number of collocated data points (N), the best fit linear regression line (the solid black line) and the 1 : 1 line (the dashed black line).

(Fig. 4) and model grids that overlap with the tracks are selected. From both CALIOP aerosol extinction coefficient and aerosol type, we can see that dust is dominating the vertical distribution above ∼ 3–4 km and mixed with marine and anthropogenic aerosols in the boundary layer. Without considering aerosols in the chemical boundary conditions, the UI-WRF-Chem simulated extinction coefficient is negligible above the boundary layer (not shown here). After considering dust and other aerosols in the chemical boundary, we can see the increase in the extinction coefficient in the vertical distribution (Fig. 8g–i). Constraining the dust PSD in the boundary (2N_upd_snox-dust PSD, Fig. 8j–l) further enhances the vertical distribution of the aerosol extinction coefficient, which matches better with the CALIOP observations. This reflects the effectiveness of including dust and other aerosols in the chemical boundary condition to better capture the vertical distribution of aerosol properties in this dust intrusion event. We note that CALIOP data is also subject to uncertainties of the lidar ratio used in deriving the extinction, and so is the extinction modeled by UI-WRF-Chem (Yang et al., 2013). Hence, CALIOP data is used as a relative reference to assess the model improvement.

Since PTA-Being is located downwind of the dust source regions in this case, there could be uncertainties in simulating the transport of different dust size bins in MERRA-2 data from source regions. Thus, our constraining method could provide an effective way to improve the dust size distribution in the boundary conditions and subsequently improve model simulated surface PM concentration as well as vertical distribution of aerosols. This method could also benefit other PTAs such as ITA-Rome, that can be affected by dust transport events, which will be discussed in Sect. 4.2.

4.1.3 Impacts of updated land surface properties on model performance

The UI-WRF-Chem model simulated surface skin temperature (TSK) is evaluated with satellite observations of land surface temperature (LST) from MODIS onboard Terra and Aqua for July 2018. We first regrid the MODIS daily LST data onto the WRF-Chem model grid, and then mask the WRF-Chem output based on the spatial and temporal avail-

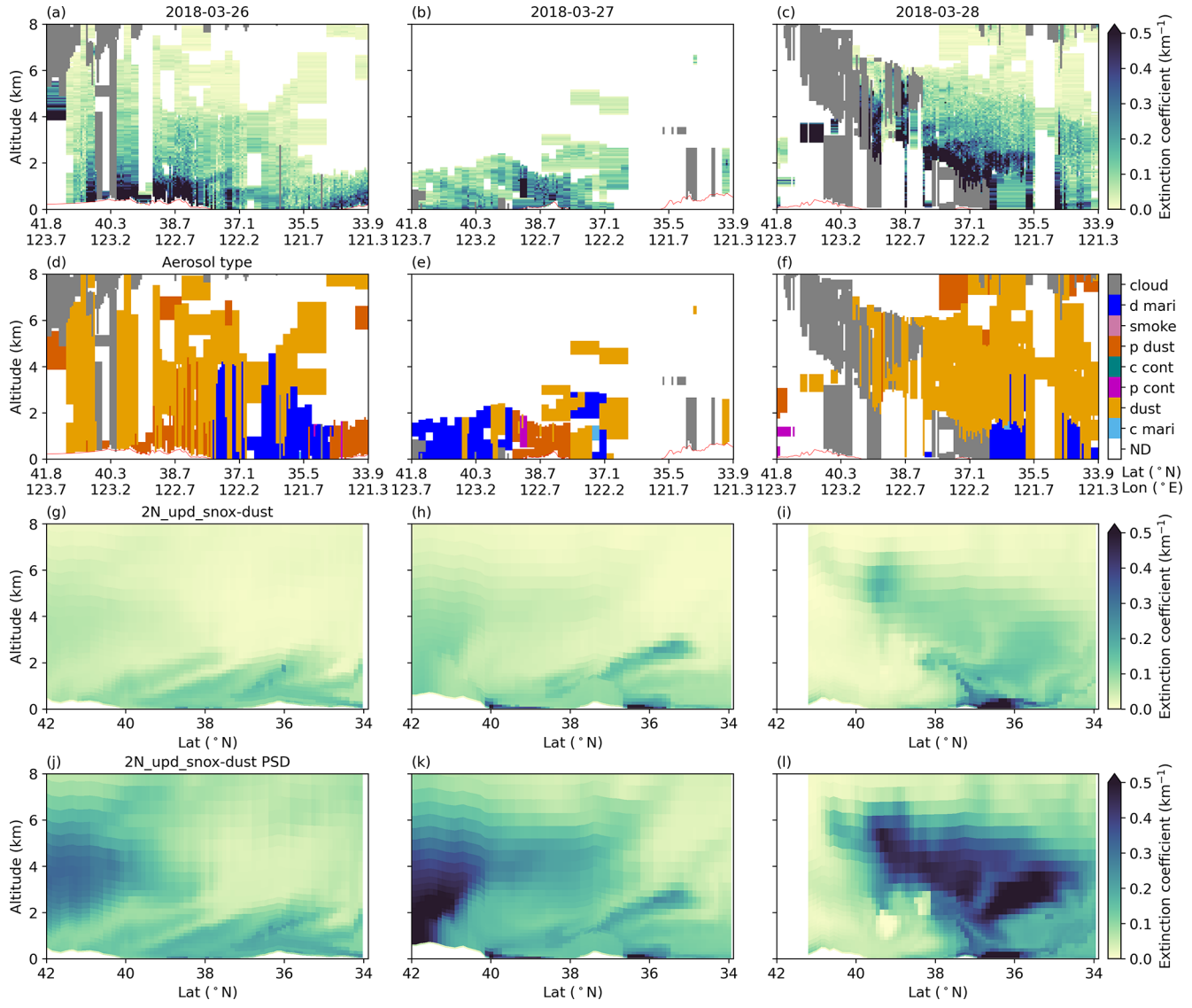

Figure 8. Comparison of CALIOP–derived vertical profile of aerosol extinction coefficient (532 nm, **a–c**) and aerosol type **(d–f)** with UI-WRF-Chem simulated extinction coefficient for CHN-Beijing over 26–28 March 2018. UI-WRF-Chem outputs are from the outer domain (D1) that overlap with CALIOP tracks (Fig. 4). **(g)–(i)** are the extinction coefficients from the UI-WRF-Chem sensitivity simulation 2N_upd_snox-dust, where dust and other aerosols are considered in the MERRA-2 chemical boundary conditions. **(j)–(l)** are the extinction coefficients from UI-WRF-Chem sensitivity simulation 2N_upd_snox-dust PSD where dust concentration is scaled in the MERRA-2 chemical boundary conditions, based on constraining MERRA-2 dust PSD data with AERONET PSD climatology data. In **(a)–(f)**, the gray areas represent cloud. In **(d)–(f)**, different aerosol types are classified: d mari for dusty marine, p dust for polluted dust, c cont for clean continental, p cont for polluted continental and c mari for clean marine. ND includes areas that have clean air and aerosol type not being determined.

ability of MODIS data to ensure a fair comparison. The Beijing-Tianjin-Hebei region is one of the highly urbanized clusters in the world and has experienced intense urban heat island (UHI) effects in the past decade (Wang et al., 2016; Clinton and Gong, 2013). First, by comparing the default and updated land cover type (Fig. 9a and f), we can see that the updated land cover type captures the urban growth over the region. The corresponding land surface properties including LAI, GVF and albedo also show changes with the updated data (Fig. S4). Both daytime (∼ 10:30 a.m. and ∼ 01:30 p.m. LT) (Figs. 9b and S5a) and nighttime (∼ 10:30 p.m. and ∼ 01:30 a.m. LT) (Figs. 9g and S5e) LST from MODIS Terra and Aqua show the UHI phenomenon over the region. Our UI-WRF-Chem model simulated TSK with updated land surface properties using MODIS data can capture the UHI spatial pattern with higher temperature in urban areas than rural areas for both daytime and nighttime. It matches the spatial pattern of satellite

observed LST UHI better than the UI-WRF-Chem simulation with the use of the default USGS land cover type and other surface properties, which is consistent with our previous work (Wang et al., 2023). Figure 3b shows the Taylor Diagram of comparing UI-WRF-Chem simulated LST with MODIS Terra and Aqua daytime and nighttime, respectively. We find that the UI-WRF-Chem simulated TSK with updated land surface properties decreases the relative bias for both Terra and Aqua daytime and nighttime, compared with the UI-WRF-Chem simulation using the default USGS land surface properties. The model simulated TSK with updated land surface properties also results in an increase in correlation for the Aqua daytime period compared with the model simulation using the USGS land surface properties.

Figure S6 shows the potential impacts of updated land surface properties on model simulated planetary boundary layer height (PBLH) and subsequently on surface $PM_{2.5}$ concentration. We find that the PBLH mainly increases in the urban areas where the land surface temperature increases, which in turn leads to a decrease in surface $PM_{2.5}$. Our work shows the promising use of updated land surface properties with timely satellite data to better capture the land cover type and other land surface properties for regions with fast urban development. To better study the impacts of UHI in the region, an urban canopy model could be used to include more details about the underlying urban surface feature and better simulate the physical processes in the boundary layer (He et al., 2019; Liang et al., 2021) with a finer spatial resolution, which is beyond the scope of the current work.

4.1.4 Impacts of updated soil NO_x emission scheme on model performance

Our previous work (Sha et al., 2021) has shown the improvement of model simulated NO_2 VCD, when evaluated against TROPOMI NO_2 VCD over croplands in California, using the BDISNP soil NO_x emission scheme. Here, we also use TROPOMI NO_2 VCD to evaluate UI-WRF-Chem simulated NO_2 VCD over croplands in the outer domain (D1) of CHN-Beijing for July 2018. Daily TROPOMI NO_2 data are regridded to UI-WRF-Chem grids with averaging kernels being applied. Hourly data from UI-WRF-Chem output, close to the TROPOMI overpass time ($\sim$ 01:30 p.m. LT) are averaged to compare with TROPOMI data. First, Fig. S7 shows the UI-WRF-Chem simulated monthly mean soil NO_x emissions using the default emission scheme – MEGAN (2N_upd_MEGAN in Table 2) and the updated scheme – BDISNP (2N_upd_BDISNP in Table 2), respectively. The MEGAN scheme (Fig. S7a) simulates low soil NO_x emissions over the whole domain and the BDISNP (Fig. S7b) instead simulates higher soil NO_x emissions in non-urban areas. Croplands show the largest soil NO_x emissions due to the use of fertilizer.

We compare the model simulated tropospheric NO_2 VCD with TROPOMI NO_2 VCD for July 2018 (Figs. 10 and 11). We can find that both simulations underestimate TROPOMI NO_2 VCD (2.2×10^{15} molec. cm^{-2}) by 1.4×10^{15} and 1.3×10^{15} molec. cm^{-2} for the MEGAN and BDISNP respectively (Fig. 11a and b) over the whole domain. The model simulated NO_2 VCD increases from 1.4×10^{15} using the MEGAN scheme to 1.7×10^{15} molec. cm^{-2} using the BDISNP scheme over croplands. The BDISNP decreases MAE from 1.59×10^{15} to 1.53×10^{15} molec. cm^{-2} (paired t-test, adjusted $p < 0.05$; Bonferroni correction) over the whole domain mainly due to the improvement over croplands. Over croplands, we can see the enhancement in the model simulated NO_2 VCD (Fig. 10c). MAE for croplands decreases from 1.88×10^{15} molec. cm^{-2} to 1.77×10^{15} (paired t-test, adjusted $p < 0.05$; Bonferroni correction). Both reductions in MAE are statistically significant, underscoring that the improvements are robust, though moderate in magnitude. The increase in soil NO_x emissions has potential impacts on surface nitrate. Figure S8 shows that the increase in surface soil NO_x emissions leads to the increase in surface nitrate up to 30 % in rural areas. Due to the lack of surface observation of nitrate, we are limited to quantify the impacts of the improvement of soil NO_x emissions on surface nitrate. The MAIA satellite mission coupled with the Geostationary Environment Monitoring Spectrometer (GEMS) (Kim et al., 2020) satellite mission could provide a synergetic opportunity to evaluate both gas and aerosol chemistry.

4.2 Case study – ITA-Rome

Our case study over CHN-Beijing target area has demonstrated the benefits of using MERRA-2 data to provide chemical boundary conditions for capturing long-range transport events such as dust intrusion. Some of the other target areas including ITA-Rome are also impacted by dust transport. Saharan dust transport poses a significant concern on air quality in Europe and the Mediterranean Basin. Previous studies have shown that Saharan dust outbreaks are more frequent in southern Europe including Italy than northern Europe (Querol et al., 2009; Viana et al., 2014; Pey et al., 2013; Wang et al., 2020a). For example, Pey et al. (2013) showed that across the Mediterranean Basin, African dust outbreaks occurred from 30 % to 37 % of the annual days in the southern sites and less than 20 % of the days in the northern sites. The work of Barnaba et al. (2022) investigated the impacts of African dust on surface PM_{10} concentrations in Italy using surface monitoring sites in Italy from 2006–2012 and found that African dust affected surface PM_{10} levels in Northern and Southern Italy for about 10 % and 30 % of dates in a year, respectively.

Here, we focus on June 2023, where Saharan dust affected PM concentrations in ITA-Rome, and investigate the benefits of using MERRA-2 data to provide chemical boundary conditions for driving UI-WRF-Chem. For example, one Saharan dust intrusion into Italy occurred from 19–22 June 2023

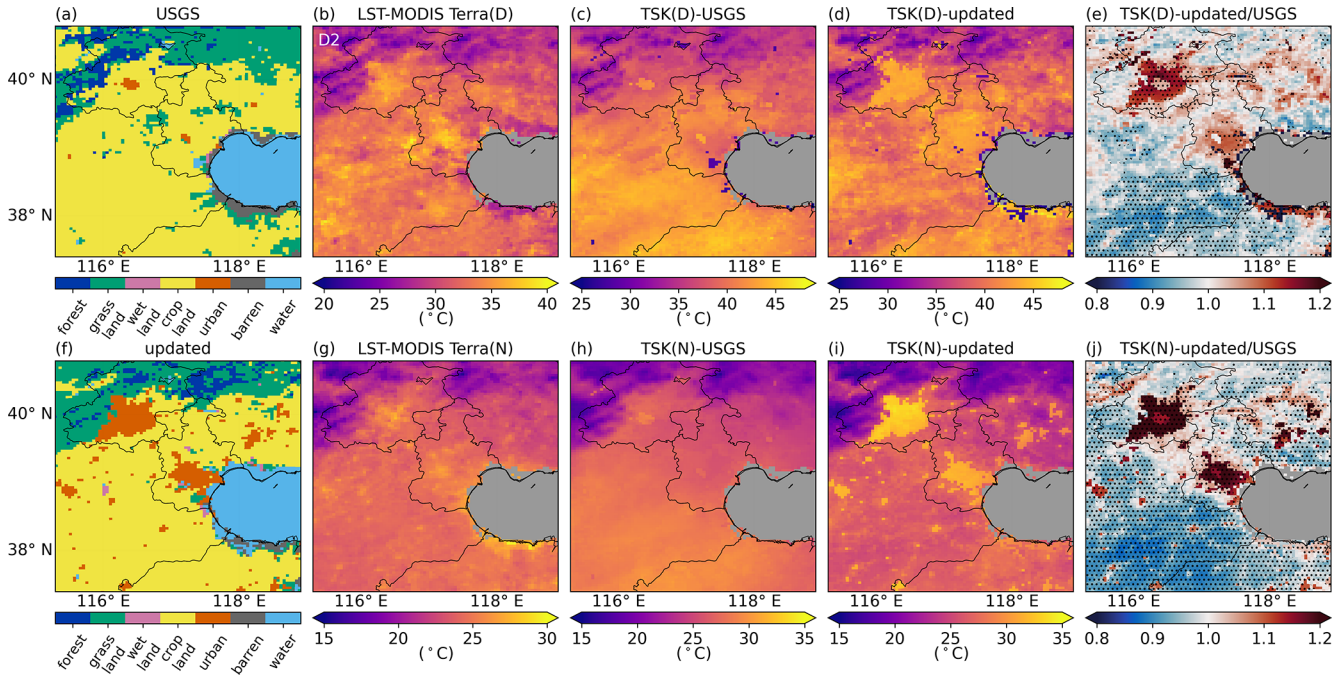

Figure 9. Comparison of UI-WRF-Chem simulated monthly mean surface skin temperature (TSK) with MODIS Terra observed land surface temperature (LST) over the inner domain (D2) of CHN-Beijing for July 2018. **(a)** and **(f)** are the land cover type from the default USGS data and updated MODIS land data. **(b)** and **(g)** are the MODIS Terra LST during daytime (D) and nighttime (N), respectively. **(c)** and **(d)** are model simulated TSK averaged over Terra overpass time during daytime from UI-WRF-Chem sensitivity simulations 2N_def (default USGS land cover type and subsequently derived GVF, LAI and albedo) and 2N_upd (updated land cover type, GVF, LAI and albedo with MODIS land data) in Table 2, respectively. **(e)** is the ratio between **(d)** and **(c)**, expressed as the geometric mean of daily ratio, with stippling indicating model grids where the difference is statistically significant (Wilcoxon test, adjusted $p < 0.05$; FDR correction). **(h)–(j)** are the same as **(c)–(e)** but averaged over Terra overpass time during nighttime. Oceans are masked as gray colors.

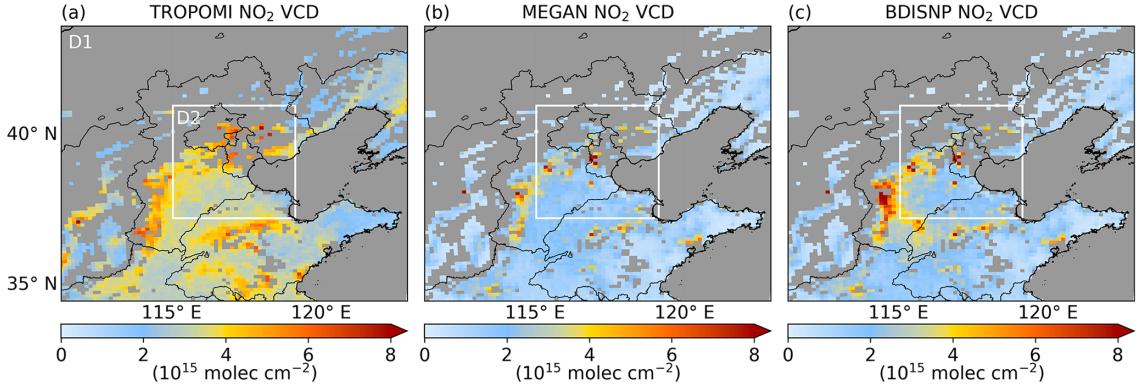

Figure 10. Monthly mean tropospheric NO_2 vertical column density (VCD) over the outer domain (D1) of CHN-Beijing for July 2018 from TROPOMI observation and model sensitivity simulations. Only model grids identified as croplands are shown on the plots and the rest are marked as gray colors. **(a)** TROPOMI observations; **(b)** UI-WRF-Chem sensitivity simulation 2N_upd_MEGAN (Table 2) using the MEGAN scheme to calculate soil NO_x emissions; **(c)** UI-WRF-Chem sensitivity simulation 2N_upd_BDISNP (Table 2) using the BDISNP scheme to calculate soil NO_x emissions. The white box represents the inner domain (D2).

as seen from the VIIRS AOD (Fig. S9) and MERRA-2 simulated dust AOD (not shown here) also captures this dust intrusion event. We conduct three UI-WRF-Chem model sensitivity simulations with different chemical boundary conditions to evaluate model simulated surface PM concentrations and AOD: (1) simulation "2N-none": no chemical species from MERRA-2 data are transported into the domain; (2) simulation "2N-dust": dust and other aerosols including sulfate, BC and OC are considered in the MERRA-2 chemical boundary condition; (3) simulation "2N-dust PSD": dust concen-

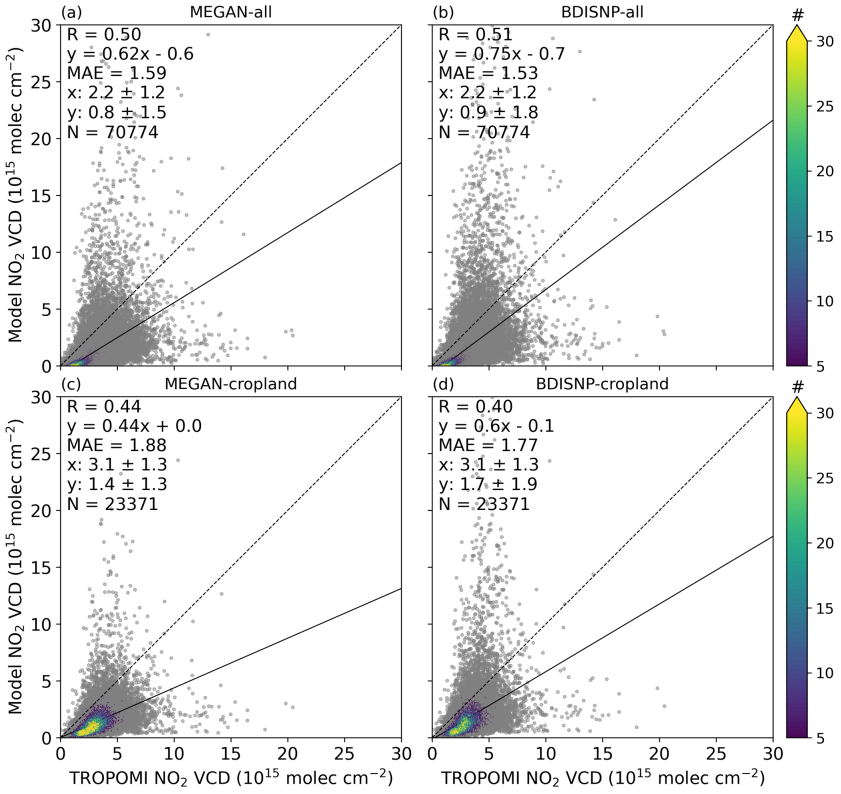

Figure 11. Scatter plot of daily tropospheric NO_2 VCD between model (y axis) and TROPOMI observation (x axis) over the outer domain (D1) of CHN-Beijing for July 2018. **(a)** and **(c)** refer to the UI-WRF-Chem sensitivity simulation using the MEGAN scheme (2N_upd_MEGAN in Table 2) and **(b)** and (d) refer to the sensitivity simulation using the BDISNP scheme (2N_upd_BDISNP in Table 2) to calculate soil NO_x emissions, respectively. **(a)** and **(b)** are for model grids over the whole domain while **(c)** and **(d)** are for model grids that are identified as croplands. Also shown on the scatter plot is the correlation coefficient (R), the mean absolute error (MAE), the mean ± standard deviation for observed (x) and model simulated tropospheric NO_2 VCD (y), the number of collocated data points (N), the density of points (the color bar), the best fit linear regression line (the solid black line) and the 1 : 1 line (the dashed black line).

tration of different size bins in the MERRA-2 boundary conditions is constrained using the AERONET PSD climatology data from 2000–2023. AERONET sites close to the Saharan dust source region are used for constraining MERRA-2 PSD (Fig. 2b). Figure 5b shows the averaged PSD over the AERONET sites between 2000–2023 from both MERRA-2 and AERONET data. The ratio between the mean of the AERONET PSD and MERRA-2 PSD for each of the five dust size bins is then used as a constraint to scale the dust concentration in each bin in the MERRA-2 chemical boundary data in the simulation "2N-dust PSD".

Like the case study in CHN-Beijing, using MERRA-2 data to provide chemical boundary conditions for UI-WRF-Chem over ITA-Rome also improves both model simulated surface PM concentration and AOD (Fig. 12). WRF-Chem PM data are regridded onto the MERRA-2 grid for a fair comparison. Compared with the sensitivity simulation 2N-none, the correlation (R) from the sensitivity simulation 2N-dust increases from 0.12 to 0.54, 0.38 to 0.70, and 0.15 to 0.62 for surface $PM_{2.5}$, surface PM_{10} and AOD, respectively, for the whole month of June. The MB decreases from −6.8 to −2.1, −13.8 to $-2.3\,\mu g\,m^{-3}$, and −0.23 to −0.13 for surface $PM_{2.5}$, PM_{10} and AOD respectively. The MAE decreases significantly from 6.9 to $3.8\,\mu g\,m^{-3}$, 13.7 to $9.1\,\mu g\,m^{-3}$, and 0.23 to 0.13 (paired t-test, adjusted $p < 0.05$; Bonferroni correction) for surface $PM_{2.5}$, PM_{10} and AOD respectively. Using constrained dust concentration in the MERRA-2 data (2N-dust PSD) further reduces the MB for surface $PM_{2.5}$ and AOD and slightly overestimates surface PM_{10}, compared with simulation 2N-dust. In contrast, both MERRA-2 simulated surface $PM_{2.5}$ and PM_{10} overestimate surface observations with MB of 6.4 and $21.8\,\mu g\,m^{-3}$, respectively. Both simulations (2N-dust and 2N-dust PSD) show higher correlation than MERRA-2 (0.70 vs. 0.66) when evaluating surface PM_{10} concentration against ground observations, while simulation 2N-dust PSD shows slightly lower correlation than MERRA-2 for surface $PM_{2.5}$ (0.52 vs. 0.54). MAEs from both simulations are also improved significantly (paired t-test, adjusted $p < 0.05$; Bonferroni correction), compared to those of MERRA-2 for both surface $PM_{2.5}$ (3.8 vs. $6.7\,\mu g\,m^{-3}$; 4.1 vs. $6.7\,\mu g\,m^{-3}$) and PM_{10} (9.1 vs. $22.0\,\mu g\,m^{-3}$; 10.3 vs. $22.0\,\mu g\,m^{-3}$). Compared with simulation 2N-dust, simula-

tion 2N-dust PSD improves model simulated AOD with MB decreasing from 0.13 to 0.09 and MAE decreases from 0.13 to 0.11 (paired t-test, adjusted $p < 0.05$; Bonferroni correction). MERRA-2 data has the best AOD performance as expected since it assimilates satellite AOD.

During June 2023, some parts of the ITA-Rome domain experienced precipitation events (Fig. S10), which occurred mostly during the first half of the month. Compared to the Global Precipitation Measurement (GPM) mission observed precipitation and MERRA-2 simulated precipitation (Fig S10), UI-WRF-Chem simulates higher precipitation, which could result in higher wet deposition of aerosols and lower concentration. Figure S11 shows the comparison of model simulated surface daily $PM_{2.5}$ and PM_{10} with ground observations for the first and second half of the month in June 2023, respectively. We can see that UI-WRF-Chem simulation 2N-dust underestimates both surface $PM_{2.5}$ and PM_{10} during the first half of the month (Fig. S11a–h) with MB of -3.1 and $-5.7\,\mu g\,m^{-3}$, respectively, while MERRA-2 overestimates surface $PM_{2.5}$ and PM_{10} with MB of 5.1 and $15.7\,\mu g\,m^{-3}$, respectively. During the second half of the month (Fig. S11i–p), UI-WRF-Chem simulation 2N-dust underestimates surface $PM_{2.5}$ with MB of $-1.3\,\mu g\,m^{-3}$ but slightly overestimates surface PM_{10} with MB of $1.3\,\mu g\,m^{-3}$. MERRA-2 still overestimates surface $PM_{2.5}$ and PM_{10} with MB of 7.4 and $28.4\,\mu g\,m^{-3}$, respectively. Due to the coarse spatial resolution of MERRA-2 data, it may not resolve the localized convective processes well, which could affect the subsequent wet deposition. There are also uncertainties associated with the dust size distribution in MERRA-2 data, which could also affect the wet deposition.

Additionally, uncertainty in UI-WRF-Chem model simulated wet deposition of aerosols could play a role in the model results discussed above. Previous studies have mostly focused on dry dust events (e.g., Zeng et al., 2020), and less has focused on wet dust events, especially dust wet deposition. Jung and Shao (2006) implemented a below-cloud dust wet deposition scheme for the UOC dust emission scheme in WRF-Chem. Currently, no dust wet scavenging scheme is implemented for the original GOCART or GOCART AFWA dust scheme in WRF-Chem. As in previous work (Su and Fung, 2015), we have implemented a simple scheme to allow dust wet scavenging by large scale and convective precipitation by assigning a scavenging efficiency for different dust size bins in the model. Future work will focus on implementing a more complex dust wet deposition scheme to better account for the scavenging processes that consider the dust particle size distribution etc., such as the work of Tsarpalis et al. (2018) and Zhao et al. (2003). Nevertheless, the case study over ITA-Rome again demonstrates the benefits of using MERRA-2 data to drive UI-WRF-Chem for capturing dust transport events.

4.3 Case study – USA-LosAngeles

Each target area has its unique feature of aerosol composition and various factors that affect the aerosol concentration, we have demonstrated the impacts of dust transport on surface PM concentration and AOD over CHN-Beijing and ITA-Rome target areas. Here, we focus on some fine tuning over USA-LosAngeles target area to improve the model simulation of surface PM concentration and AOD.

For the USA-LosAngeles target area (Fig. 2c), we investigate the impacts of dust emissions on surface PM concentration and AOD. Part of the outer domain (D1) over the USA-LosAngeles target area (here defined as the dust-prone region, the orange box in Fig. S12), located in the southwestern U.S., are desert regions with higher soil erodibility than other parts of the domain. It is common in WRF-Chem to tune some of the parameters in the dust emission scheme including the soil erodibility to better match model simulated PM_{10} concentration and AOD with satellite- and ground-based observations (e.g., Su and Fung, 2015). This approach has been mainly focusing on the total atmospheric dust load instead of an individual dust event and it is sufficient to capture the general magnitude of dust aerosol patterns. We have adopted this simple approach here to do some dust parameter tuning to improve model simulated surface PM_{10} concentration and AOD with a focus on the overall magnitude.

There are several parameters that can be used to tune dust emissions in the WRF-Chem model. One is the dust_gamma (gamma for short here), which tunes the soil erodibility in an exponential manner. Soil erodibility serves as an important factor for identifying dust source and estimating dust emission flux in the model. The other one is the dust_alpha (alpha for short here), which linearly tunes the total dust emissions. If we use the default setting (gamma = 1, alpha = 1), both model simulated surface daily PM_{10} concentration and hourly AOD overestimate surface measurements of PM_{10} and AOD in the dust-prone region (Figs. 13a and j, S13 and S14). Model simulated surface $PM_{2.5}$ concentration also overestimates surface measurements of $PM_{2.5}$ (Fig. S13a). We conduct two groups of sensitivity simulations to test the responses of model simulated PM_{10} and AOD to a range of gamma and alpha values, respectively. For the first group test, we set the gamma with 1.5, 2, 2.5 and 3 respectively, while keeping the alpha value as 1. For the second group test, we set the alpha with 0.2, 0.3, 0.4, and 0.5 respectively, while keeping the gamma value as 1. As gamma increases from 1 to 3 with the constant alpha value of 1, correlation increases for AOD and decreases for surface PM_{10} (Fig. 13). RMSE also decreases with increasing gamma value until when gamma value reaches 2.5 for both AOD and PM_{10}. MAE also decreases significantly for both AOD (0.08 to 0.04) and PM_{10} (46.7 to $21.5\,\mu g\,m^{-3}$) (paired t-test, adjusted $p < 0.05$; Bonferroni correction) when gamma increases from 1 to 2.5. As alpha value decreases from 1 to 0.5 with the constant gamma of 1, both MB and RMSE for surface PM_{10} and AOD de-

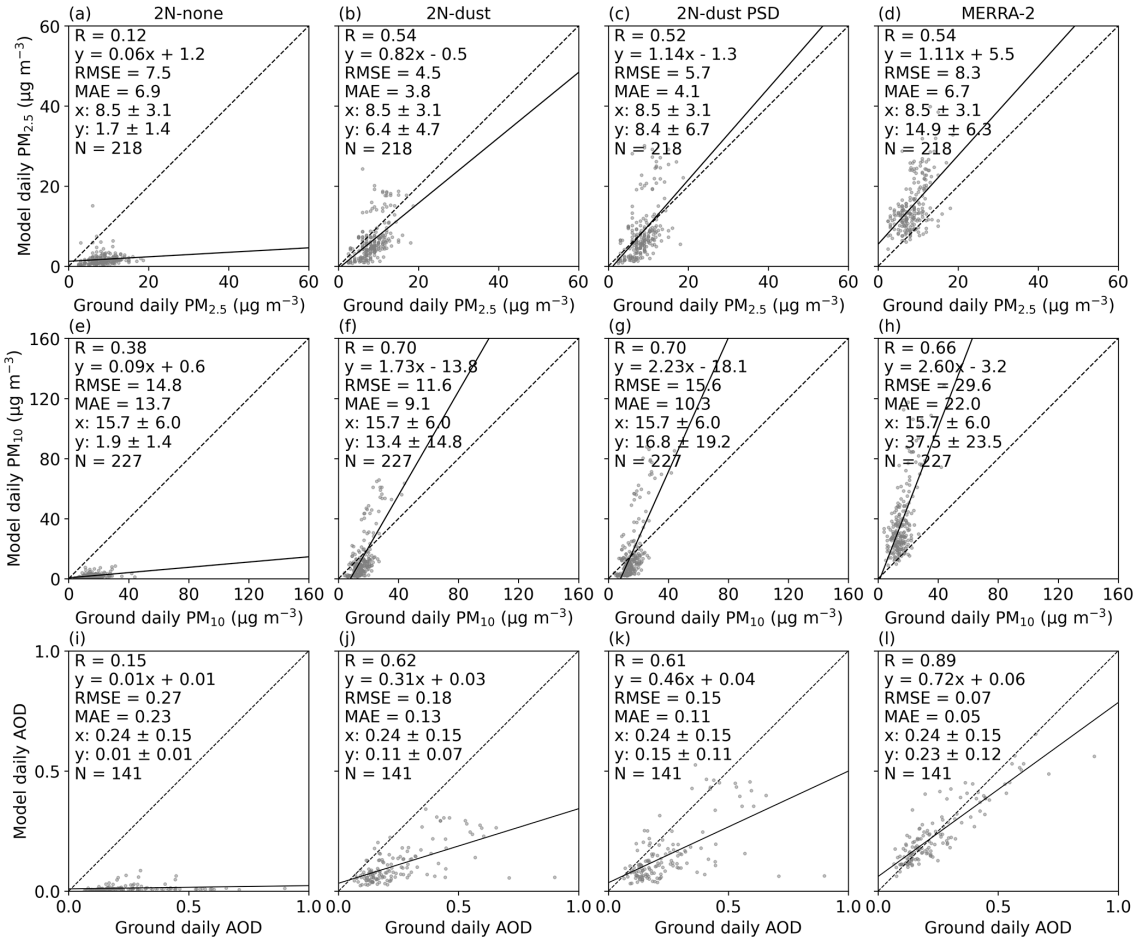

Figure 12. Scatter plot of daily $PM_{2.5}$ concentration **(a–d)**, PM_{10} concentration **(e–h)**, and AOD **(i–l)**, between model (y axis) and ground observation (x axis) over the inner domain (D2) of ITA-Rome for June 2023. **(a)**–**(c)**, **(e)**–**(g)**, and **(i)**–**(k)** refer to the UI-WRF-Chem sensitivity simulations with different chemical boundary conditions being considered using MERRA-2 data. 2N-none: no chemical species; 2N-dust: dust and other aerosols; 2N-dust PSD: same as 2N-dust except that the dust concentration is scaled based on constraining MERRA-2 dust PSD data with AERONET PSD climatology data. **(d)**, **(h)** and **(l)** show the MERRA-2 simulated daily $PM_{2.5}$, PM_{10} and AOD, respectively. Also shown on the scatter plot is the correlation coefficient (R), the root-mean-square error (RMSE), the mean absolute error (MAE), the mean ± standard deviation for observed (x) and model-simulated $PM_{2.5}$/PM_{10}/AOD (y), the number of collocated data points (N), the best fit linear regression line (the solid black line) and the 1 : 1 line (the dashed black line). WRF-Chem PM data are regridded onto the MERRA-2 grid, and when multiple surface PM sites fall within the same MERRA-2 grid, the observations are then averaged to represent a single collocated site.

crease until alpha value drops to 0.3. The correlation almost stays the same or slightly increases for both PM_{10} and AOD with decreasing alpha value. MAE also decreases significantly for both AOD (0.08 to 0.04) and PM_{10} (46.7 to 17.9 $\mu g\,m^{-3}$) (paired t-test, adjusted $p < 0.05$; Bonferroni correction) when alpha decreases from 1 to 0.3. Furthermore, the sensitivity simulation (gamma = 1, alpha = 0.3) outperforms the sensitivity simulation (gamma = 2.5, alpha = 1) with enhanced correlation (0.48 vs. 0.37) and statistically significant decrease in MAE (17.9 vs. 21.5, paired t-test, adjusted $p < 0.05$; Bonferroni correction). Therefore, we choose gamma of 1 and alpha of 0.3 as the final configuration to account for the model performance of both PM_{10} and AOD.

Here, we use one month of data to tune the dust emissions by focusing on the magnitude of the total dust load. It is challenging to fine tune each individual dust event and acquire consistent results. The work of Hyde et al. (2018) simulated nine dust storms in south-central Arizona with WRF-Chem using the GOCART AFWA dust emission scheme and the model unevenly reproduced the dust-storm events with some cases overestimating surface PM_{10} and some cases underestimating surface PM_{10}. Our evaluation of AOD with AERONET observation is rather limited spatially as we only have one AERONET site available over the dust-prone re-

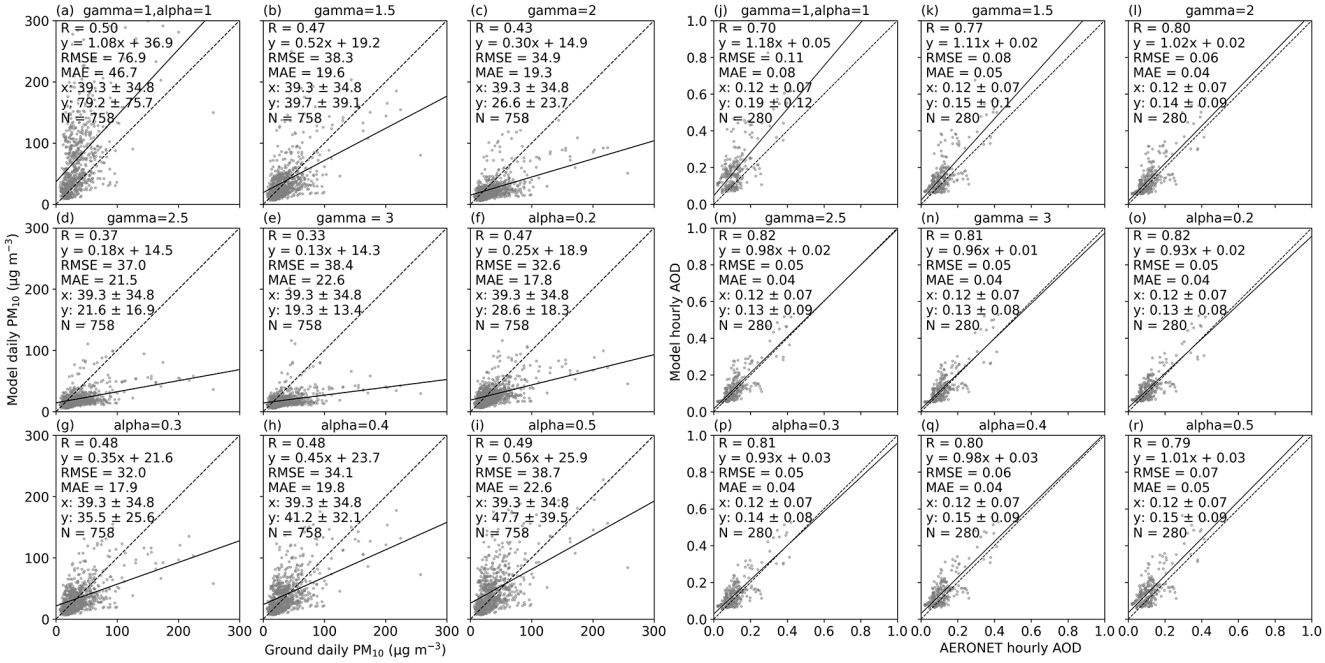

Figure 13. Scatter plot of daily surface PM_{10} concentration and hourly AOD between model (y axis) and ground observation (x axis) over the dust-prone region of USA-LosAngeles for July 2018. **(a)–(i)** are for surface daily PM_{10} and **(j)–(r)** are for hourly AOD from two groups of sensitivity simulations: **(1)** gamma = 1, 1.5, 2, 2.5, 3 while alpha stays as 1; (2) alpha = 0.2, 0.3, 0.4, 0.5 while gamma stays as 1, respectively. Also shown on the scatter plot is the correlation coefficient (R), the root-mean-square error (RMSE), the mean absolute error (MAE), the mean ± standard deviation for observed (x) and model-simulated surface PM_{10}/AOD (y), the number of collocated data points (N), the best fit linear regression line (the solid black line) and the 1 : 1 line (the dashed black line).

gion. We also conduct the same set of sensitivity simulations for July 2019 (results not shown here) and the sensitivities to the tuned parameters are comparable to results shown here in general, which further confirms the validity of the simple approach we have used. Additionally, more recent work has incorporated the albedo-based drag partition (Chappell and Webb, 2016) from satellite data into the GOCART AFWA dust emission scheme to better represent the impacts of roughness features from vegetation and non-vegetation such as soil and rocks, which demonstrated improved model performance in capturing individual dust event over the Southwestern U.S. (LeGrand et al., 2023; Dhital et al., 2024). It is beyond the scope of this work to implement this method, but future work could explore the use of this advanced method and focus on longer periods of model simulation to further evaluate model performances.

4.4 Case study – USA-Atlanta

As described in Sect. 3, for the standard PTA nested domain setup, we have chosen to turn off the cumulus parameterization in the inner domain (D2) with the spatial resolution of 4 km and allow the microphysics scheme to explicitly resolve the convection. Here, we use PTA-Atlanta as an example to examine the impacts of different setups of microphysics and cumulus schemes on model simulated precipitation and surface total and speciated $PM_{2.5}$. Since the MAIA satellite mission focuses on speciated PM, we also use PTA-Atlanta here to demonstrate how UI-WRF-Chem simulates speciated $PM_{2.5}$ mass concentrations in addition to total $PM_{2.5}$.

4.4.1 Impacts of microphysics and cumulus schemes on precipitation and surface total $PM_{2.5}$

Southeastern U.S. including the PTA-Atlanta (Fig. 2d) target area experiences pulse-type summer convective precipitation due to the interplay of land-sea breezes, outflow boundaries and complex terrain etc. (Case et al., 2011). Here, we focus on June 2022 over PTA-Atlanta to demonstrate the impacts of different setups of microphysics and cumulus schemes on model simulated precipitation and subsequent surface total $PM_{2.5}$ concentration. We perform six UI-WRF-Chem sensitivity simulations with different setups of microphysics and cumulus schemes while keeping other schemes the same as shown in Table 3: (1) mp2cu5: both domain 1 and domain 2 have the Lin microphysics scheme on. Domain 1 and domain 2 have the G3D cumulus scheme on and off, respectively; (2) mp2cu5bothon: same as (1) except that both domain and 1 and domain 2 have the G3D cumulus scheme on; (3) mp2cu3bothon: same as (2) except that both domain 1 and domain 2 have the GF cumulus scheme on; (4) mp10cu5; (5) mp10cu5bothon; and (6) mp10cu3bothon. (4)–(6) are the

same as (1)–(3) except that both domain 1 and domain 2 have the Morrison microphysics scheme on. Here, the difference between (1) and (2) illustrates the impacts of turning on/off the cumulus scheme at the 4 km resolution. The difference between (1), (2) and (1), (3) evaluates the impacts of using a traditional cumulus scheme vs. a scale-aware cumulus scheme. Corresponding difference between (1), (3) and (4), (6) represents the impacts of the microphysics scheme.

We first focus on the evaluation of daily precipitation. Although, hourly precipitation rate can be important to tell the intensity of the precipitation event, verification of the hourly precipitation can raise double-penalty issues at the finer resolution (Rossa et al., 2008; Gilleland et al., 2009), where a slight shift in the prediction of the timing or location of the precipitation event compared with the ground truth could result in the verification penalties in both space-time. Here, we accumulate the hourly precipitation into daily precipitation to help offset the errors associated with the timing of the event. Figure S15 shows the monthly averaged daily precipitation from UI-WRF-Chem model sensitivity simulations (1)–(6) with surface observations. In general, all the sensitivity runs overestimate the precipitation. Turning on the cumulus scheme in domain 2 when using the traditional G3D scheme results in larger bias compared to the results of turning the G3D scheme off. The work of Zhang et al. (2021) also found that the WRF model had better prediction of precipitation in the central Great Plains in the U.S. when turning off the G3D cumulus scheme with the spatial resolution of 4 km, compared to the sensitivity run of turning on the G3D cumulus scheme. Turning off the cumulus scheme in domain 2 when using the G3D scheme is comparable to the results of the simulation using the scale-aware GF cumulus scheme.

We then investigate the impacts on surface total $PM_{2.5}$ concentration. Figure S16 shows the spatial map of surface total $PM_{2.5}$ concentration for June 2022 and Fig. 14 compares model simulated daily total $PM_{2.5}$ concentration with ground observation. Both sensitivity simulations (2) and (4) with the G3D scheme on for the inner domain (D2) simulate higher precipitation than other simulations, which leads to lower surface $PM_{2.5}$ concentrations (Fig. S16b and e). Overall, the surface $PM_{2.5}$ concentrations from sensitivity simulations (2) and (4) have the lowest correlation (0.34 and 0.49) compared to other simulations (0.52–0.61) (Fig 14). They also have higher MB (-5.1 and $-5.9\,\mu g\,m^{-3}$) compared with other simulations (-4.7 to $-3.2\,\mu g\,m^{-3}$) (Fig. 14). Sensitivity simulations over CHN-Beijing also show similar results related to surface $PM_{2.5}$ concentration when contrasting the sensitivity simulation with or without the G3D cumulus on for the inner domain (not shown here). This validates our choice of turning the cumulus scheme off for the inner domain (D2) when using the traditional cumulus scheme such as G3D. When only using the Lin microphysics scheme (mp2), the MAE from simulation (1) mp2cu5 improves on both simulation (2) mp2cu5bothon and simulation (3) mp2cu3bothon (3.7 vs. 5.7; 3.7 vs. 5.1 $\mu g\,m^{-3}$) (paired t-test, adjusted $p < 0.05$; Bonferroni correction). When only considering using the Morrison microphysics scheme (mp10), simulation (4) mp10cu5 shows statistically lower MAE than that of simulation (5) mp10cu5bothon (5.0 vs. 6.2 $\mu g\,m^{-3}$), while simulation (6) mp10cu3bothon shows statistically reduced MAE than simulation (4) (4.8 vs. 5.0 $\mu g\,m^{-3}$) (paired t-test, adjusted $p < 0.05$; Bonferroni correction). Furthermore, simulation (1) outperforms simulation (6) with reduced RMSE (4.6 vs. 5.6 $\mu g\,m^{-3}$) and statistically significant lower MAE (3.7 vs. 4.8 $\mu g\,m^{-3}$) (paired t-test, adjusted $p < 0.05$; Bonferroni correction). Therefore, we have selected simulation (1) as the final configuration for PTA-Atlanta. It also indicates that surface $PM_{2.5}$ concentrations from sensitivity simulations, which turn off the G3D cumulus scheme (1 and 4) are comparable to or even better than the results from the sensitivity simulations (3) and (6), which turn on the scale-aware cumulus scheme GF, although further tests using the GF are needed.

There are some uncertainties in this case study. First, our evaluation is limited in time. A longer dataset would be more helpful to reveal model performances in other seasons too (Jeworrek et al., 2021). Also, we have only considered a limited number of model configurations. Previous studies have shown that the prediction of precipitation is also sensitive to other schemes in the model such as the PBL scheme (Klein et al., 2015; Argüeso et al., 2011). Most previous work have focused on the impacts of microphysics and cumulus schemes on precipitation and less have focused on the coupling with the aerosol fields. The process of handling aerosol-cloud interactions would be another source of uncertainty here. Lastly, deficiencies in MERRA-2 meteorology boundary conditions could also introduce uncertainties or biases in the WRF-Chem simulation (Zhang et al., 2021).

4.4.2 Evaluation of model simulated speciated $PM_{2.5}$

Surface measurements of total and speciated $PM_{2.5}$ mass concentration from the Interagency Monitoring of Protected Visual Environments (IMPROVE) (Malm et al., 1994; Solomon et al., 2014) and the Chemical Speciation Network (CSN) (Solomon et al., 2014) networks (see Fig. S17 for sites location information) are used to evaluate model performance. We compare UI-WRF-Chem simulated speciated $PM_{2.5}$ (OC, EC, Sulfate + Nitrate, Dust) and total $PM_{2.5}$ against these observations. Figure S18 shows the comparison of daily speciated $PM_{2.5}$ between the model and ground observations for the six different sensitivity simulations (Table 3), while Fig. S17 shows the spatial distribution of total and speciated $PM_{2.5}$ for the "mp2cu5" sensitivity simulation only.

During this month of June, both surface observations and model simulations indicate that OC, sulfate and dust are the dominate components of total $PM_{2.5}$, consistent with previous studies, which show that OC and sulfate are the primary contributors to total $PM_{2.5}$ in the Southeastern U.S. (Hand et

Table 3. A suite of UI-WRF-Chem sensitivity simulations performed over PTA-Atlanta with different setups of microphysics and cumulus schemes for the outer domain (D1) and inner domain (D2), respectively.

	mp2cu5	mp2cu5bothon	mp2cu3bothon	mp10cu5	mp10cu5bothon	mp10cu3bothon
Microphysics-D1	Lin	Lin	Lin	Morrison	Morrison	Morrison
Microphysics-D2	Lin	Lin	Lin	Morrison	Morrison	Morrison
Cumulus-D1	G3D	G3D	GF	G3D	G3D	GF
Cumulus-D2	off	G3D	GF	off	G3D	GF

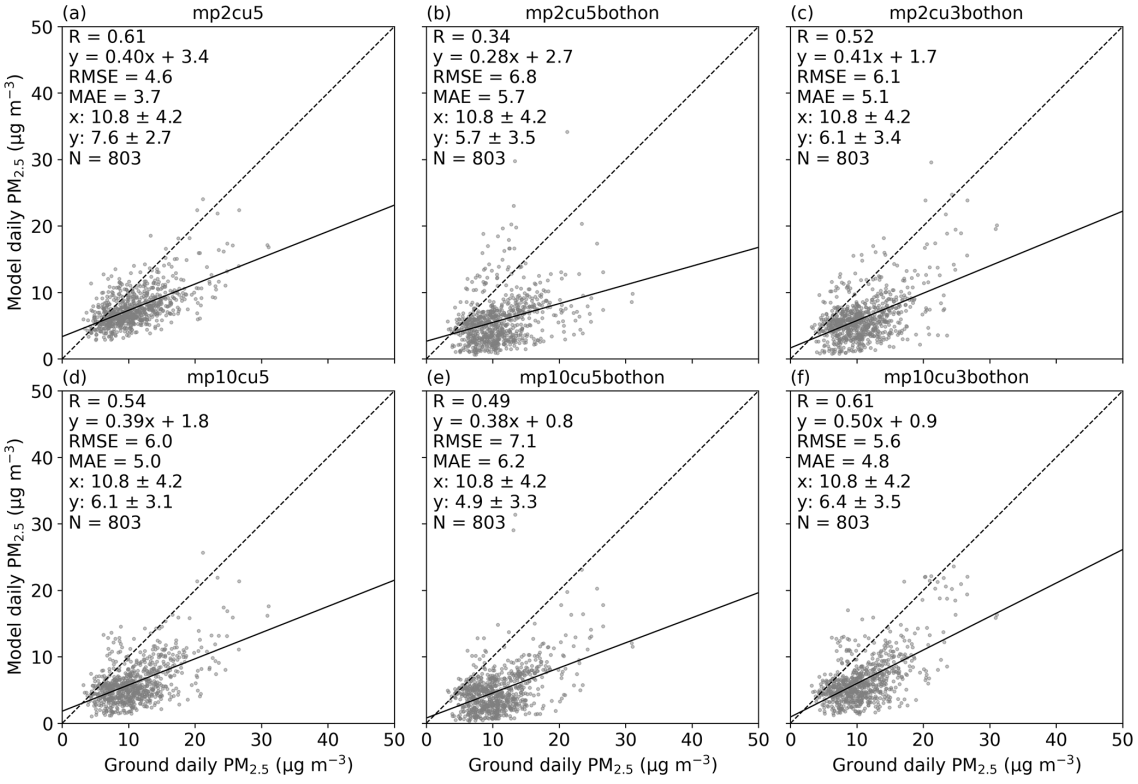

Figure 14. Scatter plot of daily surface $PM_{2.5}$ concentration between model (y axis) and ground observation (x axis) over the inner domain (D2) of USA-Atlanta for June 2022. **(a)–(f)** are the UI-WRF-Chem sensitivity simulations with different setups of microphysics and cumulus schemes. **(a)–(c)** all have the Lin microphysics scheme on for domain 1. **(a)** has the Lin microphysics scheme on for domain 2 and no cumulus scheme is used for domain 2. **(b)** is the same as **(a)** except that the G3D cumulus scheme is turned on for domain 2. **(c)** is same as **(b)** except that the GF cumulus scheme is used for domain 2. **(d)–(f)** are the same as **(a)–(c)** except that the Morrison microphysics scheme is used for both domain 1 and domain 2. Also shown on the scatter plot is the correlation coefficient (R), the root-mean-square error (RMSE), the mean absolute error (MAE), the mean ± standard deviation for observed (x) and model-simulated surface $PM_{2.5}$ (y), the number of collocated data points (N), the best fit linear regression line (the solid black line) and the 1 : 1 line (the dashed black line).

al., 2024; Zhu et al., 2024). Prescribed burns in the Southeastern U.S. including the states of Alabama and Georgia are a major source of OC emissions in this region (Li et al., 2023; Cummins et al., 2023), some of which are represented by the FLAMBE emission inventory in this work. All the model sensitivity simulations for OC show good correlation (0.45–0.60, Fig. S18) but underestimate ground observations with MB from -1.78 to $-1.36\,\mu g\,m^{-3}$. Model simulated EC concentrations also show good correlation (0.45–0.72, Fig. S18) but underestimate ground observations with MB from -0.28 to $-0.21\,\mu g\,m^{-3}$. For the dust component, correlation ranges from 0.42–0.72 (Fig. S18) but all the model sensitivity simulations overestimate ground observations with MB from 0.35–1.53 $\mu g\,m^{-3}$. In contrast, the combined sulfate + nitrate for all the sensitivity simulations show relatively lower correlation (-0.03 to 0.23) and underestimate ground observations with MB from -0.71 to $-0.35\,\mu g\,m^{-3}$. The nitrate concentration from ground observations is low in this region with an average value of $0.198\,\mu g\,m^{-3}$ for this month, which makes it challenging for the model to reproduce such a low

level. Also due to limited samples used for comparison here, sulfate and nitrate are combined for evaluation. Overall, the "mp2cu5" sensitivity simulation (Table 3) yields the best performance.

Figure 15 shows the variability in total and speciated $PM_{2.5}$ mass concentration from model simulation mp2cu5 (Table 3) compared with surface observations as well as the ratio of model simulation to observation. The simulated-to-observed ratio for dust (1–5.8) exhibits much larger variability than other $PM_{2.5}$ components (0–2), with model simulation consistently overestimating dust. During this month, PTA-Atlanta may have been affected by long-range transport of Sahara dust in the model simulation. These biases are likely due to uncertainties in the MERRA-2 simulated dust particle size distribution, as also demonstrated by the case studies over CHN-Beijing and ITA-Rome, motivating future work to tune the dust particle size distribution of MERRA-2 data for this region. Ratios for other components mostly remain below 2. Both sulfate and nitrate aerosols are predominantly secondary aerosols in the atmosphere, formed through chemical reactions and are also highly water-soluble, making them sensitive to uncertainties in the aerosol chemistry and wet deposition schemes. As discussed earlier, this month experiences some convective precipitation events, which likely contributes to the uncertainty and large variability in the simulated speciated $PM_{2.5}$ concentration.

Although our analysis here is limited to one month and one PTA, it provides a valuable case study of how the UI-WRF-Chem modeling framework simulates speciated $PM_{2.5}$. Moreover, previous work by Jin et al. (2024) using the same UI-WRF-Chem framework demonstrated its broader robustness over the Boston PTA. It illustrated the feasibility of the MAIA modeling framework for generating L2 and L4 PM products with a full year (2018) of UI-WRF-Chem outputs of total and speciated $PM_{2.5}$ mass concentrations and showed the correlation of evaluating model total and speciated $PM_{2.5}$ mass concentrations against ground observations ranging from 0.40 to 0.73 (Table S1 therein). Together, these results suggest that while the single-month evaluation such as the case study here only provides a partial picture of model performance, the framework has been shown to produce reliable and robust results for longer time periods. Future work will therefore focus on a more comprehensive assessment of model performance with respect to the PM composition using longer datasets across different PTAs.

5 Conclusions and discussion

We have developed the Unified Inputs (of initial and boundary conditions) for WRF-Chem (UI-WRF-Chem) modeling framework as the CTM, to support the MAIA satellite mission, which aims to study how different types of PM air pollution affect human health. The UI-WRF-Chem outputs including meteorology variables as well as total and speciated PM concentrations will be integrated together with satellite and ground-based observations data to generate surface total and speciated PM maps. Building upon the standard WRF-Chem model, we have developed new modules and included major enhancements in the UI-WRF-Chem framework to improve model simulated meteorology variables, PM concentration and AOD. These major developments include: (1) using NASA GEOS data including GEOS FP and MERRA-2 data to provide both meteorological and chemical initial and boundary conditions to drive WRF-Chem simulations at a finer spatial resolution for both forecasting and reanalysis modes; (2) using a global or regional land data assimilation system (GLDAS or NLDAS) to constrain soil properties (e.g., soil moisture); (3) updating land surface properties (land cover type, LAI, GVF and albedo) with recent available MODIS land data products; (4) developing a new soil NO_x emission scheme – BDISNP; (5) developing the WEPS stand-alone module to process both global and regional anthropogenic emissions as well as fire emissions.

In this work, we focus on four target areas to demonstrate the application of the UI-WRF-Chem modeling framework: CHN-Beijing, ITA-Rome, USA-LosAngeles, and USA-Atlanta. Each target area is set up with 2 nested domains with a 12 and 4 km spatial resolution for the outer domain (D1) and inner domain (D2), respectively. First, we conduct a suite of sensitivity simulations over each target area to select the optimal combination of physics schemes used in the model. We have chosen to turn off the cumulus scheme for the inner domain (D2), since we are using the traditional G3D cumulus scheme, which is not a scale-aware scheme. We investigate the impacts of cumulus and microphysics schemes on model performance over the USA-Atlanta target area for June 2022. Our case study shows that turning on the G3D cumulus scheme in the inner domain (D2) produces higher precipitation than the sensitivity simulation with the G3D scheme off, which in turn leads to lower surface total and speciated $PM_{2.5}$ concentrations. Compared with surface observations of precipitation and $PM_{2.5}$ concentration, the sensitivity simulation with the G3D scheme off shows better performance than keeping it on. Due to the problem with the scale-aware GF cumulus scheme in the model (not coupled to the chemistry), we are not able to fully investigate the impact of a scale-aware scheme on model performance in the current work. Future work will explore the use of this scale-aware scheme with longer periods of simulation or across different target areas.

Both CHN-Beijing and ITA-Rome target areas are affected by dust long-range transport events. We select two dust intrusion events that impacted these two target areas. A dust storm originated from the Taklamakan and Gobi Deserts around 24 March 2018 and moved downwind to CHN-Beijing from 27 to 28 March 2018. For ITA-Rome, we focus on June 2023, where Saharan dust transported to the target area. For both target areas, we conduct UI-WRF-Chem sensitivity simulations with different chemical boundary conditions from

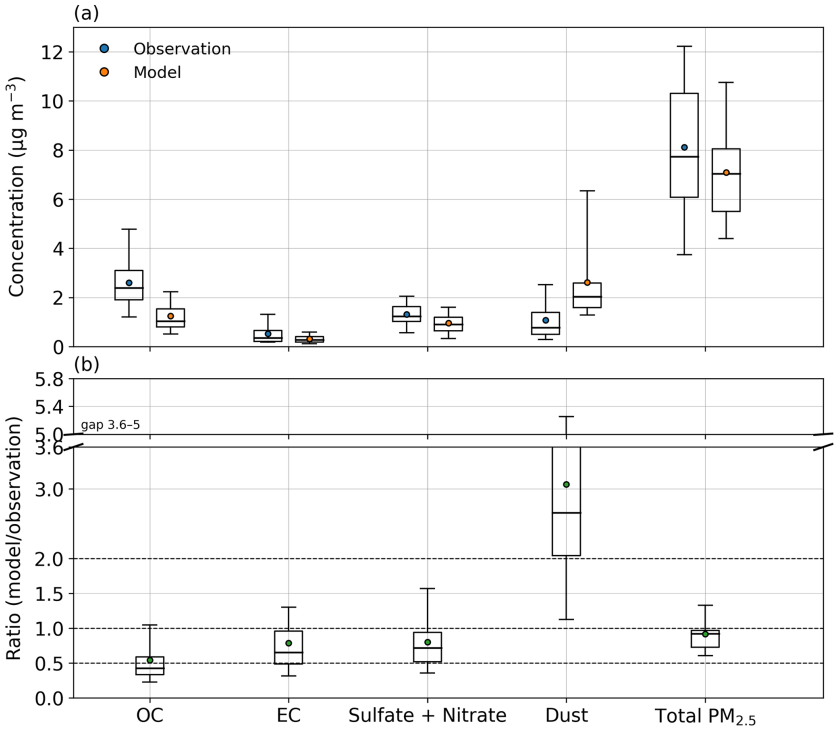

Figure 15. Box-whisker plots of **(a)** total and speciated $PM_{2.5}$ concentrations from UI-WRF-Chem simulation (mp2cu5 in Table 3) and surface observations from IMPROVE and CSN sites over the inner domain (D2) of PTA-Atlanta for June 2022, and **(b)** the ratio of model simulated to observed $PM_{2.5}$. Speciated $PM_{2.5}$ include OC, EC, dust and the combined sulfate + nitrate. Also Shown on the boxer plot are the 5th and 95th percentiles (the whiskers), the interquartile range (the boxes), the median (the black lines) and the mean (the filled circles). Note on **(b)**, the *y* axis is truncated between 3.6–5.0 for improved visualization.

MERRA-2 data being considered: no chemical species; including dust and other aerosols. Here, we develop a method to constrain the dust concentration for each size bin in the MERRA-2 data using AERONET data. We compare the dust PSD from MERRA-2 data with AERONET observations to better distribute the dust concentration in different size bins in the MERRA-2 chemical boundary conditions, based on long-term datasets. Our results show that including the dust and other aerosols in the boundary improve model simulated surface PM concentration and AOD during dust intrusion events for both target areas, compared to the model run without using MERRA-2 chemical boundary conditions. Using the constrained dust concentration in the MERRA-2 data further improves model performance. This method helps reduce the computational cost when long-range transport or regional transport affects a target area. Otherwise, we would need to add a third nested domain with expanded domain size to cover the pollution sources such as the dust source region. Since our work mainly focuses on improving the representation of the dust size distribution in MERRA-2 data, we recognize that other global models such as CAM-Chem may also provide useful information for chemical boundary conditions in different applications. While a comprehensive understanding of how different global models affect WRF-Chem simulations of special events such as the dust long-range transport, would provide valuable insights to the community, our work here demonstrates an efficient way for improving the simulation of dust transport using WRF-Chem.

Updating land surface properties (land cover type, LAI, GVF and surface albedo) with recent available MODIS land data improves model simulated TSK compared with MODIS LST, which is demonstrated over the CHN-Beijing target area for July 2018. This could help better capture the UHI phenomenon, which leads to better simulation of processes that are important for surface PM simulation. For other PTAs, which have experienced rapid urbanization, updating land cover type and other land surface properties with recent MODIS land data can be important since the default datasets used in the standard WRF-Chem model are outdated. We also recognize that we have not investigated the use of an urban canopy model to simulate the UHI effect in the UI-WRF-Chem framework. The newly updated BDISNP soil NO_x emission scheme improves the simulation of NO_2, which subsequently affects surface nitrate. Evaluated against TROPOMI NO_2 VCD, the updated BDISNP soil NO_x emission scheme increases NO_2 VCD, mainly over croplands in CHN-Beijing target area than the simulation using the default MEGAN soil NO_x emission scheme, which is mainly due to

the application of fertilizer use. Since ground observations of surface NO_2, O_3, and $PM_{2.5}$ concentrations are mostly located in urban areas, we acknowledge that our current work is limited in scope, and additional efforts will be needed to further evaluate the impacts of this updated BDISNP scheme in rural areas. Nevertheless, the launch of the GEMS and the Tropospheric Emissions: Monitoring of Pollution (TEMPO) (Zoogman et al., 2017) satellites will provide good opportunities to further refine the BDISNP scheme. The synergy between MAIA and GEMS/TEMPO will also provide opportunities to evaluate both gas and aerosol composition simultaneously.

We perform a case study over the USA-LosAngeles target area, where we tune dust emissions inside the target area. Southwestern U.S., covering part of the USA-LosAngeles target area are desert regions, which experience dust outbreaks. If we use the default dust emission scheme, the model simulated surface PM and AOD overestimate ground observations. We conduct sensitivity simulations to fine tune the parameters in the dust emission scheme as commonly done in the literature to find the optimal parameter. The case study over USA-LosAngeles together with other case studies give an example of the fine-tuning work we are doing as we continue evaluating and improving model performance.

We also use PTA-Atlanta as an example to demonstrate how UI-WRF-Chem simulates speciated $PM_{2.5}$. Overall, model simulated daily OC, EC and dust show higher correlation (0.5, 0.71 and 0.72) while the combined sulfate + nitrate aerosol concentration shows relatively lower correlation (0.23), when evaluated against measurements from IMPROVE and CSN networks. Since our work is based on only one month of data with precipitation events, the simulated total and speciated $PM_{2.5}$ concentrations are subject to large uncertainty and variability, particularly due to chemistry and wet deposition schemes associated with precipitation. As a result, this analysis only provides a partial picture of the model performance. Nevertheless, previous work by Jin et al. (2024) demonstrated the robustness of the UI-WRF-Chem framework over the Boston PTA, showing its feasibility for generating MAIA L2 and L4 PM products. Using a full year (2018) of UI-WRF-Chem outputs, they reported correlations of 0.40–0.73 between simulated and observed total and speciated $PM_{2.5}$ (Table S1 in the Supplement therein).

The MAIA project leverages existing PM monitoring networks where available and has deployed additional PM speciation monitors in PTAs where such data were otherwise unavailable, including through the Surface Particulate Matter Network (SPARTAN) (Snider et al., 2015). At the time of writing, long-term datasets of speciated $PM_{2.5}$ from observations are only available for some PTAs and extended model outputs are not yet available for all PTAs. We have since generated extended UI-WRF-Chem model outputs for each PTA and longer observations of speciated $PM_{2.5}$ are being collected. As part of the MAIA satellite mission, these expanded UI-WRF-Chem model outputs will enable a more comprehensive assessment of UI-WRF-Chem model performance, especially for speciated $PM_{2.5}$ across diverse PTAs. Such evaluation will enhance the robustness of UI-WRF-Chem for its role in the MAIA satellite mission and provide valuable insights for simulating PM composition in support of air quality and public health studies.

Code and data availability. The codes used in this work are available at: https://doi.org/10.5281/zenodo.15074107 (Zhang, 2025a). WRF-Chem is an open-access model, which is available at GitHub (WRF-model, 2022). The WRF-Chem preprocessor tools including mozbc, bio_emiss, anthro_emiss and EPA_ANTHRO_EMIS are available at: https://www2.acom.ucar.edu/wrf-chem/wrf-chem-tools-community (last access: 10 May 2022). Input files for bio_emiss and U.S. EPA NEI 2017 data can also be acquired from this website. EDGAR-HTAP global anthropogenic emission data are available at: https://edgar.jrc.ec.europa.eu/dataset_htap_v3 (last access: 1 December 2023). MEIC anthropogenic emission data for China are available at: http://meicmodel.org.cn/?page_id=1772&lang=en (last access: 1 November 2023). MODIS and VIIRS data are available at: https://ladsweb.modaps.eosdis.nasa.gov/ (last access: 15 August 2024); CALIOP data are downloaded from https://asdc.larc.nasa.gov/project/CALIPSO (last access: 9 July 2020); MERRA-2, GLDAS, NLDAS, TROPOIMI and GPM data can be acquired from https://disc.gsfc.nasa.gov/ (last access: 10 November 2024). Both ground observations of meteorology and PM data for Beijing are available at: https://quotsoft.net/air/ (last access: 15 November 2023). Ground observations of meteorology and PM data for Los Angeles as well as PM data for Atlanta are from https://aqs.epa.gov/aqsweb/airdata/download_files.html (last access: 22 January 2025). Ground observations of meteorology data for Rome and Atlanta are from https://www.ncei.noaa.gov/pub/data/noaa/isd-lite/ (last access: 29 November 2024). Speciated $PM_{2.5}$ data from both IMPROVE and CSN networks are available at https://views.cira.colostate.edu/fed/Membership/Login.aspx?ReturnUrl=%2ffed%2fQueryWizard (last access: 6 August 2025). Ground observations of PM data for Rome are available from https://search.earthdata.nasa.gov/search (use key words MAIA PM data) (last access: 18 April 2025). AERONET data can be downloaded at: https://aeronet.gsfc.nasa.gov/ (last access: 18 April 2025). Other datasets that are used and created in this work are available at: https://doi.org/10.5281/zenodo.15239058 (Zhang, 2025b).

Supplement. The supplement related to this article is available online at https://doi.org/10.5194/gmd-18-9061-2025-supplement.

Author contributions. HZ and JW conceived and designed the study. HZ performed all the simulations except for the Los Angeles case, conducted data analysis and wrote the initial manuscript draft. CG and JW constructed the UI-WRF-Chem modeling framework at the initial stage. HZ and NJ later served as the main developers for the UI-WRF-Chem modeling framework, under the guidance of JW. HZ manages the ongoing code updates. MZ developed the method

of using AERONET climatology data to constrain the MERRA-2 dust concentration for each size bin when updating chemical boundary conditions and contributed to the selection of physics schemes used for model configuration. LCG supported the development of Linux scripts, data acquisition and Python code development. TS developed the BDISNP soil NO_x emission scheme with the assistance of HZ and NJ and YiW improved the soil temperature response function within the scheme. YaW developed the modules to update land surface properties using MODIS data with support from HZ and NJ. CL updated the NEI 2017 and EDGAR-HTAP v3 emission inventories in the WEPS module with guidance from HZ. WD conducted the simulation for Los Angeles and ZX contributed to the simulation for Atlanta. WD, ZX and LC contributed to updates of land surface properties. HZ and SV collaborated on verifying the implementation of UI-WRF-Chem modeling framework and SV contributed to the design of the framework for operational use. JLM, SEG and DJD provided feedback on the implementation of the UI-WRF-Chem modeling framework in support of the MAIA satellite mission. SH assisted with the use of surface observation of PM in Italy. PRC and AMDS provided support and guidance on the use of GEOS data. JK provided input on the conceptual framework for future extension of this work. All authors contributed to the manuscript revision.

Competing interests. The contact author has declared that none of the authors has any competing interests.

Disclaimer. Publisher's note: Copernicus Publications remains neutral with regard to jurisdictional claims made in the text, published maps, institutional affiliations, or any other geographical representation in this paper. While Copernicus Publications makes every effort to include appropriate place names, the final responsibility lies with the authors. Views expressed in the text are those of the authors and do not necessarily reflect the views of the publisher.

Acknowledgements. We sincerely thank NASA Jet Propulsion Laboratory (JPL) (subcontract no. 1583456) for funding this research. The work of Sebastian Val, James L. McDuffie, Sina Hasheminassab, Scott E. Gluck and David J. Diner was carried out at the JPL, California Institute of Technology, under a contract with NASA (80NM0018D0004). We acknowledge the public availability of the various satellite datasets used here from NASA's different Distributed Active Archive Centers (DAACs): MODIS and VIIRS data from Level 1 and Atmosphere Archive and Distribution System (LAADS DAAC); the CALIOP data from Atmospheric Science Data Center (ASDC) at NASA's Langley Research Center; MERRA-2, GLDAS, NLDAS, TROPOMI and GPM data from the Goddard Earth Sciences Data and Information Service Center (GES DISC). We are grateful for the ground observations of meteorology variables (e.g., t2), provided by the Meteorological Information Comprehensive Analysis and Process System (MICAPS) in China, U.S. EPA and National Centers for Environmental Information (NCEI) Integrated Surface Database (ISD). We are thankful for the availability of ground observations of surface $PM_{2.5}$ and PM_{10} concentration from environmental monitoring stations managed by the Ministry of Environmental Protection in China, U.S. EPA, and ARPA Lazio and ARPAE Emilia Romagna in Italy. We are also thankful for the speciated $PM_{2.5}$ data from the IMPROVE and CSN networks in the U.S. We appreciate the AERONET networks for making their data publicly available and are grateful for the site PIs and data managers of the networks. We acknowledge the use of the WPS component in the NU-WRF system, which is available at: https://nuwrf.gsfc.nasa.gov/ (last access: 13 February 2019). We also acknowledge the use of the various WRF-Chem preprocessor tools (mozbc, bio_emiss, anthro_emiss and EPA_ANTHRO_EMIS), provided by the Atmospheric Chemistry Observations and Modeling Lab (ACOM) of National Center for Atmospheric Research (NCAR). We are also grateful for the anthropogenic emission inventories available to the public: EDGAR-HTAP global dataset provided by the European Commission, U.S. EPA NEI dataset by U.S. EPA and MEIC emission dataset for China provided by Tsinghua University. We thank Dr. Edward Hyer from the Naval Research Laboratory (NRL) for providing FLAMBE emission inventories. We also thank the Argon High-Performance Computing (HPC) system at the University of Iowa for the support. We are grateful for the two anonymous reviewers for their time and efforts to provide constructive feedback to improve our manuscript.

Financial support. The work carried out at the University of Iowa was supported by NASA JPL (subcontract no. 1583456), and the work carried out at NASA JPL was supported by NASA (contract no. 80NM0018D0004).

Review statement. This paper was edited by Cenlin He and reviewed by two anonymous referees.

References

Ackermann, I. J., Hass, H., Memmesheimer, M., Ebel, A., Binkowski, F. S., and Shankar, U.: Modal aerosol dynamics model for Europe: Development and first applications, Atmospheric Environment, 32, 2981–2999, 1998.

Adams-Selin, R. D., van den Heever, S. C., and Johnson, R. H.: Sensitivity of Bow-Echo Simulation to Microphysical Parameterizations, Weather and Forecasting, 28, 1188–1209, https://doi.org/10.1175/WAF-D-12-00108.1, 2013.

Aegerter, C., Wang, J., Ge, C., Irmak, S., Oglesby, R., Wardlow, B., Yang, H., You, J., and Shulski, M.: Mesoscale Modeling of the Meteorological Impacts of Irrigation during the 2012 Central Plains Drought, Journal of Applied Meteorology and Climatology, 56, 1259–1283, 2017.

Argüeso, D., Hidalgo-Muñoz, J. M., Gámiz-Fortis, S. R., Esteban-Parra, M. J., Dudhia, J., and Castro-Díez, Y.: Evaluation of WRF parameterizations for climate studies over southern Spain using a multistep regionalization, Journal of Climate, 24, 5633–5651, 2011.

Barnaba, F., Alvan Romero, N., Bolignano, A., Basart, S., Renzi, M., and Stafoggia, M.: Multiannual assessment of the desert dust impact on air quality in Italy combining PM_{10} data with physics-based and geostatistical models, Environment International, 163, 107204, https://doi.org/10.1016/j.envint.2022.107204, 2022.

Barnard, J. C., Fast, J. D., Paredes-Miranda, G., Arnott, W. P., and Laskin, A.: Technical Note: Evaluation of the WRF-Chem "Aerosol Chemical to Aerosol Optical Properties" Module using data from the MILAGRO campaign, Atmos. Chem. Phys., 10, 7325–7340, https://doi.org/10.5194/acp-10-7325-2010, 2010.

Benjamini, Y. and Hochberg, Y.: Controlling the false discovery rate: a practical and powerful approach to multiple testing, Journal of the Royal Statistical Society: Series B (Methodological), 57, 289–300, 1995.

Binkowski, F. S. and Shankar, U.: The Regional Particulate Matter Model: 1. Model description and preliminary results, Journal of Geophysical Research: Atmospheres, 100, 26191–26209, https://doi.org/10.1029/95jd02093, 1995.

Brisson, E., Demuzere, M., and Van Lipzig, N.: Modelling strategies for performing convection-permitting climate simulations, Meteorologische Zeitschrift, 25, 149–163, 2015.

Broxton, P. D., Zeng, X., Sulla-Menashe, D., and Troch, P. A.: A Global Land Cover Climatology Using MODIS Data, Journal of Applied Meteorology and Climatology, 53, 1593–1605, https://doi.org/10.1175/JAMC-D-13-0270.1, 2014.

Case, J. L., Kumar, S. V., Srikishen, J., and Jedlovec, G. J.: Improving Numerical Weather Predictions of Summertime Precipitation over the Southeastern United States through a High-Resolution Initialization of the Surface State, Weather and Forecasting, 26, 785–807, https://doi.org/10.1175/2011WAF2222455.1, 2011.

Chappell, A. and Webb, N. P.: Using albedo to reform wind erosion modelling, mapping and monitoring, Aeolian Research, 23, 63–78, https://doi.org/10.1016/j.aeolia.2016.09.006, 2016.

Chen, F. and Dudhia, J.: Coupling an advanced land surface–hydrology model with the Penn State–NCAR MM5 modeling system. Part I: Model implementation and sensitivity, Monthly Weather Review, 129, 569–585, 2001.

Chen, F., Mitchell, K., Schaake, J., Xue, Y., Pan, H. L., Koren, V., Duan, Q. Y., Ek, M., and Betts, A.: Modeling of land surface evaporation by four schemes and comparison with FIFE observations, Journal of Geophysical Research: Atmospheres, 101, 7251–7268, 1996.

Chen, S.-H. and Sun, W.-Y.: A one-dimensional time dependent cloud model, Journal of the Meteorological Society of Japan. Ser. II, 80, 99–118, 2002.

Chin, M., Ginoux, P., Kinne, S., Torres, O., Holben, B. N., Duncan, B. N., Martin, R. V., Logan, J. A., Higurashi, A., and Nakajima, T.: Tropospheric aerosol optical thickness from the GOCART model and comparisons with satellite and Sun photometer measurements, Journal of the Atmospheric Sciences, 59, 461–483, 2002.

Chou, M.-D., Suarez, M. J., Ho, C.-H., Yan, M. M., and Lee, K.-T.: Parameterizations for cloud overlapping and shortwave single-scattering properties for use in general circulation and cloud ensemble models, Journal of Climate, 11, 202–214, 1998.

Chutia, L., Wang, J., Zhang, H., Chen, X., Castro Garcia, L., and Janechek, N.: Elucidating the impacts of aerosol radiative effects for mitigating surface O_3 and $PM_{2.5}$ in Delhi, India during crop residue burning period, Atmospheric Environment, 339, 120890, https://doi.org/10.1016/j.atmosenv.2024.120890, 2024.

Clark, A. J., Gallus, W. A., Xue, M., and Kong, F.: A comparison of precipitation forecast skill between small convection-allowing and large convection-parameterizing ensembles, Weather and Forecasting, 24, 1121–1140, 2009.

Clinton, N. and Gong, P.: MODIS detected surface urban heat islands and sinks: Global locations and controls, Remote Sensing of Environment, 134, 294–304, 2013.

Cohen, A. J., Brauer, M., Burnett, R., Anderson, H. R., Frostad, J., Estep, K., Balakrishnan, K., Brunekreef, B., Dandona, L., and Dandona, R.: Estimates and 25-year trends of the global burden of disease attributable to ambient air pollution: an analysis of data from the Global Burden of Diseases Study 2015, The Lancet, 389, 1907–1918, 2017.

Colarco, P., da Silva, A., Chin, M., and Diehl, T.: Online simulations of global aerosol distributions in the NASA GEOS-4 model and comparisons to satellite and ground-based aerosol optical depth, Journal of Geophysical Research: Atmospheres, 115, https://doi.org/10.1029/2009JD012820, 2010.

Crippa, M., Solazzo, E., Huang, G., Guizzardi, D., Koffi, E., Muntean, M., Schieberle, C., Friedrich, R., and Janssens-Maenhout, G.: High resolution temporal profiles in the Emissions Database for Global Atmospheric Research, Scientific Data, 7, 121, https://doi.org/10.1038/s41597-020-0462-2, 2020.

Crippa, M., Guizzardi, D., Butler, T., Keating, T., Wu, R., Kaminski, J., Kuenen, J., Kurokawa, J., Chatani, S., Morikawa, T., Pouliot, G., Racine, J., Moran, M. D., Klimont, Z., Manseau, P. M., Mashayekhi, R., Henderson, B. H., Smith, S. J., Suchyta, H., Muntean, M., Solazzo, E., Banja, M., Schaaf, E., Pagani, F., Woo, J.-H., Kim, J., Monforti-Ferrario, F., Pisoni, E., Zhang, J., Niemi, D., Sassi, M., Ansari, T., and Foley, K.: The HTAP_v3 emission mosaic: merging regional and global monthly emissions (2000–2018) to support air quality modelling and policies, Earth Syst. Sci. Data, 15, 2667–2694, https://doi.org/10.5194/essd-15-2667-2023, 2023.

Crippa, P., Sullivan, R. C., Thota, A., and Pryor, S. C.: The impact of resolution on meteorological, chemical and aerosol properties in regional simulations with WRF-Chem, Atmos. Chem. Phys., 17, 1511–1528, https://doi.org/10.5194/acp-17-1511-2017, 2017.

Cummins, K., Noble, J., Varner, J. M., Robertson, K. M., Hiers, J. K., Nowell, H. K., and Simonson, E.: The Southeastern U.S. Prescribed Fire Permit Database: Hot Spots and Hot Moments in Prescribed Fire across the Southeastern U.S.A, Fire, 6, 372, https://doi.org/10.3390/fire6100372, 2023.

Darmenov, A. and da Silva, A.: The quick fire emissions dataset (QFED):Documentation of versions 2.1, 2.2 and 2.4, NASA/TM–2015–104606, https://ntrs.nasa.gov/citations/20180005253 (last access: 11 November 2025), 2015.

de Rosnay, P., Balsamo, G., Albergel, C., Muñoz-Sabater, J., and Isaksen, L.: Initialisation of land surface variables for numerical weather prediction, Surveys in Geophysics, 35, 607–621, 2014.

Dhital, S., Webb, N. P., Chappell, A., Kaplan, M. L., Nauman, T. W., Tyree, G., Duniway, M. C., Edwards, B., LeGrand, S. L., Letcher, T. W., McKenzie Skiles, S., Naple, P., Chaney, N. W., and Cai, J.: Synoptic Analysis and WRF-Chem Model Simulation of Dust Events in the Southwestern United States, Journal of Geophysical Research: Atmospheres, 129, e2023JD040650, https://doi.org/10.1029/2023JD040650, 2024.

Diao, M., Holloway, T., Choi, S., O'Neill, S. M., Al-Hamdan, M. Z., Van Donkelaar, A., Martin, R. V., Jin, X., Fiore, A. M., Henze, D. K., Lacey, F., Kinney, P. L., Freedman, F., Larkin, N. K., Zou, Y., Kelly, J. T., and Vaidyanathan, A.: Methods, availability, and applications of $PM_{2.5}$ exposure estimates derived from ground measurements, satellite, and atmospheric models, Jour-

nal of the Air & Waste Management Association, 69, 1391–1414, https://doi.org/10.1080/10962247.2019.1668498, 2019.

Dillon, M. E., Collini, E. A., and Ferreira, L. J.: Sensitivity of WRF short-term forecasts to different soil moisture initializations from the GLDAS database over South America in March 2009, Atmospheric Research, 167, 196–207, https://doi.org/10.1016/j.atmosres.2015.07.022, 2016.

Diner, D. J., Beckert, J. C., Reilly, T. H., Bruegge, C. J., Conel, J. E., Kahn, R. A., Martonchik, J. V., Ackerman, T. P., Davies, R., and Gerstl, S. A.: Multi-angle Imaging SpectroRadiometer (MISR) instrument description and experiment overview, IEEE Transactions on Geoscience and Remote Sensing, 36, 1072–1087, 1998.

Diner, D. J., Boland, S. W., Brauer, M., Bruegge, C., Burke, K. A., Chipman, R., Di Girolamo, L., Garay, M. J., Hasheminassab, S., and Hyer, E.: Advances in multiangle satellite remote sensing of speciated airborne particulate matter and association with adverse health effects: from MISR to MAIA, Journal of Applied Remote Sensing, 12, 042603, https://doi.org/10.1117/1.JRS.12.042603, 2018.

Done, J., Davis, C. A., and Weisman, M.: The next generation of NWP: explicit forecasts of convection using the weather research and forecasting (WRF) model, Atmospheric Science Letters, 5, 110–117, https://doi.org/10.1002/asl.72, 2004.

Du, Q., Zhao, C., Zhang, M., Dong, X., Chen, Y., Liu, Z., Hu, Z., Zhang, Q., Li, Y., Yuan, R., and Miao, S.: Modeling diurnal variation of surface $PM_{2.5}$ concentrations over East China with WRF-Chem: impacts from boundary-layer mixing and anthropogenic emission, Atmos. Chem. Phys., 20, 2839–2863, https://doi.org/10.5194/acp-20-2839-2020, 2020.

Dudhia, J.: A history of mesoscale model development, Asia-Pacific Journal of Atmospheric Sciences, 50, 121–131, 2014.

Emmons, L. K., Schwantes, R. H., Orlando, J. J., Tyndall, G., Kinnison, D., Lamarque, J.-F., Marsh, D., Mills, M. J., Tilmes, S., Bardeen, C., Buchholz, R. R., Conley, A., Gettelman, A., Garcia, R., Simpson, I., Blake, D. R., Meinardi, S., and Pétron, G.: The Chemistry Mechanism in the Community Earth System Model Version 2 (CESM2), Journal of Advances in Modeling Earth Systems, 12, e2019MS001882, https://doi.org/10.1029/2019MS001882, 2020.

Fast, J. D., Gustafson Jr, W. I., Easter, R. C., Zaveri, R. A., Barnard, J. C., Chapman, E. G., Grell, G. A., and Peckham, S. E.: Evolution of ozone, particulates, and aerosol direct radiative forcing in the vicinity of Houston using a fully coupled meteorology-chemistry-aerosol model, Journal of Geophysical Research: Atmospheres, 111, https://doi.org/10.1029/2005JD006721, 2006.

Forouzanfar, M. H., Afshin, A., Alexander, L. T., et al.: Global, regional, and national comparative risk assessment of 79 behavioural, environmental and occupational, and metabolic risks or clusters of risks, 1990–2015: a systematic analysis for the Global Burden of Disease Study 2015, The Lancet, 388, 1659–1724, https://doi.org/10.1016/S0140-6736(16)31679-8, 2016.

Friedl, M. A., McIver, D. K., Hodges, J. C. F., Zhang, X. Y., Muchoney, D., Strahler, A. H., Woodcock, C. E., Gopal, S., Schneider, A., Cooper, A., Baccini, A., Gao, F., and Schaaf, C.: Global land cover mapping from MODIS: algorithms and early results, Remote Sensing of Environment, 83, 287–302, https://doi.org/10.1016/S0034-4257(02)00078-0, 2002.

Gao, Y., Leung, L. R., Zhao, C., and Hagos, S.: Sensitivity of U.S. summer precipitation to model resolution and convective parameterizations across gray zone resolutions, Journal of Geophysical Research: Atmospheres, 122, 2714–2733, https://doi.org/10.1002/2016JD025896, 2017.

Ge, C., Wang, J., and Reid, J. S.: Mesoscale modeling of smoke transport over the Southeast Asian Maritime Continent: coupling of smoke direct radiative effect below and above the low-level clouds, Atmos. Chem. Phys., 14, 159–174, https://doi.org/10.5194/acp-14-159-2014, 2014.

Ge, C., Wang, J., Reid, J. S., Posselt, D. J., Xian, P., and Hyer, E.: Mesoscale modeling of smoke transport from equatorial Southeast Asian Maritime Continent to the Philippines: First comparison of ensemble analysis with in situ observations, Journal of Geophysical Research: Atmospheres, 122, 5380–5398, 2017.

Gelaro, R., McCarty, W., Suárez, M. J., Todling, R., Molod, A., Takacs, L., Randles, C. A., Darmenov, A., Bosilovich, M. G., and Reichle, R.: The modern-era retrospective analysis for research and applications, version 2 (MERRA-2), Journal of Climate, 30, 5419–5454, 2017.

Georgiou, G. K., Christoudias, T., Proestos, Y., Kushta, J., Hadjinicolaou, P., and Lelieveld, J.: Air quality modelling in the summer over the eastern Mediterranean using WRF-Chem: chemistry and aerosol mechanism intercomparison, Atmos. Chem. Phys., 18, 1555–1571, https://doi.org/10.5194/acp-18-1555-2018, 2018.

Gettelman, A., Mills, M. J., Kinnison, D. E., Garcia, R. R., Smith, A. K., Marsh, D. R., Tilmes, S., Vitt, F., Bardeen, C. G., McInerny, J., Liu, H.-L., Solomon, S. C., Polvani, L. M., Emmons, L. K., Lamarque, J.-F., Richter, J. H., Glanville, A. S., Bacmeister, J. T., Phillips, A. S., Neale, R. B., Simpson, I. R., DuVivier, A. K., Hodzic, A., and Randel, W. J.: The Whole Atmosphere Community Climate Model Version 6 (WACCM6), Journal of Geophysical Research: Atmospheres, 124, 12380–12403, https://doi.org/10.1029/2019JD030943, 2019.

Gilleland, E., Ahijevych, D., Brown, B. G., Casati, B., and Ebert, E. E.: Intercomparison of spatial forecast verification methods, Weather and Forecasting, 24, 1416–1430, 2009.

Ginoux, P., Chin, M., Tegen, I., Prospero, J. M., Holben, B., Dubovik, O., and Lin, S. J.: Sources and distributions of dust aerosols simulated with the GOCART model, Journal of Geophysical Research: Atmospheres, 106, 20255–20273, 2001.

Grell, G. A. and Dévényi, D.: A generalized approach to parameterizing convection combining ensemble and data assimilation techniques, Geophysical Research Letters, 29, 38-31–38-34, 2002.

Grell, G. A. and Freitas, S. R.: A scale and aerosol aware stochastic convective parameterization for weather and air quality modeling, Atmos. Chem. Phys., 14, 5233–5250, https://doi.org/10.5194/acp-14-5233-2014, 2014.

Grell, G. A., Dudhia, J., and Stauffer, D. R.: A description of the fifth-generation Penn State/NCAR Mesoscale Model (MM5), NCAR Tech. Note TN-398+STR, https://doi.org/10.5065/D60Z716B, 1994.

Grell, G. A., Peckham, S. E., Schmitz, R., McKeen, S. A., Frost, G., Skamarock, W. C., and Eder, B.: Fully coupled "online" chemistry within the WRF model, Atmospheric Environment, 39, 6957–6975, 2005.

Guenther, A., Karl, T., Harley, P., Wiedinmyer, C., Palmer, P., and Geron, C.: Estimates of global terrestrial isoprene emissions using MEGAN (Model of Emissions of Gases and Aerosols from Nature), Atmos. Chem. Phys., 6, 3181–3210, https://doi.org/10.5194/acp-6-3181-2006, 2006.

Guenther, A., Jiang, X., Heald, C., Sakulyanontvittaya, T., Duhl, T., Emmons, L., and Wang, X.: The Model of Emissions of Gases and Aerosols from Nature version 2.1 (MEGAN2.1): an extended and updated framework for modeling biogenic emissions, Geosci. Model Dev., 5, 1471–1492, https://doi.org/10.5194/gmd-5-1471-2012, 2012.

Han, B., Fan, J., Varble, A., Morrison, H., Williams, C. R., Chen, B., Dong, X., Giangrande, S. E., Khain, A., Mansell, E., Milbrandt, J. A., Shpund, J., and Thompson, G.: Cloud-Resolving Model Intercomparison of an MC3E Squall Line Case: Part II. Stratiform Precipitation Properties, Journal of Geophysical Research: Atmospheres, 124, 1090–1117, https://doi.org/10.1029/2018JD029596, 2019.

Han, T., Pan, X., and Wang, X.: Evaluating and improving the sand storm numerical simulation performance in Northwestern China using WRF-Chem and remote sensing soil moisture data, Atmospheric Research, 251, 105411, https://doi.org/10.1016/j.atmosres.2020.105411, 2021.

Hand, J., Prenni, A., and Schichtel, B.: Trends in seasonal mean speciated aerosol composition in remote areas of the United States from 2000 through 2021, Journal of Geophysical Research: Atmospheres, 129, e2023JD039902, 2024.

He, X., Li, Y., Wang, X., Chen, L., Yu, B., Zhang, Y., and Miao, S.: High-resolution dataset of urban canopy parameters for Beijing and its application to the integrated WRF/Urban modelling system, Journal of Cleaner Production, 208, 373–383, https://doi.org/10.1016/j.jclepro.2018.10.086, 2019.

Holloway, T., Miller, D., Anenberg, S., Diao, M., Duncan, B., Fiore, A. M., Henze, D. K., Hess, J., Kinney, P. L., Liu, Y., Neu, J. L., O'Neill, S. M., Odman, M. T., Pierce, R. B., Russell, A. G., Tong, D., West, J. J., and Zondlo, M. A.: Satellite Monitoring for Air Quality and Health, Annual Review of Biomedical Data Science, 4, https://doi.org/10.1146/annurev-biodatasci-110920-093120, 2021.

Hong, S.-Y. and Lim, J.-O. J.: The WRF single-moment 6-class microphysics scheme (WSM6), Asia-Pacific Journal of Atmospheric Sciences, 42, 129–151, 2006.

Hong, S.-Y., Noh, Y., and Dudhia, J.: A new vertical diffusion package with an explicit treatment of entrainment processes, Monthly Weather Review, 134, 2318–2341, 2006.

Hu, J., Ostro, B., Zhang, H., Ying, Q., and Kleeman, M. J.: Using Chemical Transport Model Predictions To Improve Exposure Assessment of $PM_{2.5}$ Constituents, Environmental Science & Technology Letters, 6, 456–461, https://doi.org/10.1021/acs.estlett.9b00396, 2019.

Hudman, R. C., Moore, N. E., Mebust, A. K., Martin, R. V., Russell, A. R., Valin, L. C., and Cohen, R. C.: Steps towards a mechanistic model of global soil nitric oxide emissions: implementation and space based-constraints, Atmos. Chem. Phys., 12, 7779–7795, https://doi.org/10.5194/acp-12-7779-2012, 2012.

Hyde, P., Mahalov, A., and Li, J.: Simulating the meteorology and PM10 concentrations in Arizona dust storms using the Weather Research and Forecasting model with Chemistry (Wrf-Chem), Journal of the Air & Waste Management Association, 68, 177–195, 2018.

Iacono, M. J., Delamere, J. S., Mlawer, E. J., Shephard, M. W., Clough, S. A., and Collins, W. D.: Radiative forcing by long-lived greenhouse gases: Calculations with the AER radiative transfer models, Journal of Geophysical Research: Atmospheres, 113, https://doi.org/10.1029/2008JD009944, 2008.

Ichoku, C. and Ellison, L.: Global top-down smoke-aerosol emissions estimation using satellite fire radiative power measurements, Atmos. Chem. Phys., 14, 6643–6667, https://doi.org/10.5194/acp-14-6643-2014, 2014.

Jaeglé, L., Steinberger, L., Martin, R. V., and Chance, K.: Global partitioning of NO × sources using satellite observations: Relative roles of fossil fuel combustion, biomass burning and soil emissions, Faraday Discussions, 130, 407–423, 2005.

Janjic, Z.: Nonsingular implementation of the Mellor-Yamada Level 2.5 Scheme in the NCEP Meso model, National Centers for Environmental Prediction, Office Note, https://repository.library.noaa.gov/view/noaa/11409/noaa_11409_DS1.pdf (last access: 12 November 2025), 2001.

Janssens-Maenhout, G., Crippa, M., Guizzardi, D., Dentener, F., Muntean, M., Pouliot, G., Keating, T., Zhang, Q., Kurokawa, J., Wankmüller, R., Denier van der Gon, H., Kuenen, J. J. P., Klimont, Z., Frost, G., Darras, S., Koffi, B., and Li, M.: HTAP_v2.2: a mosaic of regional and global emission grid maps for 2008 and 2010 to study hemispheric transport of air pollution, Atmos. Chem. Phys., 15, 11411–11432, https://doi.org/10.5194/acp-15-11411-2015, 2015.

Jenkins, G. S. and Diokhane, A. M.: WRF prediction of two winter season Saharan dust events using PM_{10} concentrations: Boundary versus initial conditions, Atmospheric Environment, 167, 129–142, https://doi.org/10.1016/j.atmosenv.2017.08.010, 2017.

Jeworrek, J., West, G., and Stull, R.: Evaluation of cumulus and microphysics parameterizations in WRF across the convective gray zone, Weather and Forecasting, 34, 1097–1115, 2019.

Jeworrek, J., West, G., and Stull, R.: WRF precipitation performance and predictability for systematically varied parameterizations over complex terrain, Weather and Forecasting, 36, 893–913, 2021.

Jiménez, P. A. and Dudhia, J.: Improving the representation of resolved and unresolved topographic effects on surface wind in the WRF model, Journal of Applied Meteorology and Climatology, 51, 300–316, 2012.

Jiménez, P. A., Dudhia, J., González-Rouco, J. F., Navarro, J., Montávez, J. P., and García-Bustamante, E.: A Revised Scheme for the WRF Surface Layer Formulation, Monthly Weather Review, 140, 898–918, https://doi.org/10.1175/MWR-D-11-00056.1, 2012.

Jin, Z., Pu, Q., Janechek, N., Zhang, H., Wang, J., Chang, H., and Liu, Y.: A MAIA-like modeling framework to estimate $PM_{2.5}$ mass and speciation concentrations with uncertainty, Remote Sensing of Environment, 303, 113995, https://doi.org/10.1016/j.rse.2024.113995, 2024.

Jung, E. and Shao, Y.: An intercomparison of four wet deposition schemes used in dust transport modeling, Global and Planetary Change, 52, 248–260, https://doi.org/10.1016/j.gloplacha.2006.02.008, 2006.

Justice, C., Townshend, J., Vermote, E., Masuoka, E., Wolfe, R., Saleous, N., Roy, D., and Morisette, J.: An overview of MODIS Land data processing and product status, Remote Sensing of Environment, 83, 3–15, 2002.

Kahn, R. A., Gaitley, B. J., Martonchik, J. V., Diner, D. J., Crean, K. A., and Holben, B.: Multiangle Imaging Spectroradiometer (MISR) global aerosol optical depth validation based on 2

years of coincident Aerosol Robotic Network (AERONET) observations, Journal of Geophysical Research: Atmospheres, 110, https://doi.org/10.1029/2004JD004706, 2005.

Kain, J. S.: The Kain–Fritsch Convective Parameterization: An Update, Journal of Applied Meteorology, 43, 170–181, https://doi.org/10.1175/1520-0450(2004)043<0170:TKCPAU>2.0.CO;2, 2004.

Kaiser, J. W., Heil, A., Andreae, M. O., Benedetti, A., Chubarova, N., Jones, L., Morcrette, J.-J., Razinger, M., Schultz, M. G., Suttie, M., and van der Werf, G. R.: Biomass burning emissions estimated with a global fire assimilation system based on observed fire radiative power, Biogeosciences, 9, 527–554, https://doi.org/10.5194/bg-9-527-2012, 2012.

Kim, J., Jeong, U., Ahn, M.-H., Kim, J. H., Park, R. J., Lee, H., Song, C. H., Choi, Y.-S., Lee, K.-H., and Yoo, J.-M.: New era of air quality monitoring from space: Geostationary Environment Monitoring Spectrometer (GEMS), Bulletin of the American Meteorological Society, 101, E1–E22, 2020.

Klein, C., Heinzeller, D., Bliefernicht, J., and Kunstmann, H.: Variability of West African monsoon patterns generated by a WRF multi-physics ensemble, Climate Dynamics, 45, 2733–2755, 2015.

Koster, R. D., Suarez, M. J., Ducharne, A., Stieglitz, M., and Kumar, P.: A catchment-based approach to modeling land surface processes in a general circulation model: 1. Model structure, Journal of Geophysical Research: Atmospheres, 105, 24809–24822, 2000.

Kramer, S. J., Alvarez, C., Barkley, A. E., Colarco, P. R., Custals, L., Delgadillo, R., Gaston, C. J., Govindaraju, R., and Zuidema, P.: Apparent dust size discrepancy in aerosol reanalysis in north African dust after long-range transport, Atmos. Chem. Phys., 20, 10047–10062, https://doi.org/10.5194/acp-20-10047-2020, 2020.

Kumar, S. V., Peters-Lidard, C. D., Tian, Y., Houser, P. R., Geiger, J., Olden, S., Lighty, L., Eastman, J. L., Doty, B., Dirmeyer, P., Adams, J., Mitchell, K., Wood, E. F., and Sheffield, J.: Land information system: An interoperable framework for high resolution land surface modeling, Environmental Modelling & Software, 21, 1402–1415, https://doi.org/10.1016/j.envsoft.2005.07.004, 2006.

Kumar, S. V., Peters-Lidard, C. D., Eastman, J. L., and Tao, W.-K.: An integrated high-resolution hydrometeorological modeling testbed using LIS and WRF, Environmental Modelling & Software, 23, 169–181, 2008.

Lee, J., Hsu, N. C., Sayer, A. M., Bettenhausen, C., and Yang, P.: AERONET-Based Nonspherical Dust Optical Models and Effects on the VIIRS Deep Blue/SOAR Over Water Aerosol Product, Journal of Geophysical Research: Atmospheres, 122, 10384–10401, https://doi.org/10.1002/2017JD027258, 2017.

LeGrand, S. L., Polashenski, C., Letcher, T. W., Creighton, G. A., Peckham, S. E., and Cetola, J. D.: The AFWA dust emission scheme for the GOCART aerosol model in WRF-Chem v3.8.1, Geosci. Model Dev., 12, 131–166, https://doi.org/10.5194/gmd-12-131-2019, 2019.

LeGrand, S. L., Letcher, T. W., Okin, G. S., Webb, N. P., Gallagher, A. R., Dhital, S., Hodgdon, T. S., Ziegler, N. P., and Michaels, M. L.: Application of a satellite-retrieved sheltering parameterization (v1.0) for dust event simulation with WRF-Chem v4.1, Geosci. Model Dev., 16, 1009–1038, https://doi.org/10.5194/gmd-16-1009-2023, 2023.

Li, C., Wang, J., Zhang, H., Diner, D. J., Hasheminassab, S., and Janechek, N.: Improvement of Surface $PM_{2.5}$ Diurnal Variation Simulations in East Africa for the MAIA Satellite Mission, ACS ES&T Air, 1, 223–233, https://doi.org/10.1021/acsestair.3c00008, 2024.

Li, M., Song, Y., Huang, X., Li, J., Mao, Y., Zhu, T., Cai, X., and Liu, B.: Improving mesoscale modeling using satellite-derived land surface parameters in the Pearl River Delta region, China, Journal of Geophysical Research: Atmospheres, 119, 6325–6346, 2014.

Li, M., Wang, T., Xie, M., Zhuang, B., Li, S., Han, Y., Song, Y., and Cheng, N.: Improved meteorology and ozone air quality simulations using MODIS land surface parameters in the Yangtze River Delta urban cluster, China, Journal of Geophysical Research: Atmospheres, 122, 3116–3140, 2017a.

Li, M., Liu, H., Geng, G., Hong, C., Liu, F., Song, Y., Tong, D., Zheng, B., Cui, H., and Man, H.: Anthropogenic emission inventories in China: a review, National Science Review, 4, 834–866, 2017b.

Li, Y., Pickering, K. E., Barth, M. C., Bela, M. M., Cummings, K. A., and Allen, D. J.: Evaluation of Parameterized Convective Transport of Trace Gases in Simulation of Storms Observed During the DC3 Field Campaign, Journal of Geophysical Research: Atmospheres, 123, 11238–11261, https://doi.org/10.1029/2018JD028779, 2018.

Li, Y., Pickering, K. E., Barth, M. C., Bela, M. M., Cummings, K. A., and Allen, D. J.: Wet Scavenging in WRF-Chem Simulations of Parameterized Convection for a Severe Storm During the DC3 Field Campaign, Journal of Geophysical Research: Atmospheres, 124, 7413–7428, https://doi.org/10.1029/2019JD030484, 2019.

Li, Y., Yuan, S., Fan, S., Song, Y., Wang, Z., Yu, Z., Yu, Q., and Liu, Y.: Satellite Remote Sensing for Estimating $PM_{2.5}$ and Its Components, Curr Pollution Rep 7, 72–87, https://doi.org/10.1007/s40726-020-00170-4, 2021.

Li, Z., Maji, K. J., Hu, Y., Vaidyanathan, A., O'Neill, S. M., Odman, M. T., and Russell, A. G.: An Analysis of Prescribed Fire Activities and Emissions in the Southeastern United States from 2013 to 2020, Remote Sensing, 15, 2725, https://doi.org/10.3390/rs15112725, 2023.

Liang, T., He, J., Chen, L., Yao, Z., Zhang, L., Che, H., and Gong, S.: Simulation of the influence of a fine-scale urban underlying surface on the urban heat island effect in Beijing, Atmospheric Research, 262, 105786, https://doi.org/10.1016/j.atmosres.2021.105786, 2021.

Lin, Y.-C., Zhang, Y.-L., Yu, M., Fan, M.-Y., Xie, F., Zhang, W.-Q., Wu, G., Cong, Z., and Michalski, G.: Formation Mechanisms and Source Apportionments of Airborne Nitrate Aerosols at a Himalayan-Tibetan Plateau Site: Insights from Nitrogen and Oxygen Isotopic Compositions, Environmental Science & Technology, 55, 12261–12271, 2021.

Lin, Y.-L., Farley, R. D., and Orville, H. D.: Bulk parameterization of the snow field in a cloud model, Journal of Applied Meteorology and climatology, 22, 1065–1092, 1983.

Liu, Y. and Diner, D. J.: Multi-angle imager for aerosols: a satellite investigation to benefit public health, Public Health Reports, 132, 14–17, 2017.

Liu, Y., Chen, D., Kahn, R. A., and He, K.: Review of the applications of multiangle imaging spectroradiometer to air quality research, Science in China Series D: Earth Sciences, 52, 132–144, 2009.

Madronich, S.: Photodissociation in the atmosphere: 1. Actinic flux and the effects of ground reflections and clouds. Journal of Geophysical Research: Atmospheres, 92, 9740–9752, https://doi.org/10.1029/JD092iD08p09740, 1987.

Malm, W. C., Sisler, J. F., Huffman, D., Eldred, R. A., and Cahill, T. A.: Spatial and seasonal trends in particle concentration and optical extinction in the United States, Journal of Geophysical Research: Atmospheres, 99, 1347–1370, 1994.

Meng, X., Garay, M. J., Diner, D. J., Kalashnikova, O. V., Xu, J., and Liu, Y.: Estimating $PM_{2.5}$ speciation concentrations using prototype 4.4 km-resolution MISR aerosol properties over Southern California, Atmospheric Environment, 181, 70–81, 2018.

Menut, L., Tuccella, P., Flamant, C., Deroubaix, A., and Gaetani, M.: The role of aerosol–radiation–cloud interactions in linking anthropogenic pollution over southern west Africa and dust emission over the Sahara, Atmos. Chem. Phys., 19, 14657–14676, https://doi.org/10.5194/acp-19-14657-2019, 2019.

Mitchell, K. E., Lohmann, D., Houser, P. R., Wood, E. F., Schaake, J. C., Robock, A., Cosgrove, B. A., Sheffield, J., Duan, Q., and Luo, L.: The multi-institution North American Land Data Assimilation System (NLDAS): Utilizing multiple GCIP products and partners in a continental distributed hydrological modeling system, Journal of Geophysical Research: Atmospheres, 109, https://doi.org/10.1029/2003JD003823, 2004.

Mlawer, E. J., Taubman, S. J., Brown, P. D., Iacono, M. J., and Clough, S. A.: Radiative transfer for inhomogeneous atmospheres: RRTM, a validated correlated-k model for the longwave, Journal of Geophysical Research: Atmospheres, 102, 16663–16682, 1997.

Mo, J., Gong, S., Zhang, L., He, J., Lu, S., Zhou, Y., Ke, H., and Zhang, H.: Impacts of long-range transports from Central and South Asia on winter surface $PM_{2.5}$ concentrations in China, Science of The Total Environment, 777, 146243, https://doi.org/10.1016/j.scitotenv.2021.146243, 2021.

Mölders, N.: On the uncertainty in mesoscale modeling caused by surface parameters, Meteorology and Atmospheric Physics, 76, 119–141, 2001.

Morrison, H., Thompson, G., and Tatarskii, V.: Impact of cloud microphysics on the development of trailing stratiform precipitation in a simulated squall line: Comparison of one-and two-moment schemes, Monthly Weather Review, 137, 991–1007, 2009.

Nakanishi, M. and Niino, H.: An Improved Mellor–Yamada Level-3 Model with Condensation Physics: Its Design and Verification, Boundary-Layer Meteorology, 112, 1–31, https://doi.org/10.1023/B:BOUN.0000020164.04146.98, 2004.

Oikawa, P. Y., Ge, C., Wang, J., Eberwein, J. R., Liang, L. L., Allsman, L. A., Grantz, D. A., and Jenerette, G. D.: Unusually high soil nitrogen oxide emissions influence air quality in a high-temperature agricultural region, Nature Communications, 6, 8753, https://doi.org/10.1038/ncomms9753, 2015.

Oleson, K. W., Dai, Y., Bonan, G., Bosilovich, M., Dickinson, R., Dirmeyer, P., Hoffman, F., Houser, P., Levis, S., and Niu, G.-Y.: Technical description of the community land model (CLM), Tech. Note NCAR/TN-461+ STR, https://doi.org/10.5065/D6FB50WZ, 2004.

Peters-Lidard, C. D., Kemp, E. M., Matsui, T., Santanello, J. A., Kumar, S. V., Jacob, J. P., Clune, T., Tao, W.-K., Chin, M., Hou, A., Case, J. L., Kim, D., Kim, K.-M., Lau, W., Liu, Y., Shi, J., Starr, D., Tan, Q., Tao, Z., Zaitchik, B. F., Zavodsky, B., Zhang, S. Q., and Zupanski, M.: Integrated modeling of aerosol, cloud, precipitation and land processes at satellite-resolved scales, Environmental Modelling & Software, 67, 149–159, https://doi.org/10.1016/j.envsoft.2015.01.007, 2015.

Pey, J., Querol, X., Alastuey, A., Forastiere, F., and Stafoggia, M.: African dust outbreaks over the Mediterranean Basin during 2001–2011: PM_{10} concentrations, phenomenology and trends, and its relation with synoptic and mesoscale meteorology, Atmos. Chem. Phys., 13, 1395–1410, https://doi.org/10.5194/acp-13-1395-2013, 2013.

Philip, S., Martin, R. V., van Donkelaar, A., Lo, J. W.-H., Wang, Y., Chen, D., Zhang, L., Kasibhatla, P. S., Wang, S., and Zhang, Q.: Global chemical composition of ambient fine particulate matter for exposure assessment, Environmental Science & Technology, 48, 13060–13068, 2014.

Prein, A. F., Langhans, W., Fosser, G., Ferrone, A., Ban, N., Goergen, K., Keller, M., Tölle, M., Gutjahr, O., Feser, F., Brisson, E., Kollet, S., Schmidli, J., van Lipzig, N. P. M., and Leung, R.: A review on regional convection-permitting climate modeling: Demonstrations, prospects, and challenges, Reviews of Geophysics, 53, 323–361, https://doi.org/10.1002/2014RG000475, 2015.

Querol, X., Pey, J., Pandolfi, M., Alastuey, A., Cusack, M., Pérez, N., Moreno, T., Viana, M., Mihalopoulos, N., Kallos, G., and Kleanthous, S.: African dust contributions to mean ambient PM_{10} mass-levels across the Mediterranean Basin, Atmospheric Environment, 43, 4266–4277, https://doi.org/10.1016/j.atmosenv.2009.06.013, 2009.

Randles, C., Da Silva, A., Buchard, V., Colarco, P., Darmenov, A., Govindaraju, R., Smirnov, A., Holben, B., Ferrare, R., and Hair, J.: The MERRA-2 aerosol reanalysis, 1980 onward. Part I: System description and data assimilation evaluation, Journal of Climate, 30, 6823–6850, 2017.

Reid, J. S., Hyer, E. J., Prins, E. M., Westphal, D. L., Zhang, J., Wang, J., Christopher, S. A., Curtis, C. A., Schmidt, C. C., and Eleuterio, D. P.: Global monitoring and forecasting of biomass-burning smoke: Description of and lessons from the Fire Locating and Modeling of Burning Emissions (FLAMBE) program, IEEE Journal of Selected Topics in Applied Earth Observations and Remote Sensing, 2, 144–162, 2009.

Rienecker, M. M., Suarez, M., Todling, R., Bacmeister, J., Takacs, L., Liu, H., Gu, W., Sienkiewicz, M., Koster, R., and Gelaro, R.: The GEOS-5 Data Assimilation System: Documentation of Versions 5.0.1, 5.1.0, and 5.2.0, NASA/TM-2008-104606-VOL-27, https://ntrs.nasa.gov/citations/20120011955 (last access: 12 November 2025), 2008.

Roberts, G. J. and Wooster, M. J.: Fire detection and fire characterization over Africa using Meteosat SEVIRI, IEEE Transactions on Geoscience and Remote Sensing, 46, 1200–1218, 2008.

Rodell, M., Houser, P., Jambor, U., Gottschalck, J., Mitchell, K., Meng, C.-J., Arsenault, K., Cosgrove, B., Radakovich, J., and Bosilovich, M.: The global land data assimilation system, Bulletin of the American Meteorological Society, 85, 381–394, 2004.

Roozitalab, B., Carmichael, G. R., and Guttikunda, S. K.: Improving regional air quality predictions in the Indo-Gangetic Plain – case study of an intensive pollution episode in November 2017, Atmos. Chem. Phys., 21, 2837–2860, https://doi.org/10.5194/acp-21-2837-2021, 2021.

Rossa, A., Nurmi, P., and Ebert, E.: Overview of methods for the verification of quantitative precipitation forecasts, in: Precipitation: Advances in measurement, estimation and prediction, Springer, 419–452, https://doi.org/10.1007/978-3-540-77655-0_16, 2008.

Sangkham, S., Phairuang, W., Sherchan, S. P., Pansakun, N., Munkong, N., Sarndhong, K., Islam, M. A., and Sakunkoo, P.: An update on adverse health effects from exposure to $PM_{2.5}$, Environmental Advances, 18, 100603, https://doi.org/10.1016/j.envadv.2024.100603, 2024.

Schell, B., Ackermann, I. J., Hass, H., Binkowski, F. S., and Ebel, A.: Modeling the formation of secondary organic aerosol within a comprehensive air quality model system, Journal of Geophysical Research: Atmospheres, 106, 28275–28293, 2001.

Sha, T., Ma, X., Zhang, H., Janechek, N., Wang, Y., Wang, Y., Castro García, L., Jenerette, G. D., and Wang, J.: Impacts of Soil NO_x Emission on O_3 Air Quality in Rural California, Environmental Science & Technology, https://doi.org/10.1021/acs.est.0c06834, 2021.

Shao, Y., Ishizuka, M., Mikami, M., and Leys, J.: Parameterization of size-resolved dust emission and validation with measurements, Journal of Geophysical Research: Atmospheres, 116, https://doi.org/10.1029/2010JD014527, 2011.

Shin, M., Kang, Y., Park, S., Im, J., Yoo, C., and Quackenbush, L. J.: Estimating ground-level particulate matter concentrations using satellite-based data: a review, GIScience & Remote Sensing, 57, 174–189, 2020.

Silvern, R. F., Jacob, D. J., Mickley, L. J., Sulprizio, M. P., Travis, K. R., Marais, E. A., Cohen, R. C., Laughner, J. L., Choi, S., Joiner, J., and Lamsal, L. N.: Using satellite observations of tropospheric NO_2 columns to infer long-term trends in US NO_x emissions: the importance of accounting for the free tropospheric NO_2 background, Atmos. Chem. Phys., 19, 8863–8878, https://doi.org/10.5194/acp-19-8863-2019, 2019.

SIMES, R. J.: An improved Bonferroni procedure for multiple tests of significance, Biometrika, 73, 751–754, https://doi.org/10.1093/biomet/73.3.751, 1986.

Smirnova, T. G., Brown, J. M., Benjamin, S. G., and Kim, D.: Parameterization of cold-season processes in the MAPS land-surface scheme, Journal of Geophysical Research: Atmospheres, 105, 4077-4086, https://doi.org/10.1029/1999JD901047, 2000.

Snider, G., Weagle, C. L., Martin, R. V., van Donkelaar, A., Conrad, K., Cunningham, D., Gordon, C., Zwicker, M., Akoshile, C., Artaxo, P., Anh, N. X., Brook, J., Dong, J., Garland, R. M., Greenwald, R., Griffith, D., He, K., Holben, B. N., Kahn, R., Koren, I., Lagrosas, N., Lestari, P., Ma, Z., Vanderlei Martins, J., Quel, E. J., Rudich, Y., Salam, A., Tripathi, S. N., Yu, C., Zhang, Q., Zhang, Y., Brauer, M., Cohen, A., Gibson, M. D., and Liu, Y.: SPARTAN: a global network to evaluate and enhance satellite-based estimates of ground-level particulate matter for global health applications, Atmos. Meas. Tech., 8, 505–521, https://doi.org/10.5194/amt-8-505-2015, 2015.

Solomon, P. A., Crumpler, D., Flanagan, J. B., Jayanty, R., Rickman, E. E., and McDade, C. E.: US National PM2. 5 chemical speciation monitoring networks – CSN and IMPROVE: description of networks, Journal of the Air & Waste Management Association, 64, 1410–1438, 2014.

Stockwell, W. R., Middleton, P., Chang, J. S., and Tang, X.: The second generation regional acid deposition model chemical mechanism for regional air quality modeling, Journal of Geophysical Research: Atmospheres, 95, 16343–16367, 1990.

Su, L. and Fung, J. C. H.: Sensitivities of WRF-Chem to dust emission schemes and land surface properties in simulating dust cycles during springtime over East Asia, Journal of Geophysical Research: Atmospheres, 120, 11215–11230, https://doi.org/10.1002/2015JD023446, 2015.

Tao, M., Fiore, A. M., Karambelas, A., Miller, P. J., Valin, L. C., Judd, L. M., Tzortziou, M., Whitehill, A., Teora, A., Tian, Y., Civerolo, K. L., Tong, D., Ma, S., Adamo, S. B., and Holloway, T.: Insights Into Summertime Surface Ozone Formation From Diurnal Variations in Formaldehyde and Nitrogen Dioxide Along a Transect Through New York City, Journal of Geophysical Research: Atmospheres, 130, e2024JD040922, https://doi.org/10.1029/2024JD040922, 2025.

Taylor, K. E.: Summarizing multiple aspects of model performance in a single diagram, Journal of Geophysical Research: Atmospheres, 106, 7183–7192, 2001.

Thomas, A., Huff, A. K., Hu, X.-M., and Zhang, F.: Quantifying Uncertainties of Ground-Level Ozone Within WRF-Chem Simulations in the Mid-Atlantic Region of the United States as a Response to Variability, Journal of Advances in Modeling Earth Systems, 11, 1100–1116, https://doi.org/10.1029/2018MS001457, 2019.

Tie, X., Madronich, S., Walters, S., Zhang, R., Rasch, P., and Collins, W.: Effect of clouds on photolysis and oxidants in the troposphere. Journal of Geophysical Research: Atmospheres, 108, https://doi.org/10.1029/2003JD003659, 2003.

Tsarpalis, K., Papadopoulos, A., Mihalopoulos, N., Spyrou, C., Michaelides, S., and Katsafados, P.: The implementation of a mineral dust wet deposition scheme in the GOCART-AFWA module of the WRF model, Remote Sensing, 10, 1595, https://doi.org/10.3390/rs10101595, 2018.

Tuccella, P., Curci, G., Visconti, G., Bessagnet, B., Menut, L., and Park, R. J.: Modeling of gas and aerosol with WRF/Chem over Europe: Evaluation and sensitivity study, Journal of Geophysical Research: Atmospheres, 117, https://doi.org/10.1029/2011JD016302, 2012.

Ukhov, A., Mostamandi, S., Krotkov, N., Flemming, J., da Silva, A., Li, C., Fioletov, V., McLinden, C., Anisimov, A., and Alshehri, Y. M.: Study of SO_2 Pollution in the Middle East Using MERRA-2, CAMS Data Assimilation Products, and High-Resolution WRF-Chem Simulations, Journal of Geophysical Research: Atmospheres, 125, e2019JD031993, https://doi.org/10.1029/2019JD031993, 2020.

Ukhov, A., Ahmadov, R., Grell, G., and Stenchikov, G.: Improving dust simulations in WRF-Chem v4.1.3 coupled with the GOCART aerosol module, Geosci. Model Dev., 14, 473–493, https://doi.org/10.5194/gmd-14-473-2021, 2021.

van der Werf, G. R., Randerson, J. T., Giglio, L., Collatz, G. J., Mu, M., Kasibhatla, P. S., Morton, D. C., DeFries, R. S., Jin, Y., and van Leeuwen, T. T.: Global fire emissions and the contribution of deforestation, savanna, forest, agricultural, and

peat fires (1997–2009), Atmos. Chem. Phys., 10, 11707–11735, https://doi.org/10.5194/acp-10-11707-2010, 2010.

Van Donkelaar, A., Martin, R. V., and Park, R. J.: Estimating ground-level $PM_{2.5}$ using aerosol optical depth determined from satellite remote sensing, Journal of Geophysical Research: Atmospheres, 111, https://doi.org/10.1029/2005JD006996, 2006.

Van Donkelaar, A., Martin, R. V., Brauer, M., Kahn, R., Levy, R., Verduzco, C., and Villeneuve, P. J.: Global estimates of ambient fine particulate matter concentrations from satellite-based aerosol optical depth: development and application, Environmental Health Perspectives, 118, 847, https://doi.org/10.1289/ehp.0901623, 2010.

Viana, M., Pey, J., Querol, X., Alastuey, A., de Leeuw, F., and Lükewille, A.: Natural sources of atmospheric aerosols influencing air quality across Europe, Science of The Total Environment, 472, 825–833, https://doi.org/10.1016/j.scitotenv.2013.11.140, 2014.

Vinken, G. C. M., Boersma, K. F., Maasakkers, J. D., Adon, M., and Martin, R. V.: Worldwide biogenic soil NO_x emissions inferred from OMI NO_2 observations, Atmos. Chem. Phys., 14, 10363–10381, https://doi.org/10.5194/acp-14-10363-2014, 2014.

Wagner, A., Heinzeller, D., Wagner, S., Rummler, T., and Kunstmann, H.: Explicit convection and scale-aware cumulus parameterizations: High-resolution simulations over areas of different topography in Germany, Monthly Weather Review, 146, 1925–1944, 2018.

Wang, J. and Christopher, S. A.: Intercomparison between satellite-derived aerosol optical thickness and $PM_{2.5}$ mass: Implications for air quality studies, Geophysical Research Letters, 30, https://doi.org/10.1029/2003GL018174, 2003.

Wang, J., Nair, U., and Christopher, S. A.: GOES 8 aerosol optical thickness assimilation in a mesoscale model: Online integration of aerosol radiative effects, Journal of Geophysical Research: Atmospheres, 109, https://doi.org/10.1029/2004JD004827, 2004.

Wang, J., Ge, C., Yang, Z., Hyer, E. J., Reid, J. S., Chew, B.-N., Mahmud, M., Zhang, Y., and Zhang, M.: Mesoscale modeling of smoke transport over the Southeast Asian Maritime Continent: Interplay of sea breeze, trade wind, typhoon, and topography, Atmospheric Research, 122, 486–503, 2013.

Wang, J., Huang, B., Fu, D., Atkinson, P. M., and Zhang, X.: Response of urban heat island to future urban expansion over the Beijing–Tianjin–Hebei metropolitan area, Applied Geography, 70, 26–36, 2016.

Wang, L., Wu, X., Du, J., Cao, W., and Sun, S.: Global burden of ischemic heart disease attributable to ambient $PM_{2.5}$ pollution from 1990 to 2017, Chemosphere, 263, 128134, https://doi.org/10.1016/j.chemosphere.2020.128134, 2021a.

Wang, Q., Gu, J., and Wang, X.: The impact of Sahara dust on air quality and public health in European countries, Atmospheric Environment, 241, 117771, https://doi.org/10.1016/j.atmosenv.2020.117771, 2020a.

Wang, R., Qiao, F., Liang, X.-Z., Zhu, Y., Zhang, H., Li, Q., and Ding, Y.: Role of convection representation across the gray zone in forecasting warm season extreme precipitation over Shanghai from two typical cases, Atmospheric Research, 253, 105370, https://doi.org/10.1016/j.atmosres.2020.105370, 2021b.

Wang, Y., Ge, C., Garcia, L. C., Jenerette, G. D., Oikawa, P. Y., and Wang, J.: Improved modelling of soil NO × emissions in a high temperature agricultural region: role of background emissions on NO_2 trend over the US, Environmental Research Letters, 16, 084061, https://doi.org/10.1088/1748-9326/ac16a3, 2021c.

Wang, Y., Wang, J., Xu, X., Henze, D. K., Qu, Z., and Yang, K.: Inverse modeling of SO_2 and NO_x emissions over China using multisensor satellite data – Part 1: Formulation and sensitivity analysis, Atmos. Chem. Phys., 20, 6631–6650, https://doi.org/10.5194/acp-20-6631-2020, 2020b.

Wang, Y., Wang, J., Zhou, M., Henze, D. K., Ge, C., and Wang, W.: Inverse modeling of SO_2 and NO_x emissions over China using multisensor satellite data – Part 2: Downscaling techniques for air quality analysis and forecasts, Atmos. Chem. Phys., 20, 6651–6670, https://doi.org/10.5194/acp-20-6651-2020, 2020c.

Wang, Y., Wang, J., Zhang, H., Janechek, N., Wang, Y., Zhou, M., Shen, P., Tan, J., He, Q., Cheng, T., and Huang, C.: Impact of land use change on the urban-rural temperature disparity in Eastern China, Atmospheric Environment, 308, 119850, https://doi.org/10.1016/j.atmosenv.2023.119850, 2023.

Wei, J., Wang, J., Li, Z., Kondragunta, S., Anenberg, S., Wang, Y., Zhang, H., Diner, D., Hand, J., and Lyapustin, A.: Long-term mortality burden trends attributed to black carbon and $PM_{2.5}$ from wildfire emissions across the continental USA from 2000 to 2020: a deep learning modelling study, The Lancet Planetary Health, 7, e963–e975, 2023.

Weichenthal, S., Christidis, T., Olaniyan, T., van Donkelaar, A., Martin, R., Tjepkema, M., Burnett, R. T., and Brauer, M.: Epidemiological studies likely need to consider $PM_{2.5}$ composition even if total outdoor $PM_{2.5}$ mass concentration is the exposure of interest, Environmental Epidemiology, 8, e317, https://doi.org/10.1097/EE9.0000000000000317, 2024.

Weisman, M. L., Skamarock, W. C., and Klemp, J. B.: The resolution dependence of explicitly modeled convective systems, Monthly Weather Review, 125, 527–548, 1997.

Weisman, M. L., Davis, C., Wang, W., Manning, K. W., and Klemp, J. B.: Experiences with 0–36-h explicit convective forecasts with the WRF-ARW model, Weather and Forecasting, 23, 407–437, 2008.

Wiedinmyer, C., Akagi, S. K., Yokelson, R. J., Emmons, L. K., Al-Saadi, J. A., Orlando, J. J., and Soja, A. J.: The Fire INventory from NCAR (FINN): a high resolution global model to estimate the emissions from open burning, Geosci. Model Dev., 4, 625–641, https://doi.org/10.5194/gmd-4-625-2011, 2011.

Wilks, D. S.: Chapter 9 – Time Series, in: International Geophysics, edited by: Wilks, D. S., Vol. 100, Academic Press, 395–456, https://doi.org/10.1016/B978-0-12-385022-5.00009-9, 2011.

WRF-model: WRF, GitHub [code], https://github.com/wrf-model/WRF/tree/v4.0, last access: 10 May 2022.

Wu, J., Bei, N., Wang, Y., Li, X., Liu, S., Liu, L., Wang, R., Yu, J., Le, T., Zuo, M., Shen, Z., Cao, J., Tie, X., and Li, G.: Insights into particulate matter pollution in the North China Plain during wintertime: local contribution or regional transport?, Atmos. Chem. Phys., 21, 2229–2249, https://doi.org/10.5194/acp-21-2229-2021, 2021.

Xia, Y., Sheffield, J., Ek, M. B., Dong, J., Chaney, N., Wei, H., Meng, J., and Wood, E. F.: Evaluation of multi-model simulated soil moisture in NLDAS-2, Journal of Hydrology, 512, 107–125, https://doi.org/10.1016/j.jhydrol.2014.02.027, 2014.

Yang, Z., Wang, J., Ichoku, C., Hyer, E., and Zeng, J.: Mesoscale modeling and satellite observation of transport and mixing of smoke and dust particles over northern sub-Saharan African

region, Journal of Geophysical Research: Atmospheres, 118, 12139–12157, 2013.

Yu, E., Bai, R., Chen, X., and Shao, L.: Impact of physical parameterizations on wind simulation with WRF V3.9.1.1 under stable conditions at planetary boundary layer gray-zone resolution: a case study over the coastal regions of North China, Geosci. Model Dev., 15, 8111–8134, https://doi.org/10.5194/gmd-15-8111-2022, 2022.

Zeng, Y., Wang, M., Zhao, C., Chen, S., Liu, Z., Huang, X., and Gao, Y.: WRF-Chem v3.9 simulations of the East Asian dust storm in May 2017: modeling sensitivities to dust emission and dry deposition schemes, Geosci. Model Dev., 13, 2125–2147, https://doi.org/10.5194/gmd-13-2125-2020, 2020.

Zhang, F., Wang, J., Ichoku, C., Hyer, E. J., Yang, Z., Ge, C., Su, S., Zhang, X., Kondragunta, S., and Kaiser, J. W.: Sensitivity of mesoscale modeling of smoke direct radiative effect to the emission inventory: a case study in northern sub-Saharan African region, Environmental Research Letters, 9, 075002, https://doi.org/10.1088/1748-9326/9/7/075002, 2014.

Zhang, G. J. and McFarlane, N. A.: Sensitivity of climate simulations to the parameterization of cumulus convection in the Canadian Climate Centre general circulation model, Atmosphere-Ocean, 33, 407–446, 1995.

Zhang, H.: Development of UI-WRF-Chem (v1.0) for the MAIA satellite mission: case demonstration, Zenodo [code], https://doi.org/10.5281/zenodo.15074107, 2025a.

Zhang, H.: Development of UI-WRF-Chem (v1.0) for the MAIA satellite mission: case demonstration, Zenodo [data set], https://doi.org/10.5281/zenodo.15239058, 2025b.

Zhang, H., Wang, S., Hao, J., Wang, X., Wang, S., Chai, F., and Li, M.: Air pollution and control action in Beijing, Journal of Cleaner Production, 112, 1519–1527, 2016.

Zhang, H., Wang, J., García, L. C., Ge, C., Plessel, T., Szykman, J., Murphy, B., and Spero, T. L.: Improving Surface $PM_{2.5}$ Forecasts in the United States Using an Ensemble of Chemical Transport Model Outputs: 1. Bias Correction With Surface Observations in Nonrural Areas, Journal of Geophysical Research: Atmospheres, 125, e2019JD032293, https://doi.org/10.1029/2019jd032293, 2020.

Zhang, H., Wang, J., García, L. C., Zhou, M., Ge, C., Plessel, T., Szykman, J., Levy, R. C., Murphy, B., and Spero, T. L.: Improving Surface $PM_{2.5}$ Forecasts in the United States Using an Ensemble of Chemical Transport Model Outputs: 2. Bias Correction With Satellite Data for Rural Areas, Journal of Geophysical Research: Atmospheres, 127, e2021JD035563, https://doi.org/10.1029/2021JD035563, 2022.

Zhang, X., Kondragunta, S., Ram, J., Schmidt, C., and Huang, H. C.: Near-real-time global biomass burning emissions product from geostationary satellite constellation, Journal of Geophysical Research: Atmospheres, 117, https://doi.org/10.1029/2012JD017459, 2012.

Zhang, X.-X., Sharratt, B., Liu, L.-Y., Wang, Z.-F., Pan, X.-L., Lei, J.-Q., Wu, S.-X., Huang, S.-Y., Guo, Y.-H., Li, J., Tang, X., Yang, T., Tian, Y., Chen, X.-S., Hao, J.-Q., Zheng, H.-T., Yang, Y.-Y., and Lyu, Y.-L.: East Asian dust storm in May 2017: observations, modelling, and its influence on the Asia-Pacific region, Atmos. Chem. Phys., 18, 8353–8371, https://doi.org/10.5194/acp-18-8353-2018, 2018.

Zhang, Y., Roundy, J. K., and Santanello, J. A.: Evaluating the impact of model resolutions and cumulus parameterization on precipitation in NU-WRF: A case study in the Central Great Plains, Environmental Modelling & Software, 145, 105184, https://doi.org/10.1016/j.envsoft.2021.105184, 2021.

Zhao, T., Gong, S., Zhang, X., and McKendry, I.: Modeled size-segregated wet and dry deposition budgets of soil dust aerosol during ACE-Asia 2001: Implications for trans-Pacific transport, Journal of Geophysical Research: Atmospheres, 108, https://doi.org/10.1029/2002JD003363, 2003.

Zheng, B., Tong, D., Li, M., Liu, F., Hong, C., Geng, G., Li, H., Li, X., Peng, L., Qi, J., Yan, L., Zhang, Y., Zhao, H., Zheng, Y., He, K., and Zhang, Q.: Trends in China's anthropogenic emissions since 2010 as the consequence of clean air actions, Atmos. Chem. Phys., 18, 14095–14111, https://doi.org/10.5194/acp-18-14095-2018, 2018.

Zhou, M., Wang, J., Garcia, L. C., Chen, X., da Silva, A. M., Wang, Z., Román, M. O., Hyer, E. J., and Miller, S. D.: Enhancement of Nighttime Fire Detection and Combustion Efficiency Characterization Using Suomi-NPP and NOAA-20 VIIRS Instruments, IEEE Transactions on Geoscience and Remote Sensing, 61, 1–20, 2023.

Zhu, Q., Place, B., Pfannerstill, E. Y., Tong, S., Zhang, H., Wang, J., Nussbaumer, C. M., Wooldridge, P., Schulze, B. C., Arata, C., Bucholtz, A., Seinfeld, J. H., Goldstein, A. H., and Cohen, R. C.: Direct observations of NO_x emissions over the San Joaquin Valley using airborne flux measurements during RECAP-CA 2021 field campaign, Atmos. Chem. Phys., 23, 9669–9683, https://doi.org/10.5194/acp-23-9669-2023, 2023.

Zhu, Q., Liu, Y., and Hasheminassab, S.: Long-term source apportionment of $PM_{2.5}$ across the contiguous United States (2000–2019) using a multilinear engine model, Journal of Hazardous Materials, 472, 134550, https://doi.org/10.1016/j.jhazmat.2024.134550, 2024.

Zhu, Q., Liu, Y., and Xiao, N.: The Frequency and Intensity of Extreme Dust Events and Related Driving Factors in Major Dust Sources Based on MERRA-2 Aerosol Reanalysis, Journal of Climate, https://doi.org/10.1175/JCLI-D-24-0702.1, 2025.

Zoogman, P., Liu, X., Suleiman, R., Pennington, W., Flittner, D., Al-Saadi, J., Hilton, B., Nicks, D., Newchurch, M., and Carr, J.: Tropospheric emissions: Monitoring of pollution (TEMPO), Journal of Quantitative Spectroscopy and Radiative Transfer, 186, 17–39, 2017.